



**T.C.  
İSTANBUL UNIVERSITY-CERRAHPASA  
INSTITUTE OF GRADUATE STUDIES**



**Ph.D. THESIS**

**MAGNETICALLY RECYCLABLE NANOCATALYSTS FOR  
ORGANIC REACTIONS**

**Ümran KURTAN**

**SUPERVISOR**

**Assoc. Prof. Dr. İlven MUTLU**

**Department of Bio and Nanotechnology Engineering**

**Bio and Nanotechnology Engineering Programme**

**ISTANBUL- December, 2018**

This study was accepted on 28/12/2018 as a Ph. D. thesis in Department of Bio and Nanotechnology Engineering, Bio and Nanotechnology Engineering Programme by the following Committee.

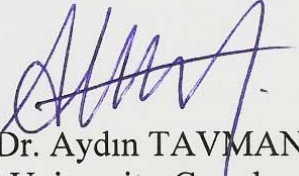
### Examining Committee Members



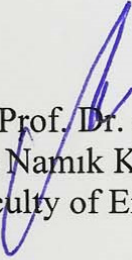
Assoc. Prof. Dr. İlven MUTLU (Supervisor)  
Istanbul University-Cerrahpaşa  
Faculty of Engineering



Prof. Dr. Ayben KİLİSLİOĞLU  
Istanbul University-Cerrahpaşa  
Faculty of Engineering



Prof. Dr. Aydın TAVMAN  
Istanbul University-Cerrahpaşa  
Faculty of Engineering



Assoc. Prof. Dr. Aylin YILDIZ  
Tekirdağ Namık Kemal University  
Faculty of Engineering

Assist. Prof. Dr. Ayşe A. CANPOLAT  
Gebze Technical University  
Faculty of Engineering





As required by the 9/2 and 22/2 articles of the Graduate Education Regulation which was published in the Official Gazette on 20.04.2016, this graduate thesis is reported as in accordance with criteria determined by the Institute of Graduate Studies by using the plagiarism software to which İstanbul University-Cerrahpasa is a subscriber.

This thesis is supported by the project numbered ..... of İstanbul University Scientific Research Projects Executive Secretariat.

This thesis is supported by the project numbered ..... of .....

## FOREWORD

I have completed the course and research stages of this thesis work in PhD program of Department of Biyo-Nano Technology Engineering at Fatih University, where has been closed. I would like to thank Prof. Dr. Abdülhadi BAYKAL, for making this thesis possible through his wealth of academic experience in inorganic synthesis. More than a supervisor, helped me a lot by his support and suggestions and was me anytime during my research period whenever I need.

I would like to thank our coordinator teacher Prof. Dr. Ayben KİLİSLİOĞLU for her contributions during the completion of this thesis at İstanbul University.

I specially thank to my advisor Asst. Prof. Dr. İlven MUTLU for his generous assistance and support during the completion of this thesis.

I express my thanks to Prof. Dr. Muhammed TOPRAK from KTH Royal Institute for his scientific discussions and contributions.

I would like to thank Dr.Utkan ŞAHİNTÜRK for his understanding and motivation.

I am also very grateful to my colleagues Ms. Hamide Aydın, Mr. Md Amir for their friendship and encouragement.

Finally, my special thnaks to my parents for their love, patience and encouragement. Without their support, I could not succeed it.

December 2018

Ümran KURTAN

# TABLE OF CONTENTS

	Page
<b>FOREWORD</b> .....	<b>iv</b>
<b>TABLE OF CONTENTS</b> .....	<b>v</b>
<b>LIST OF FIGURES</b> .....	<b>vii</b>
<b>LIST OF TABLES</b> .....	<b>xiii</b>
<b>LIST OF SYMBOLS AND ABBREVIATIONS</b> .....	<b>xiv</b>
<b>ÖZET</b> .....	<b>xv</b>
<b>SUMMARY</b> .....	<b>xvii</b>
<b>1. INTRODUCTION</b> .....	<b>1</b>
1.1. NANOTECHNOLOGY .....	1
1.2. NANOSTRUCTURED MATERIALS .....	2
1.3. MAGNETIC NANOPARTICLES (MNPs).....	3
1.3.1. Spinel Ferrites .....	4
1.3.1.1. <i>Co-precipitation</i> .....	5
1.3.1.2. <i>Thermal Decomposition</i> .....	5
1.3.1.3. <i>Hydrothermal Reaction</i> .....	6
1.3.1.4. <i>Microemulsion</i> .....	6
1.3.1.5. <i>Sol-Gel Method</i> .....	7
1.4. MAGNETIC PROPERTIES .....	7
1.4.1. Hysteresis Loop .....	8
1.5. SURFACE MODIFICATION .....	9
1.5.1. Silica .....	10
1.5.2. Polymers .....	11
1.6. CATALYSIS.....	11
1.6.1. Homogeneous Catalysis.....	12
1.6.2. Heterogeneous Catalysis.....	13
1.6.3. Catalytic Applications of Magnetic Nanocomposites .....	13
1.7. DYES .....	14
<b>2. MATERIALS AND METHODS</b> .....	<b>15</b>
2.1. CHEMICALS.....	15
2.2. INSTRUMENTATIONS .....	15

2.3. PROCEDURE.....	16
2.3.1. Preparation of Fe <sub>3</sub> O <sub>4</sub> @Tween-Ag Magnetic Hybrid.....	16
2.3.2. Preparation of Fe <sub>3</sub> O <sub>4</sub> @His-Cu and Fe <sub>3</sub> O <sub>4</sub> @His-Ag Magnetic Hybrids.....	16
2.3.3. Preparation of Fe <sub>3</sub> O <sub>4</sub> @Nico-Ag and Fe <sub>3</sub> O <sub>4</sub> @Nico-Cu Magnetic Hybrids .....	17
2.3.4. Preparation of MnFe <sub>2</sub> O <sub>4</sub> @PANI-Ag and MnFe <sub>2</sub> O <sub>4</sub> @SiO <sub>2</sub> -Ag Magnetic Hybrids.....	19
2.3.5. Preparation of Fe <sub>3</sub> O <sub>4</sub> @PAMAM(G1)-Ag Magnetic Hybrid.....	20
2.4. CATALYTIC STUDIES.....	21
<b>3. RESULTS .....</b>	<b>22</b>
3.1. ANALYSIS OF MAGNETIC NANOCATALYSTS .....	22
3.1.1. Characterization Results of Fe <sub>3</sub> O <sub>4</sub> @Tween20-Ag Magnetic Hybrid.....	22
3.1.2. Characterization Results of Fe <sub>3</sub> O <sub>4</sub> @His-Cu Magnetic Hybrid .....	24
3.1.3. Characterization Results of Fe <sub>3</sub> O <sub>4</sub> @His-Ag Magnetic Hybrid.....	28
3.1.4. Characterization Results of Fe <sub>3</sub> O <sub>4</sub> @Nico-Ag Magnetic Hybrid.....	32
3.1.5. Characterization Results of Fe <sub>3</sub> O <sub>4</sub> @Nico-Cu Magnetic Hybrid.....	35
3.1.6. Characterization Results of MnFe <sub>2</sub> O <sub>4</sub> @PANI-Ag Magnetic Hybrid.....	39
3.1.7. Characterization Results of MnFe <sub>2</sub> O <sub>4</sub> @SiO <sub>2</sub> -Ag Magnetic Hybrid .....	46
3.1.8. Characterization Results of Fe <sub>3</sub> O <sub>4</sub> @PAMAM(G1)-Ag Magnetic Hybrid.....	49
<b>4. DISCUSSION .....</b>	<b>55</b>
4.1. EVALUATION OF UV-VIS RESULTS OF MAGNETIC NANOCATALYSTS.....	55
4.1.1. Catalytic Tests of Fe <sub>3</sub> O <sub>4</sub> @Tween20-Ag Magnetic Nanocatalysts .....	55
4.1.1.1. For azo dyes reduction .....	55
4.1.1.2. For nitro aromatics reduction.....	60
4.1.2. Catalytic Tests of Fe <sub>3</sub> O <sub>4</sub> @His-Cu Magnetic Nanocatalysts.....	63
4.1.3. Catalytic Tests of Fe <sub>3</sub> O <sub>4</sub> @His-Ag Magnetic Nanocatalysts.....	67
4.1.4. Catalytic Tests of Fe <sub>3</sub> O <sub>4</sub> @Nico-Ag Magnetic Nanocatalysts .....	70
4.1.4.1. For Nitro aromatics.....	70
4.1.4.2. For Azo dyes .....	74
4.1.5. Catalytic Tests of Fe <sub>3</sub> O <sub>4</sub> @Nico-Cu Magnetic Nanocatalysts.....	79
4.1.6. Catalytic Tests of MnFe <sub>2</sub> O <sub>4</sub> @PANI-Ag Magnetic Nanocatalysts .....	83
4.1.7. Catalytic Tests of MnFe <sub>2</sub> O <sub>4</sub> @SiO <sub>2</sub> -Ag Magnetic Hybrid .....	88
4.1.7.1. Azo dyes reduction.....	88
4.1.8. Catalytic Tests of Fe <sub>3</sub> O <sub>4</sub> @PAMAM(G1)-Ag Magnetic Hybrid .....	93
<b>5. CONCLUSION AND RECOMMENDATIONS.....</b>	<b>96</b>
<b>REFERENCES .....</b>	<b>98</b>
<b>CURRICULUM VITAE .....</b>	<b>104</b>

## LIST OF FIGURES

	<b>Page</b>
<b>Figure 1.1:</b> Various applications of nanotechnology [3].	1
<b>Figure 1.2:</b> The clasification of nanostructures.	3
<b>Figure 1.3:</b> The general representation of spinel ferrites[8].	4
<b>Figure 1.4:</b> An illustration of NP synthesis by thermal decompostion process [8].	5
<b>Figure 1.5:</b> Autoclave used for hydrothermal method.	6
<b>Figure 1.6:</b> An illustration of sol-gel reaction.	7
<b>Figure 1.7:</b> Different types of magnetic behaviors of materials.	8
<b>Figure 1.8:</b> Example of magnetization curve.	9
<b>Figure 1.9:</b> Representation for the synthesis of silica coated MNPs [23].	11
<b>Figure 1.10:</b> A representation for the catalyzed pathway [27].	12
<b>Figure 1.11:</b> Magnetic filtration of dispersed MNPs (left: the application of the magnet immediately; right: a short time later).	13
<b>Figure 1.12:</b> A representation for the magnetic gel composite preparation[15].	14
<b>Figure 2.1:</b> Synthesis protocol of the Fe <sub>3</sub> O <sub>4</sub> @Tween20-Ag magnetic hybrid.	16
<b>Figure 2.2:</b> Suggested coordination of histidine to Fe <sub>3</sub> O <sub>4</sub> @His magnetic nanoparticle surface.	17
<b>Figure 2.3:</b> Formation process of the Fe <sub>3</sub> O <sub>4</sub> @Nico-Ag magnetic hybrid.	18
<b>Figure 2.4:</b> Formation process of the Fe <sub>3</sub> O <sub>4</sub> @Nico-Cu magnetic hybrid.	18
<b>Figure 2.5:</b> Synthesis route for the MnFe <sub>2</sub> O <sub>4</sub> @PANI-Ag.	19
<b>Figure 2.6:</b> Synthesis of MnFe <sub>2</sub> O <sub>4</sub> @SiO <sub>2</sub> -Ag magnetic hybrid	20
<b>Figure 2.7:</b> Formation process of the Fe <sub>3</sub> O <sub>4</sub> @PAMAM(G1)-Ag magnetic hybrid.	21
<b>Figure 3.1:</b> (a) XRD of Fe <sub>3</sub> O <sub>4</sub> @Tween20-Ag, (b) FTIR (I) Fe <sub>3</sub> O <sub>4</sub> @Tween20-Ag, (II) Tween-20, (III) Oleicacid and (IV) bare Fe <sub>3</sub> O <sub>4</sub> (c) magnetic hysteresis curve, (d) TG-DTA thermograms.	23

<b>Figure 3.2:</b> SEM micrographs of Fe <sub>3</sub> O <sub>4</sub> @Tween20-Ag nanocomposite with EDX result. ....	24
<b>Figure 3.3:</b> (I) XRD powder pattern of Fe <sub>3</sub> O <sub>4</sub> @His@Cu and (II) FTIR spectra of (a) His and (b) Fe <sub>3</sub> O <sub>4</sub> @His-Cu. ....	25
<b>Figure 3.4:</b> TG thermograms of (a) Histidine and (b) Fe <sub>3</sub> O <sub>4</sub> @His-Cu magnetic hybrid. ....	26
<b>Figure 3.5:</b> SEM micrographs and EDX spectra of Fe <sub>3</sub> O <sub>4</sub> @His-@Cu magnetic nanocomposite at various magnifications. ....	27
<b>Figure 3.6:</b> Magnetic hysteresis curve of Fe <sub>3</sub> O <sub>4</sub> @His-Cu magnetic hybrid. ....	28
<b>Figure 3.7:</b> (I) XRD powder pattern of Fe <sub>3</sub> O <sub>4</sub> @His-Ag and (II) TG thermograms of (a) bare Fe <sub>3</sub> O <sub>4</sub> , (b) Fe <sub>3</sub> O <sub>4</sub> @His-Ag and (c) Histidine [82]. ....	29
<b>Figure 3.8:</b> (I) FTIR spectra of (a) Fe <sub>3</sub> O <sub>4</sub> @His-Ag, (b) His and (c) Fe <sub>3</sub> O <sub>4</sub> @His and (II) magnetization plot of Fe <sub>3</sub> O <sub>4</sub> @His-Ag magnetic hybrid [82]. ....	30
<b>Figure 3.9:</b> (a) The SEM images, (b) EDX and (c) TEM image with the particle size distribution diagram of Fe <sub>3</sub> O <sub>4</sub> @His-Ag magnetic hybrid. ....	31
<b>Figure 3.10:</b> XRD powder pattern of Fe <sub>3</sub> O <sub>4</sub> @Nico-Ag magnetic hybrid. ....	32
<b>Figure 3.11:</b> FTIR spectra of (a) Nicotinic acid and (b) Fe <sub>3</sub> O <sub>4</sub> @Nico-Ag magnetic hybrid. ....	33
<b>Figure 3.12:</b> TG plot of (a) Nicotinic acid and (b) Fe <sub>3</sub> O <sub>4</sub> @Nico-Ag magnetic hybrid. ....	34
<b>Figure 3.13:</b> Magnetic hysteresis curve of Fe <sub>3</sub> O <sub>4</sub> @Nico-Ag magnetic hybrid. ....	34
<b>Figure 3.14:</b> SEM image of Fe <sub>3</sub> O <sub>4</sub> @Nico-Ag magnetic hybrid. ....	35
<b>Figure 3.15:</b> XRD powder pattern of Fe <sub>3</sub> O <sub>4</sub> @Nico-Ag magnetic hybrid. ....	36
<b>Figure 3.16:</b> FTIR spectra of (a) Nico, (b) Fe <sub>3</sub> O <sub>4</sub> @Nico and (c) Fe <sub>3</sub> O <sub>4</sub> @Nico-Cu samples. ....	36
<b>Figure 3.17:</b> TG thermogram of (a) Nicotinic acid and (b) Fe <sub>3</sub> O <sub>4</sub> @Nico-Cu magnetic hybrid. ....	37
<b>Figure 3.18:</b> Magnetic hysteresis curve of Fe <sub>3</sub> O <sub>4</sub> @Nico-Cu magnetic hybrid. ....	38
<b>Figure 3.19:</b> SEM micrographs of Fe <sub>3</sub> O <sub>4</sub> @Nico-Cu magnetic hybrid. ....	39
<b>Figure 3.20:</b> XRD pattern of the MnFe <sub>2</sub> O <sub>4</sub> @PANI-Ag magnetic hybrid. ....	40
<b>Figure 3.21:</b> FTIR spectra (a) MnFe <sub>2</sub> O <sub>4</sub> @PANI and (b) MnFe <sub>2</sub> O <sub>4</sub> @PANI-Ag magnetic hybrid. ....	41
<b>Figure 3.22:</b> TG curves of (a) PANI and (b) MnFe <sub>2</sub> O <sub>4</sub> @PANI-Ag samples. ....	42



<b>Figure 3.23:</b> Magnetic hysteresis curve of MnFe <sub>2</sub> O <sub>4</sub> @PANI-Ag magnetic hybrid. ....	43
<b>Figure 3.24:</b> (a) SEM images and (b) EDX spectra of MnFe <sub>2</sub> O <sub>4</sub> @PANI-Ag sample. ....	44
<b>Figure 3.25:</b> TEM images for MnFe <sub>2</sub> O <sub>4</sub> @PANI-Ag magnetic hybrid.....	45
<b>Figure 3.26:</b> XRD powder pattern of MnFe <sub>2</sub> O <sub>4</sub> @SiO <sub>2</sub> -Ag magnetic hybrid.....	46
<b>Figure 3.27:</b> FTIR spectrum of MnFe <sub>2</sub> O <sub>4</sub> @SiO <sub>2</sub> -Ag magnetic hybrid. ....	47
<b>Figure 3.28:</b> TG curves of (a) MnFe <sub>2</sub> O <sub>4</sub> , (b) SiO <sub>2</sub> coated MnFe <sub>2</sub> O <sub>4</sub> and (c) MnFe <sub>2</sub> O <sub>4</sub> @SiO <sub>2</sub> -Ag samples.....	48
<b>Figure 3.29:</b> Magnetic hysteresis plots of (a) MnFe <sub>2</sub> O <sub>4</sub> , (b) SiO <sub>2</sub> coated MnFe <sub>2</sub> O <sub>4</sub> and (c) MnFe <sub>2</sub> O <sub>4</sub> @SiO <sub>2</sub> -Ag magnetic hybrids. ....	49
<b>Figure 3.30:</b> XRD powder pattern of Fe <sub>3</sub> O <sub>4</sub> @PAMAM(G1)-Ag magnetic hybrid. ....	50
<b>Figure 3.31:</b> FTIR spectra of (a) Fe <sub>3</sub> O <sub>4</sub> and (b) Fe <sub>3</sub> O <sub>4</sub> @PAMAM(G1)-Ag samples.....	51
<b>Figure 3.32:</b> TEM images of Fe <sub>3</sub> O <sub>4</sub> @PAMAM(G1)-Ag nanocomposite different magnifications with particle size distribution diagram. ....	52
<b>Figure 3.33:</b> TG plot of the Fe <sub>3</sub> O <sub>4</sub> @PAMAM-Ag magnetic hybrid.....	53
<b>Figure 3.34:</b> Magnetic hysteresis curve of Fe <sub>3</sub> O <sub>4</sub> @PAMAM-Ag magnetic hybrid.....	54
<b>Figure 4.1:</b> Absorbance of (a) MO dye, MO dye solution after immediate addition of NaBH <sub>4</sub> to MO and NaBH <sub>4</sub> solution after for 24 h; (b) MO dye and NaBH <sub>4</sub> mixture in the presence of Fe <sub>3</sub> O <sub>4</sub> @Tween20-Ag nanocatalyst.....	56
<b>Figure 4.2:</b> Absorbance of MB dye solution (a) after immediate addition of NaBH <sub>4</sub> to MB and NaBH <sub>4</sub> solution after reaction for 24 h; (b) with the help of Fe <sub>3</sub> O <sub>4</sub> @Tween20-Ag nanocatalyst.....	56
<b>Figure 4.3:</b> Plots of first order rates for reduction of (a) MO and (b) MB dye. ....	57
<b>Figure 4.4:</b> Absorbance of (a) RhB dye solution after immediate addition of NaBH <sub>4</sub> only and (b) in the presence of Fe <sub>3</sub> O <sub>4</sub> @Tween20-Ag magnetic nanocatalyst. ....	57
<b>Figure 4.5:</b> The relation between ln(A <sub>t</sub> /A <sub>0</sub> ) and reduction time for RhB reduction.....	58
<b>Figure 4.6:</b> Photographs of the azo dyes catalytically reduced by NaBH <sub>4</sub> with the help of Fe <sub>3</sub> O <sub>4</sub> @Tween20-Ag magnetic nanocatalyst.....	59
<b>Figure 4.7:</b> Changes in catalytic performance of Fe <sub>3</sub> O <sub>4</sub> @Tween20-Ag magnetic hybrid for (a) MO, (b) MB and (c) RhB azo dyes with NaBH <sub>4</sub> , respectively.....	60
<b>Figure 4.8:</b> (I) Absorbance of (a) 2-NA, (b) 3-NA, (c) 4-NA and (d) 4-NP solution immediate addition of NaBH <sub>4</sub> only and (II) one of nitro compounds and NaBH <sub>4</sub> mixture in the existence of Fe <sub>3</sub> O <sub>4</sub> @Tween20-Ag nanocatalyst. ....	61

<b>Figure 4.9:</b> (a) The slope of straight line of $\ln(C_t/C_0)$ vs. reaction time for 4-NP degradation (b) Photographs of the 4-NP catalytically reduced by $\text{Fe}_3\text{O}_4@\text{Tween}20\text{-Ag}$ nanocatalyst and its magnetic separation (c) Graph of $\ln(C/C_0)$ vs. time for four cycles and (d) Comparison of rate constants for each cycle.....	63
<b>Figure 4.10:</b> Absorption spectra of MO dye (a) after immediate addition of $\text{NaBH}_4$ only, (b) methyl orange and sodiumborohydride mixture in the existence of $\text{Fe}_3\text{O}_4@ \text{His}@\text{Cu}$ as nanocatalyst, (c) the first order kinetic plot for MO degradation and (d) catalytic activity of $\text{Fe}_3\text{O}_4@ \text{His}@\text{Cu}$ in different cycling number.....	64
<b>Figure 4.11:</b> Absorbance of (a) methyl blue solution by only $\text{NaBH}_4$ and (b) methyl blue $\text{NaBH}_4$ mixture with the help of $\text{Fe}_3\text{O}_4@ \text{His}@\text{Cu}$ as nanocatalyst, (c) first order kinetic plot of MB reduction using $\text{Fe}_3\text{O}_4@ \text{His}@\text{Cu}$ as catalyst and (d) catalytic activity of $\text{Fe}_3\text{O}_4@ \text{His}@\text{Cu}$ in different cycling number. ....	65
<b>Figure 4.12:</b> Absorbance of (a) azo dyes and reducing agent mixture with the help of $\text{Fe}_3\text{O}_4@ \text{His}@\text{Cu}$ as nanocatalyst, (b) first order kinetic plot of MO and (c) MB reduction using $\text{Fe}_3\text{O}_4@ \text{His}@\text{Cu}$ as catalyst.....	66
<b>Figure 4.13:</b> The mechanism of any azo dye on $\text{Fe}_3\text{O}_4@ \text{His}-\text{Cu}$ nanocatalyst surface in the reduction process. ....	67
<b>Figure 4.14:</b> Absorbance of (a) MO solution by only $\text{NaBH}_4$ and (b) MO and $\text{NaBH}_4$ mixture in the existence of $\text{Fe}_3\text{O}_4@ \text{His}-\text{Ag}$ . ....	68
<b>Figure 4.15:</b> Photographs of azo dyes reduction in the presence of and $\text{Fe}_3\text{O}_4@ \text{His}-\text{Ag}$ and $\text{NaBH}_4$ nanocatalyst.....	68
<b>Figure 4.16:</b> Absorbance of (a) MB and (b) MB and $\text{NaBH}_4$ mixture in the existence of $\text{Fe}_3\text{O}_4@ \text{His}-\text{Ag}$ as nanocatalyst. ....	69
<b>Figure 4.17:</b> The kinetic curve of azo dyes reduction using $\text{Fe}_3\text{O}_4@ \text{His}-\text{Ag}$ as nanocatalyst, respectively.....	70
<b>Figure 4.18:</b> Changes in conversion of (a) MO and (b) MB reduction as the cycling continues.....	70
<b>Figure 4.19:</b> The schematic illustration for the reduction of 4-nitrophenol and 4-nitroaniline compounds in the existence of $\text{Fe}_3\text{O}_4@ \text{Nico}-\text{Ag}$ nanocatalyst.....	71
<b>Figure 4.20:</b> Absorbance of (a) 4-NP and (b) 4-NA by only $\text{NaBH}_4$ and(c) 4-NP and (d) 4-NA with the help of $\text{Fe}_3\text{O}_4@ \text{Nico}-\text{Ag}$ magnetic hybrid.....	72
<b>Figure 4.21:</b> Absorbance for the reduction process of mixture of 4-NP and 4-NA compounds.....	73
<b>Figure 4.22:</b> The relation between $\ln(A_t/A_0)$ and reduction time using $\text{Fe}_3\text{O}_4@ \text{Nico}@\text{Ag}$ as nanocatalyst and (b) Changes in conversion of 4-NP and 4-NA as the cycling continues. ....	73

<b>Figure 4.23:</b> Absorbance of various azo dyes in the presence of NaBH <sub>4</sub> only. ....	74
<b>Figure 4.24:</b> (a) Absorbance of various azo dyes with the help of Fe <sub>3</sub> O <sub>4</sub> @Nico-Ag.....	75
<b>Figure 4.25:</b> (a) Plots of first order rate for reduction of various azo dyes and (b) Changes in catalytic activity of Fe <sub>3</sub> O <sub>4</sub> @Nico-Ag in different cycling number. ....	76
<b>Figure 4.26:</b> (a) Absorbance for the degradation of azo dye mixtures with the help of Fe <sub>3</sub> O <sub>4</sub> @Nico-Ag and (b) Plots of first order rate of azo dyes. ....	77
<b>Figure 4.27:</b> Absorbance of azo dye mixtures with the help of Fe <sub>3</sub> O <sub>4</sub> @Nico@Ag nanocatalyst. ....	78
<b>Figure 4.28:</b> Azo dyes' leuco forms during reduction reactions (hydrazine derivative for MO).....	78
<b>Figure 4.29:</b> (a) Absorption spectra for the MO in the existence of only NaBH <sub>4</sub> , (b) upon addition of magnetic nanocatalyst and (c) The slope of straight line of In (A <sub>t</sub> /A <sub>0</sub> ) vs. reaction time for MO dye reduction. ....	79
<b>Figure 4.30:</b> (a) Absorbance for MB dye in the existence only NaBH <sub>4</sub> , (b) upon addition of prepared magnetic nanocatalyst and (c) The slope of straight line of In (A <sub>t</sub> /A <sub>0</sub> ) vs. time for MB dye degradation. ....	80
<b>Figure 4.31:</b> Absorption spectra for the degradation of eosin Y dye (a) in the existence of only sodiumborohydride, (b) upon addition of prepared magnetic nanocatalyst and (c) The slope of straight line of In (A <sub>t</sub> /A <sub>0</sub> ) vs. reaction time for EY dye reduction. ....	81
<b>Figure 4.32:</b> Absorption spectra of RhB for only (a) sodium borohydride, (b) upon addition of prepared magnetic nanocatalyst and (c) The slope of straight line of In (A <sub>t</sub> /A <sub>0</sub> ) vs. time for RhB dye reduction.....	82
<b>Figure 4.33:</b> Photo that illustrates color change of azo dyes after catalysis reaction and easy separation of it by a magnet. ....	83
<b>Figure 4.34:</b> Absorbance of (a) MO dye by only NaBH <sub>4</sub> and (b) upon addition of MnFe <sub>2</sub> O <sub>4</sub> @PANI-Ag nanocatalyst in the presence of NaBH <sub>4</sub> .....	84
<b>Figure 4.35:</b> Absorbance of MB (a) in the presence of only NaBH <sub>4</sub> and (b) after immediate addition of MnFe <sub>2</sub> O <sub>4</sub> @PANI-Ag nanocatalyst in the existence of NaBH <sub>4</sub> .....	85
<b>Figure 4.36:</b> Absorbance of (a) EY in the presence of only NaBH <sub>4</sub> and (b) upon addition of MnFe <sub>2</sub> O <sub>4</sub> @PANI-Ag, (c) RhB by only NaBH <sub>4</sub> and (d) after immediate addition of MnFe <sub>2</sub> O <sub>4</sub> @PANI-Ag nanocatalyst. ....	86
<b>Figure 4.37:</b> The slope of straight line of In (A <sub>t</sub> /A <sub>0</sub> ) vs. reaction time for various azo dyes reduction.....	87

<b>Figure 4.38:</b> The catalytic performance of the MnFe <sub>2</sub> O <sub>4</sub> @PANI-Ag nanocatalyst in different cycling numbers.....	87
<b>Figure 4.39:</b> Absorption spectra for the reduction process of (a) MO, (b) RhB (c) EY and (d) MB solution after immediate addition of MnFe <sub>2</sub> O <sub>4</sub> @SiO <sub>2</sub> -Ag nanocatalyst in the presence of NaBH <sub>4</sub> . .....	88
<b>Figure 4.40:</b> Absorbance of (a) 4-NP, (b) 4-NA and (c) 2-NA solution after immediate addition of MnFe <sub>2</sub> O <sub>4</sub> @SiO <sub>2</sub> -Ag nanocatalyst in the presence of NaBH <sub>4</sub> . .....	91
<b>Figure 4.41:</b> The first order kinetic plot of various aromatic compounds reduction using magnetic MnFe <sub>2</sub> O <sub>4</sub> @SiO <sub>2</sub> -Ag as nanocatalyst.....	92
<b>Figure 4.42:</b> Recycling of MnFe <sub>2</sub> O <sub>4</sub> @SiO <sub>2</sub> -Ag nanocatalyst for the reduction of (a) MO and (b) MB dye in the presence of NaBH <sub>4</sub> . .....	93
<b>Figure 4.43:</b> UV-Vis absorption spectra of the 4-NP mixture in NaBH <sub>4</sub> solution only.....	94
<b>Figure 4.44:</b> UV-Vis absorption spectra for the reduction of 4-NP in the presence of Fe <sub>3</sub> O <sub>4</sub> @PAMAM(G1)-Ag magnetic nanocatalyst. ....	94
<b>Figure 4.45:</b> (a) First order kinetic plot and (b) the color changes of 4-NP and the recyclability of the catalyst after complete reaction.....	95

## LIST OF TABLES

	<b>Page</b>
<b>Table 4.1:</b> The reaction rates and time of various nitro compounds by $\text{Fe}_3\text{O}_4@\text{Tween}20\text{-Ag}$ .....	62
<b>Table 4.2:</b> The required time and k for the reduction reactions of MO, MB, RhB and EY.....	76
<b>Table 4.3:</b> Reduction time and rates of various compounds by $\text{MnFe}_2\text{O}_4@\text{SiO}_2\text{-Ag}$ catalyzed reactions.....	89

## LIST OF SYMBOLS AND ABBREVIATIONS

<b>Symbol</b>	<b>Explanation</b>
<b>h</b>	:hour
<b>°</b>	:degree
<b>min</b>	:minute
<b>Hkl</b>	:x.y.z coordinates
<b><math>\beta</math></b>	:Full width at half maximum (FWHM)
<b>M<sub>s</sub></b>	:Saturation Magnetization
<b>B<sub>0</sub></b>	:Applied Magnetic Field
<b>M<sub>r</sub></b>	:Remenance
<b>H<sub>c</sub></b>	:Coercivity

<b>Abbreviation</b>	<b>Explanation</b>
<b>ATR:</b>	Attenuated Total Reflectance
<b>FTIR:</b>	Fourier-transform Infrared Spectroscopy
<b>XRD:</b>	X-Ray Diffraction
<b>TGA:</b>	Thermal Gravimetric Analysis
<b>VSM:</b>	Vibrating Simple Magnetometer
<b>MNPs:</b>	Magnetic Nanoparticles
<b>TEOS:</b>	Tetraethyl Orthosilicate
<b>MO:</b>	Methyl Orange
<b>MB:</b>	Methyl Blue
<b>EY:</b>	Eosin Y
<b>RhB:</b>	Rhodamine B
<b>4-NP:</b>	4-nitrophenol
<b>4-NA:</b>	4-nitroaniline
<b>2-NA:</b>	2-nitroaniline
<b>NA:</b>	Nicotinic acid
<b>His:</b>	Histidine
<b>APTES:</b>	(3-aminopropyl)- triethoxysilane

## ÖZET

# ORGANİK REAKSİYONLAR İÇİN MANYETİK OLARAK GERİ DÖNÜŞÜMLÜ NANOKATALİZÖRLER

## DOKTORA TEZİ

Ümran KURTAN

İstanbul Üniversitesi-Cerrahpaşa

Lisansüstü Eğitim Enstitüsü

Biyo ve Nano Teknoloji Mühendisliği Anabilim Dalı

Danışman : Doç. Dr. İlven MUTLU

Her zaman birçok farklı uygulama için araştırmacıların yeni ve daha verimli nanomalzemeler bulma eğilimi olmuştur. Sulu ortamdan boya uzaklaştırmak için bir dizi malzeme kullanılmasına rağmen, manyetik nano-kompozitler boya sökme işlemi için geniş çapta araştırılmaktadır. Bu tezin içeriği, özellikle organik reaksiyonlar için heterojen manyetik hibrid malzemelerin, özellikle nitro aromatik bileşikler ve azo boyaların indirgenme reaksiyonları için araştırılmıştır. Bu kapsamda kaplanmış manyetik spinel nanopartikülleri (NP'ler)  $AFe_2O_4$  ( $A = Fe, Mn$ ) hidrotermal, termal ayrışma, sol-jel ve birlikte çöktürme gibi çeşitli tekniklerle üretilmiştir.  $Fe_3O_4$  ve  $MnFe_2O_4$  manyetik nanoparçacıklarının agglomerasyonunu önlemek ve stabilitesini arttırmak için yüzeyleri modifiye edilmiştir. Bu amaçla polianilin ya da silica gibi organik ve inorganik yapılar tercih edilmiştir. Daha sonra Ag veya Cu nanopartikülleri manyetik nanokompozitlerin içerisine hapsedilerek malzemelere katalitik aktivite kazandırılmıştır. Böylelikle birçok malzemenin özellikleri biraraya getirilerek çok fonksiyonlu hem manyetik hem katalitikçe aktif nanomalzemeler elde edilmiştir. Elde edilen tüm manyetik hibrit malzemelerin yapısal, morfolojik, spektroskopik ve manyetik karakterizasyonu XRD, SEM, TEM, FTIR ve TGA teknikleri kullanılarak gerçekleştirilmiştir. Optik özellikler için UV-Vis spektrofotometre kullanılmış olup ve sentezlenen tüm örneklerin katalitik aktivitesi ayrıntılı olarak araştırılmıştır.

Aralık 2018, 124 sayfa.

**Anahtar kelimeler:**Nanomalzemeler, Manyetik nanokompozitler, Manyetizma, Kataliz, Kimyasal İndirgenme





## **SUMMARY**

### **MAGNETICALLY RECYCLABLE NANOCATALYSTS FOR ORGANIC REACTIONS**

#### **Ph.D. THESIS**

**Ümran KURTAN**

**Istanbul University-Cerrahpasa**

**Institute of Graduate Studies**

**Department of Bio and Nanotechnology Engineering**

**Supervisor : Assoc. Prof. Dr. İlven MUTLU**

There is always a tendency of the researchers to find new and more efficient nanomaterials for many kinds of applications. Even though a number of materials are used for dye removal from aqueous environment, magnetic nanocomposites are widely investigated for the dye removal process. The content of this thesis is specifically devoted to a description of the heterogeneous magnetic hybrids for organic reactions, particularly nitro aromatics and azo dyes reduction reactions. In this thesis,  $AFe_2O_4$  ( $A= Fe, Mn$ ) type of coated magnetic spinel nanoparticles (NPs) were fabricated by various techniques including hydrothermal, thermal decomposition, sol-gel and co-precipitation.  $Fe_3O_4$  and  $MnFe_2O_4$  magnetic nanoparticles have been modified in order to prevent agglomeration and improve their stability. For this purpose, organic and inorganic structures such as polyaniline or silica have been utilized. Subsequently, Ag or Cu nanoparticles were entrapped into magnetic nanocomposites and catalytic activity was introduced into the materials. In this way, the properties of many materials are combined to obtain multi-functional such as both magnetic and catalytically active nanomaterials. Structural, morphological, spectroscopic and magnetic characterizations of all materials were carried out using XRD, SEM, TEM, FTIR and TGA techniques. The optical properties were obtained by UV-Vis spectrophotometer and the catalytic activity of the all prepared samples has been investigated in detail.

December 2018,124pages.

**Keywords:**Nanomaterials, magnetic nanocomposites, magnetization,catalysis,chemical reduction



## 1. INTRODUCTION

### 1.1. NANOTECHNOLOGY

The invention of “Nanotechnology” has created by Taniguchi in the 1970s and identified as the study of building machines in size (1–100 nm) showing enhanced chemical, physical and also thermal and biological characteristics [1, 2]. Miniaturization of the world has happened with the presentation called “There’s Plenty of Room at the Bottom” by Richard Feynmann’s 1959 talk and the origin of “nanotechnology” was born with this. A miniaturization that would require the ability to manipulate and control materials on a scale smaller than was ever imagined at that time.



**Figure 1.1:** Various applications of nanotechnology [3].

The status of nanoscience has developed over the last 15-20 years and gained significance in the fields of environmental remediation, biomedical application, energy storing devices, computer industry, data storage, computing, magnetic resonance imaging and a wide range of applications of nanotechnology are seen in Fig. 1.1[4]. Nanotechnology is interested in nanomaterials and devices with processes that happen in the “nm” scale. It is a science of chemical research and engineering that develops the design of materials and processes since new kinds of forces, possibilities and effects are faced at the atomic and molecular level.

Assembly of nano components is a key point for the material synthesis thus a great part of accurate multidisciplinary knowledge is to be desired for the development of technologies. Nanomaterials can be considered as *nanostructured materials* which contain at least one of its dimensions in 1-100 nm whereas *nanodispersions* have a homogeneous dispersion medium.

## 1.2. NANOSTRUCTURED MATERIALS

Firstly, it is important to mention the general terms of the nanomaterials. The term “Nano”, meaning dwarf in Greek, is specifying for so small features and representing  $10^{-9}$  meter in length. Generally, the terms of nanostructures and nanostructured materials are complementary. Nanostructures are defined as entities described by form and at least one dimensionality in nanoscale range while nanostructured materials are not only composed of building units which have nanoscale dimensions but they are characterized additionally by composition.

In modern science and technology, nanochemistry is growing exponentially to fabricate of various NPs. Nanomaterials are promising materials because of unique features not observed for their counterparts. Owing to physical dimension limits, such nanostructures show remarkable chemical and mechanical characteristics. Both theory and experimental investigations have been figured out to explore the nanoscale applications based on their dimensions. The examples of the elementary building units of nanostructures are seen in Fig 1.2. Nanorods, nanowires, nanotubes are one dimensional (1D) whereas nanodisks and magnetic nanoparticle layers, etc., are the class of two-dimensional objects (2D).

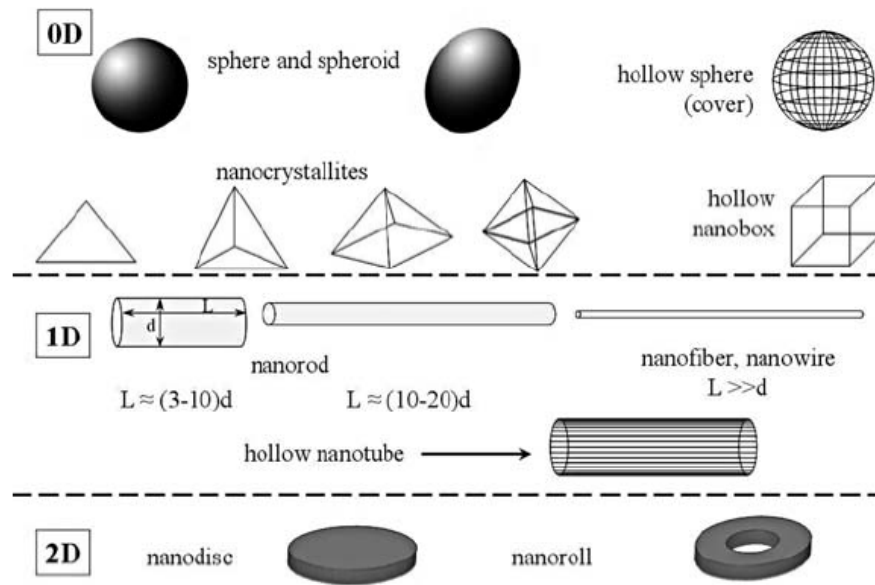


**Figure 1.2:** The clasification of nanostructures.

In the nanostructured materials field, many names and labels have been used. It is significant that some terms are explained in the nanoscale materials. For example; *clusters* are finite aggregates of atoms and molecules that are surrounded by a ligand layer that permits the isolation of molecular species. *Colloids* are mixtures which contain particles dispersed in a liquid medium. *Nanoparticle* is a particle between the 1-100 nm which can be nanocrystalline or an aggregate of crystallites.

### 1.3. MAGNETIC NANOPARTICLES (MNPs)

Unusual physical features of NPs have extensively studied in recent years. Particularly, the magnetic properties owing to the difference between the bulk material and a nanomaterial are under intensive research since their new physicochemical characteristics owing to the higher surface area. The physical characteristics of nanoparticles are known to be importantly dependent on their sizes and the magnetization and the magnetic anisotropy of NPs could be higher than those of a bulk material. These new properties of NPs allows them the possibility to be utilized in a variety of fields and there are different kind of application areas such as technological (data storage, magnetic resonance imaging), environmental (catalysts, hydrogen storage), energy (supercapacitors) and biomedical applications. Therefore, among many of known nanomaterials, magnetic nanoparticles and their structures are of great scientific

interest and investigated by the researchers greatly in recent years. There is a direct connection between the physical properties and the particles size of the samples therefore different processes have now been studied for the production of them containing co-precipitation, thermodecomposition of the metal precursors, hydro/solvothermal reactions, microbial synthesis [5], sol-gel, photolysis [6], electrochemical [7], and other techniques.

### 1.3.1. Spinel Ferrites

Transition metal oxide compounds also called ferrites have the general formula  $MFe_2O_4$  and spinel ferrites are an essential class among several metal oxides. These materials are extremely important materials in science and technology since they have been used in various applications containing data storage, optical devices, gas sensors, drug delivery and catalysis thus they have been extensively investigated by the researchers. due to the high magnetization values which are important for catalytic applications. However, they are not stable and can oxidize easily during the synthesis if they are not reacted specially.

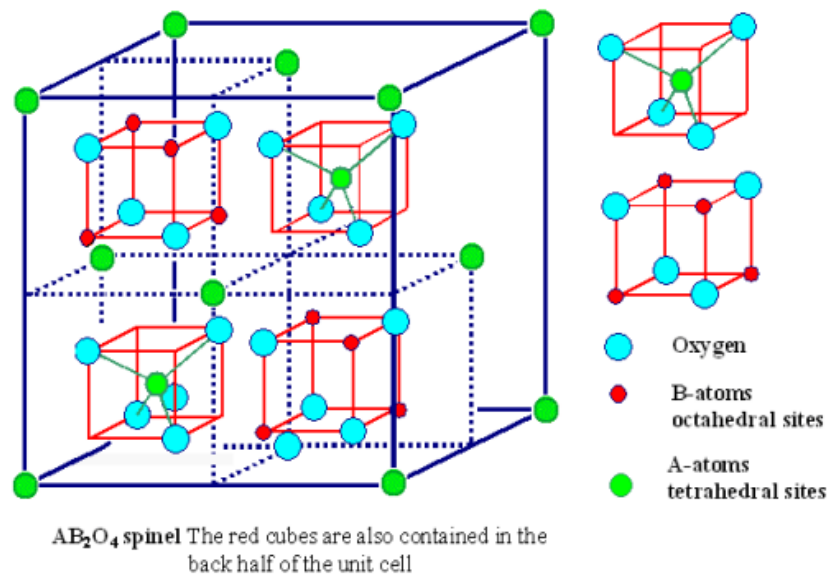


**Figure 1.3:** The general representation of spinel ferrites[8].

In normal spinels, all the  $B^{3+}$  ions present in  $O_h$  while  $A^{2+}$  ions present in the  $T_d$ (Fig. 1.3). When it comes to inverse spinel ferrites, half of the  $T_d$  sites are covered with the  $B^{3+}$ . The other of the  $T_d$  sites is formed of the  $A^{2+}$  ions and the  $O_h$  sites are covered with  $A^{3+}$ (Fig. 1.3).

It should be also noted that various synthesis methods like co-precipitation, hydrothermal, and thermodecomposition have utilized to control size, shape and composition of these materials.

### 1.3.1.1. *Co-precipitation*

It is thought to be the most classical route to produce spinel ferrites and done with the solution of metal salts in an aqueous and basic medium at ambient temperatures. Some surfactants could be required to stabilize the colloidal solution. Importantly, the nature of the metal precursors or pH would influence not only the crystallinity but also the size and the shape of the nanocrystallines. The use of easily found starting materials and the aqueous medium are the advantages of this method. Chelating agents could be used to stabilize the colloidal dispersions but this will cause to precipitate larger particles formation.

### 1.3.1.2. *Thermal Decomposition*

It is the commonly utilized method to prepare highly monodisperse MNPs with smaller size. If the particle size is desired with the accurate control, thermal decomposition methods are generally preferred. Monodisperse MNPs could be synthesized readily by utilizing metal acetylacetonates or metal carbonyls in high boiling solvents at high temperatures (Fig 1.4). Oleic acid and oleylamine can also be used as stabilizing agent. However, it has some disadvantages such as that the precursors are generally highly toxic and prepared nanoparticles are only soluble in nonpolar solvents.

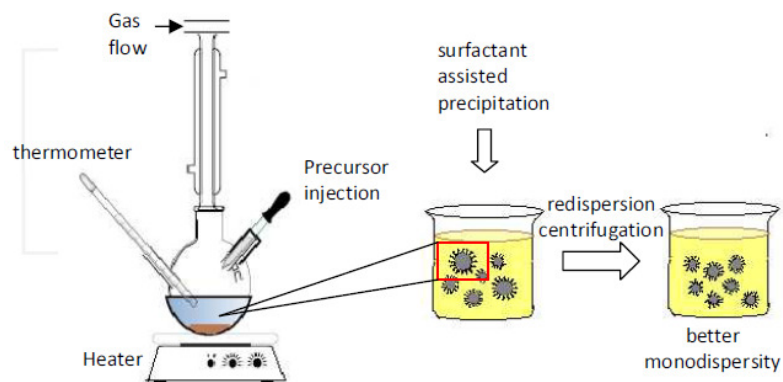


**Figure 1.4:**An illustration of NP synthesis by thermal decomposition process [8].

### **1.3.1.3. Hydrothermal Reaction**

It is another kind of method used to synthesize MNPs. The crystal is grown in hot water under high pressure and in solubilized precursors. The process is done in an equipment called an autoclave, in which the solution containing precursors for crystal growth is processed. A typical Teflon-lined autoclave is shown in Figure 1.5. Precursor solution would be initially prepared and filled into the autoclave. By increasing in the autogenous pressure resulting from heating, reactivity and also solubility of metal precursors are enhanced.

There are several profits of the hydrothermal synthesis compared to the other techniques. For example; It is possible to obtain crystalline materials with high melting points at lower temperatures. Also, it is particularly suitable in that large good-quality crystals can be formed by the hydrothermal method while maintenance of composition control is needed. Possible drawbacks contain the need for high cost autoclaves and lack of observing the crystalline material as it grows. In addition, this technique helps to obtain good crystalline materials and does not require additional treatments after the process.



**Figure 1.5:** Autoclave used for hydrothermal method.

### **1.3.1.4. Microemulsion**

One of the most common technique is microemulsion method. By this technique, micelles and reverse micelles are formed to control the magnetic NPs growth since they behave as tiny reactors. The formation of particles happens through interdroplet dynamic exchange and stabilization of phases is done with the formation of micelles. Wrapping of oil in water droplets in microemulsion is done by the surfactant. Particles are grown in micelles and they



are precipitated by the solvent addition. The size of the micelles are generally dependent on the concentration of the surfactant an water.

### 1.3.1.5. Sol-Gel Method

Another technique for the production of MNPs is sol-gel method. It usually means the conversion from a liquid generally colloidal to a solid state by the hydrolysis and condensation of metal precursors [9]. By subjecting the gels to elevated temperatures, the nanoparticles are formed the final crystalline state. The solvent type, the temperature, type of metal salts and the pH influence the properties of the gel and large quantities of MNPs could be obtained by this method [10]. As seen in Fig. 1.6, this process generally includes the steps as production of the homogen solution, sol, gel, aging, dehydration and condensation [11-13].

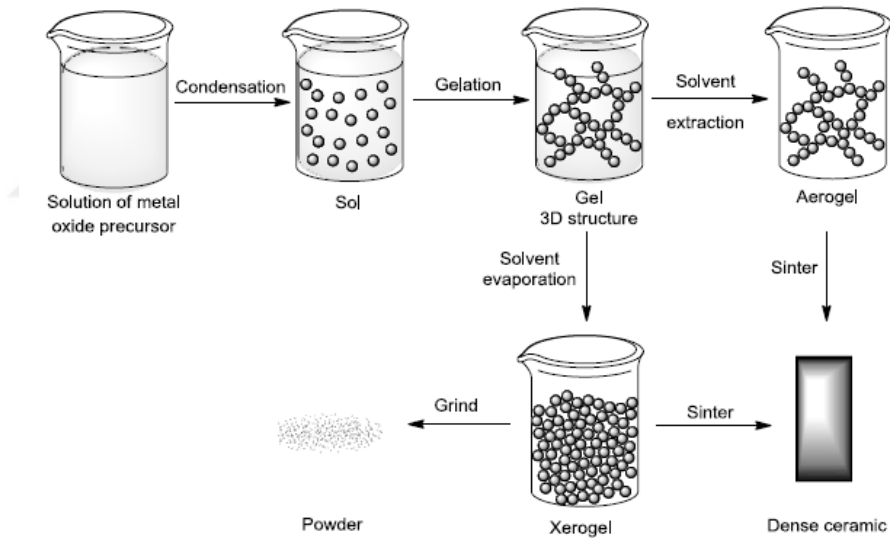


**Figure 1.6:** An illustration of sol-gel reaction.

## 1.4. MAGNETIC PROPERTIES

All matters contain electrons which show a magnetic moment with respect to electron motion. Spin and orbital moment are two classes of electron motion and each of them belongs to its own magnetic moment. If the magnetic features of a sample are considered, the magnetic moment of the atoms should be thought in the sample. To understand the class of magnetism,

it is easy to compare them depending on magnetic moment directions and these are as the following paramagnetism, ferromagnetism and ferrimagnetism.

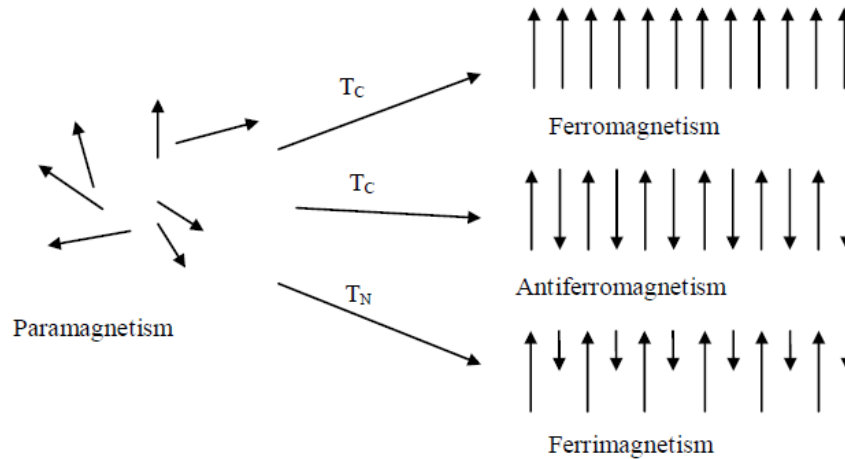


**Figure 1.7:** Different types of magnetic behaviors of materials.

All materials can be categorized with respect to their magnetic behavior based on their response to applied external magnetic field as seen in Fig 1.7. Diamagnetic and paramagnetic elements are usually non-magnetic character whereas ferromagnetic ones are referred as magnetic and they are the most useful ones. Antiferromagnetism is seen in pure elements at room temperature. When it comes to ferrimagnetic property, it is observed in compounds like mixed oxides and spinel ferrites. If a material has a paramagnetic property, the dipole moments are oriented randomly resulting for that the crystal is having a net magnetic moment which is different from zero. If a magnetic field is implemented to this crystal, the crystal would be a small net dipole moment due to the orientation of the some moments. The dipole moments are oriented even without any magnetic field for a ferromagnetic crystal. When it comes to a ferrimagnetic crystal, the net magnetization is the total of individual atomic magnetic moments that are antiparallel each other and have different strengths. When these moments are equal as magnitude, the material behaves as antiferromagnetic and the net magnetic moment is zero.

#### 1.4.1. Hysteresis Loop

A hysteresis loop called as B-H curve gives much data related to the magnetic features of a specimen. Hysteresis loop reflects several magnetic features of the material and the loop is formed by varying magnetic flux density, B, according to the magnetic field strength, H. Fig.

1.8 presents an example of a hysteresis loop in more detail. When the applied magnetic field  $H$  is higher, the stronger magnetic field on the component  $B$  happens. If it is parallel, all spins are almost orientated and an extra increment in the magnetizing force will give rise to a little increase in  $B$ . Then it is said that the sample has obtained the saturation magnetization called by  $M_S$ . When the magnetic field goes to zero, an inductive coercive force will arise to move the curve from saturation point to origin. Now an amount of  $B$  remains in the sample although the magnetizing force is zero. This means the point of remanence and the residual magnetism in the sample. It is observed as  $M_R$  on the Figure 1.8.

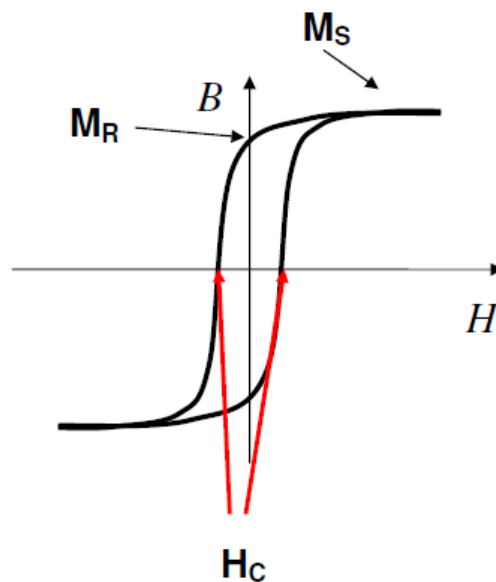


**Figure 1.8:** Example of magnetization curve.

Hysteresis curves are usually in “s” shape type and the magnetizations did not reach the saturation completely. In spite of ferromagnetic samples, superparamagnetic specimens have small coercive field and a magnetization curve increase rapidly up to remanence point ( $M_S$ ) and after this point it follows linearly as the magnetic field increases.

## 1.5. SURFACE MODIFICATION

MNPs have attracted attention for many years they have an unusual catalytic properties. But, the direct application of them in catalysis is not easy because they have a tendency of

agglomeration because of their strong magnetic interactions between each other including attractive (magnetic and dipole-dipole) and repulsive (electrostatic) forces. The surface encapsulating of MNPs is significant in catalysis and organic or inorganic surface functionalization could be. Several approaches have been developed to prepare them and different inorganic and organic supports were utilized to disperse and incorporate them [14, 15]. By coating the magnetic NPs, direct contacts are prevented between particles, therefore, the degree of aggregates will be decreased. Functionalized magnetic NPs are called magnetic nanocomposites which are three dimensional materials incorporated with zero dimensional structures (magnetic nanoparticles). The combination of different components in the nano size range can produce new materials which may combine the advantages of each component each materials. Inorganic-organic hybrid nanocomposite is an example for this type of materials. They are synthesized on a possible matrix like organic layer [16], metal based material [17], carbon [18], and porous silica [19]. The catalytic performance of nanoparticles depends on the active atom which refers to the size and shape. Therefore, the stabilization of MNPs is an essential topic [20]. To overcome these drawbacks, several incorporating methods have been developed. These may be divided into two: (1) incorporating with inorganic structures such as silica or metals oxides and (2) encapsulating with organic materials.

### 1.5.1. Silica

Silica is the most used as an encapsulating agent for the monodisperse MNPs synthesis. Generally, a silica layer does not allow their aggregation and enhances their stabilization. Stabilization of magnetite nanoparticles by silica coating agent occurs by two routes containing the dipole interactions with the silica layer and the coulombic repulsion of the MNPs since silica NPs are negatively charged. The sol-gel method is the process to coat the MNPs with silica which is commonly known Stöber technique [21]. For example; Philipse et al. reported that the silica layer on the MNPs enhances its colloidal stability and prevents magnetic clusters formation [22]. In another study, Karimi synthesized H<sub>2</sub>SO<sub>4</sub> functionalized silica coated MNPs and the prepared sample was used as an effective catalyst in excellent yields (Fig. 1.9) [23].

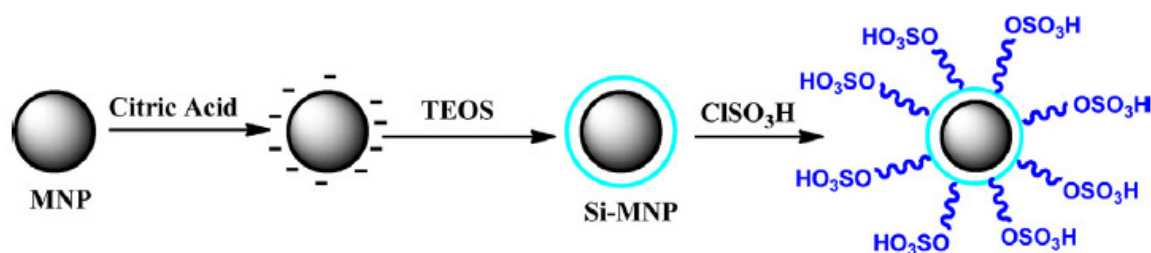


**Figure 1.9:** Representation for the synthesis of silica coated MNPs [23].

### 1.5.2. Polymers

Various organic polymers like hydrophobic or hydrophilic structure can be thought. Also, they can be neutral or charged. They can be also categorized into as natural or synthetic polymers. Chitosan is one of the most used natural polymer for coating of MNPs since it is cheap, nontoxic and hydrophilic. Y. Chang have showed that the formation of 14 nm sized chitosan coated MNPs by carboxymethylation of chitosan and then carbodiimide activation covalently [24]. J. Zhi et al. reported an efficient way for the preparation of chitosan-magnetite nanocomposites by microemulsion technique [25]. As unnatural polymers like PEG, PVA and PVP are the most popular used ones. Sometimes, to increase the water solubility of magnetic nanoparticles other organic molecules like oleic acid or oleylamine are also preferred. PEG is a kind of neutral and hydrophilic polymer and connected to various surfaces by its functional groups. The stability and solubility in aqueous mediums PEG coated MNPs have high quality. PVA is another kind of synthetic hydrophilic polymer and coating with PVA increases the colloidal stability. However, PVA does not connect reversibly to magnetic NPs surface due to interconnection with interface.

### 1.6. CATALYSIS

In many situations, the production of waste is associated with the use of a stoichiometric amount of reagents. Catalysis can enhance the efficiency of a process by reducing the required energy and preventing the use of stoichiometric amount of reagents with the greater product selection. This indicates less energy and waste [26]. In addition, it often helps to open the door to significant innovations for chemical reactions and allow nonconventional approaches to traditional chemical difficulties. Thus, catalysis is important in the fabrication of chemicals, especially in the synthesis of bulk materials and fine chemicals. The concepts of a catalytic reaction refers that a catalyst

accelerates the reaction without getting consumed in the reaction. The catalyst offers an alternative, lower energy, route over the activation barrier. Although the catalysed reaction path may be more complex, the lower activation costs makes the alternative path energetically favourable. However, even though the activation energy is lower with a catalyst, the overall free energy change is the same for the catalysed reaction as for the uncatalysed. A schematic picture over the catalysed reaction could be shown in Figure 1.10.

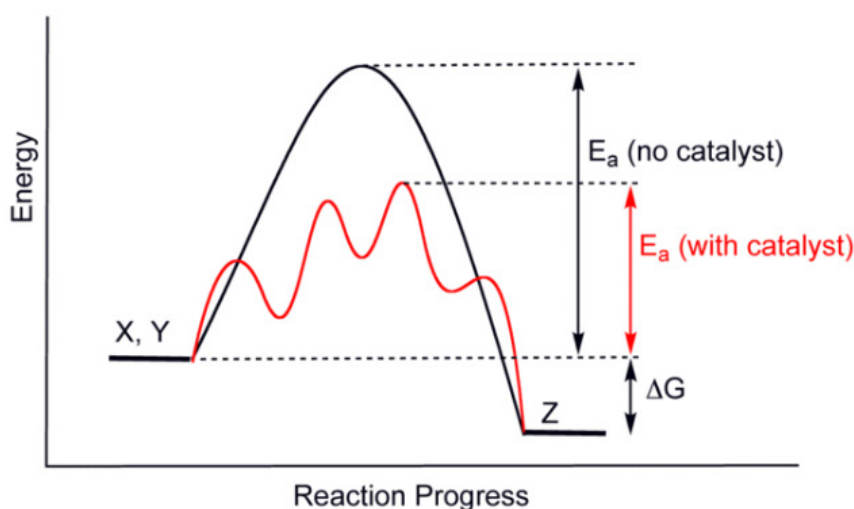


**Figure 1.10:** A representation for the catalyzed pathway [27].

If we can restrict ourselves to metal oxide based catalysts, we can categorize into two types catalysis: heterogeneous and homogeneous catalysis.

### 1.6.1. Homogeneous Catalysis

In homogeneous catalysis, all the reactants and catalysts are present in the same phase. They are the simple molecules like  $\text{H}_2\text{SO}_4$  or  $\text{Mn}^{+2}$  or organometallic complexes. Generally, they are more active and selective. Catalytic chemistry and mechanism for homogeneous catalysis are better studied and understood and thus it is easy to control the reaction parameters. Also, since the reactants and catalysts exist in same phase, the diffusion rate is very high but the homogeneous catalyst is not recyclable after the reaction thus the separation of them is difficult.

### 1.6.2. Heterogeneous Catalysis

Heterogeneous catalysis is associated with the catalysis where the reacting and the catalytic species are in different thermodynamic phases. It is a vital part of the chemical industry and it is essential for it to evolve and to be economical. In catalysis, heterogeneous catalysts have been prepared using nanoparticles with a specific size which should be possible for its various applications. Magnetic filtration is a “green” step because it prevents the difficulties like filtration, loss of catalyst or oxidation of metal compounds. Therefore, waste and costs can be importantly decreased and Figure 1.11 represents magnetic separation example of the catalyst in a laboratory scale.

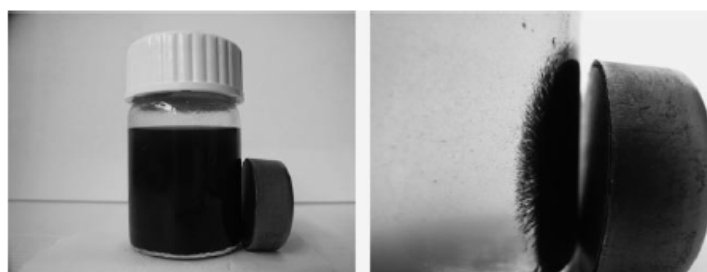


**Figure 1.11:** Magnetic filtration of dispersed MNPs (left: the application of the magnet immediately; right: a short time later).

Today, researchers are finding to do better with different methods to associate the properties of homogeneous and heterogeneous catalysts. The aim is a highly efficient, low cost and stable catalyst with high product selectivity [28, 29].

### 1.6.3. Catalytic Applications of Magnetic Nanocomposites

In order to associate the excellent catalytic performance with magnetic filtration ability, magnetic noble metal nanocatalysts are investigated [30, 31]. Magnetic nanoparticles with polymeric supports are considered one of the best candidates owing to their unique catalytic properties for the removal of organic pollutants thus they have been investigated worldwide by the researchers to find out the most effective catalytic materials.

For example; Cheng and co-workers fabricated a kind of magnetic composite gel with the improved adsorption performance for methyl blue and methyl violet dyes. Their experimental results demonstrated that the combination of polyvinyl alcohol and graphene with magnetic core offered an effective way to generate versatile composite (Figure 1.12) [15].

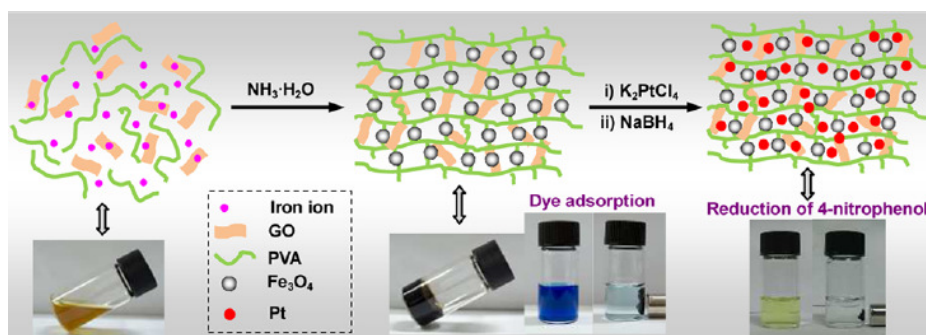


**Figure 1.12:** A representation for the magnetic gel composite preparation[15].

In addition,  $\text{Fe}_3\text{O}_4@\text{SiO}_2\text{-Ag}$  nanocomposites were generated by Jiang and his co-workers. These magnetic nanocomposites were rapid and efficient for organic contaminants and can be used many times by magnetic filtration [32]. As a result, the application of the magnetically recyclable nanocatalysts is widely investigated by the researchers for the reduction of various organic compounds since this chemical transformation is important for the fabrication of a large scale of products.

### 1.7. DYES

A wide range of organic dyes are available in different industrial sectors, like dye synthesis, paper making, printing, food, cosmetic and textiles. For example, more than  $1.47 \times 10^6$  tons of organic dyes were generated in China in 2010. Irrespective of the enormous consumption, however, it is thought that 10–15% of the dyes have been thrown away in the dyeing processes. The discharged organic dyes' solubility is high in water and not easy to remove from the water due to their lack of biodegradability. Also, they are both toxic and carcinogenic to aquatic living organisms and would endanger the environment [33, 34]. The existence of even less than 1 ppm of these organic pollutants is quite visible and needless. Thus, the adsorption of them has been thought as the most significant global concerns. For this reason, many decolorization techniques have been applied so far like coagulation, filtration, adsorption, photocatalysis, etc. [14, 35-38]. The adsorption technique gives the best results and is more popular. As a result, it is believed that a high adsorption capacity and rate, low cost and easy separation may allow a better solution for the global concern of organic pollutants' adsorption from the water [14, 15].



## 2. MATERIALS AND METHODS

### 2.1. CHEMICALS

Iron(II) chloride tetrahydrate ( $\text{FeCl}_2 \cdot 4\text{H}_2\text{O}$ ),  $\text{Fe}(\text{NO}_3)_3 \cdot 9\text{H}_2\text{O}$ , Copper(II)Sulphate ( $\text{CuSO}_4$ ), ( $\text{Mn}(\text{NO}_3)_2 \cdot 4\text{H}_2\text{O}$ ), iron (III) chloride hexahydrate ( $\text{FeCl}_3 \cdot 6\text{H}_2\text{O}$ ), silver Nitrate ( $\text{AgNO}_3$ ), sodium borohydrate ( $\text{NaBH}_4$ ), nitric acid ( $\text{HNO}_3$ ), hydrochloric acid ( $\text{HCl}$ ), ammonia solution ( $\text{NH}_4\text{OH}$ , 30%), sulfuric acid ( $\text{H}_2\text{SO}_4$ ) were all obtained from Sigma. Aniline, ammonium peroxydisulfate (APS), histidine (His), nicotinic acid (Nico), tetraethyl orthosilicate (TEOS), oleic acid, polyvinylpyrrolidone (PVP), vaseline oil, Tween20, methyl acrylate, ethylene diamine, methyl orange (MO), (3-aminopropyl) triethoxysilane (APTES), methyl blue (MB) were purchased from Merck. Rhodamine B (RhB), eosin Y (EY) and all nitro aromatic compounds were all obtained from Sigma.

### 2.2. INSTRUMENTATIONS

FTIR spectroscopy was performed by the attenuated total reflection (ATR) method. The spectra of the samples were recorded in the range of 4000 and 400  $\text{cm}^{-1}$ .

The crystal structure of the materials was estimated by X-ray diffraction (XRD) on a Rigaku using Cu  $K\alpha$  radiation between 3° and 80°.

Thermogravimetric analysis (TGA) was conducted under nitrogen atmosphere using STA 6000 TGA (Perkin Elmer) in the temperature range of 30-800°C with a heating ramp of 5°  $\text{min}^{-1}$ .

The scanning electron microscope (SEM, Philips XL30 SFEG) at an operational voltage of 15 kV was used to investigate the morphology of the materials.

Transmission electron microscope (TEM, FEI Tecnai G2 Sphera) was used. Analysis was performed after alcohol evaporation. Several micrographs at different magnifications were used to calculate particle size distribution histogram counting a minimum of 100 particles.

Field and temperature dependence of magnetization were performed by vibrating sample magnetometer (LDJ Electronics Inc. Model 9600) with an applied field of 15 kOe.

UV-Vis spectroscopy (Perkin Elmer Lamda 35 model) was used to investigate the optical properties of the nanomaterials.

## 2.3. PROCEDURE

### 2.3.1. Preparation of Fe<sub>3</sub>O<sub>4</sub> @ Tween-Ag Magnetic Hybrid

To obtain the iron oleate complex, oleic acid and Fe<sup>3+</sup> chlorides were used. The reaction was initiated with 10 mmol FeCl<sub>3</sub>.6H<sub>2</sub>O in ethanol and 1 ml of oleic acid. After, 0.3 M NaOH in ethanol was added into this reaction drop by drop and the solution was refluxed for 3h at 200°C and then iron oleate complex was dried at 80°C. Obtained iron oleate, suitable amount of vaseline oil and Tween20 were stirred in the presence of argon atmosphere at 350 °C. The obtained Fe<sub>3</sub>O<sub>4</sub>@Tween20 magnetic nanocomposite was dispersed in 20 ml of 0.033M Ag(NH<sub>3</sub>)<sub>2</sub>NO<sub>3</sub>. 100 mg of PVP was dissolved in ethanol was transferred into this mixture and refluxed at 70°C. Schematic representation was shown in Figure 2.1.

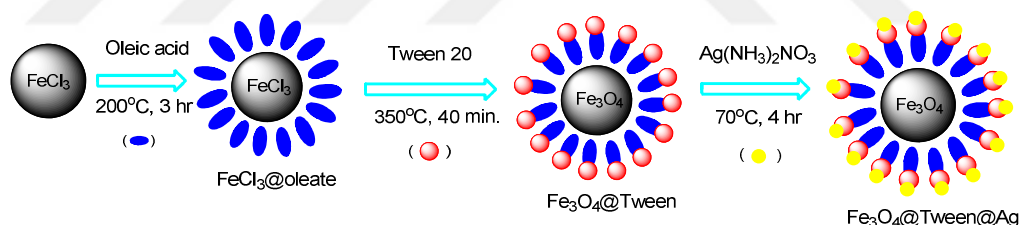


**Figure 2.1:** Synthesis protocol of the Fe<sub>3</sub>O<sub>4</sub>@Tween20-Ag magnetic hybrid.

### 2.3.2. Preparation of Fe<sub>3</sub>O<sub>4</sub>@His-Cu and Fe<sub>3</sub>O<sub>4</sub>@His-Ag Magnetic Hybrids

Fe<sub>3</sub>O<sub>4</sub>@His samples were fabricated by the preparation of metal salts and their decomposition. An appropriate amount of histidine was added into metal salts mixture. To precipitate ferrites and also to adjust pH level to 10, ammonium hydroxide was added slowly. After, it was kept in Ar to transform the solution into black precipitates. In this part, 50 mg Fe<sub>3</sub>O<sub>4</sub>@Histidine was mixed with 50 ml of distilled water with a constant ultrasonication and was added into the CuSO<sub>4</sub> solution (30 ml, 0.2 mmolL<sup>-1</sup>) followed by the addition of NaBH<sub>4</sub>. Suggested linkage was estimated as in Figure 2.2.

Same method was done for the fabrication of  $\text{Fe}_3\text{O}_4\text{@His-Ag}$  nanocatalyst, the only difference was the usage of 0.2 mmol/L  $\text{AgNO}_3$  instead of 0.2 mmol/L  $\text{CuSO}_4$  solution.

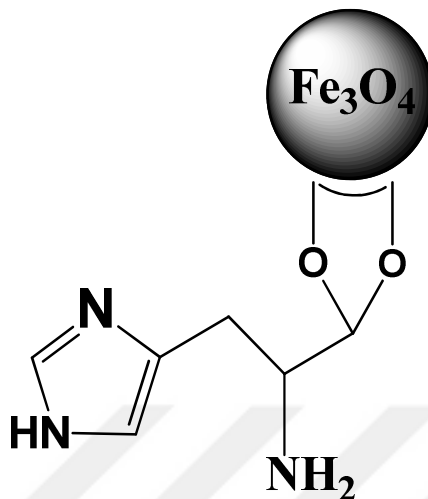


**Figure 2.2:** Suggested coordination of histidine to  $\text{Fe}_3\text{O}_4\text{@His}$  magnetic nanoparticle surface.

### 2.3.3. Preparation of $\text{Fe}_3\text{O}_4\text{@Nico-Ag}$ and $\text{Fe}_3\text{O}_4\text{@Nico-Cu}$ Magnetic Hybrids

$\text{Fe}_3\text{O}_4$  was synthesized by standard thermal decomposition technique in which iron salts were dissolved in water and added  $\text{NH}_3$  solution as the precipitating agent. pH was almost at 10 with further addition of  $\text{NH}_3$  solution and the solution was refluxed with  $\text{N}_2$  flow at  $100^\circ\text{C}$  for 2h. Then, stoichiometric amount of nicotinic acid was mixed homogeneously and kept in reflux for 5h. After it was cooled down to room temperature, washing process was done with water and ethanol to obtain  $\text{Fe}_3\text{O}_4\text{@Nico}$  nanocomposite. Then, 150 mg of the  $\text{Fe}_3\text{O}_4\text{@Nico}$  nanocomposite was used in required amount of water with sonication. By adding 0.2 mmol/L of 30 ml  $\text{AgNO}_3$  solution and 0.6 g of  $\text{NaBH}_4$ , the solution was kept by stirring for 3h at r.t. Formation process was illustrated in Figure 2.3.  $\text{Fe}_3\text{O}_4\text{@Nico-Cu}$  magnetic hybrid was prepared in the same way except that 0.2 mmol/L of 30 ml of copper(II)nitrate solution was added as the copper source as shown in Fig. 2.4.

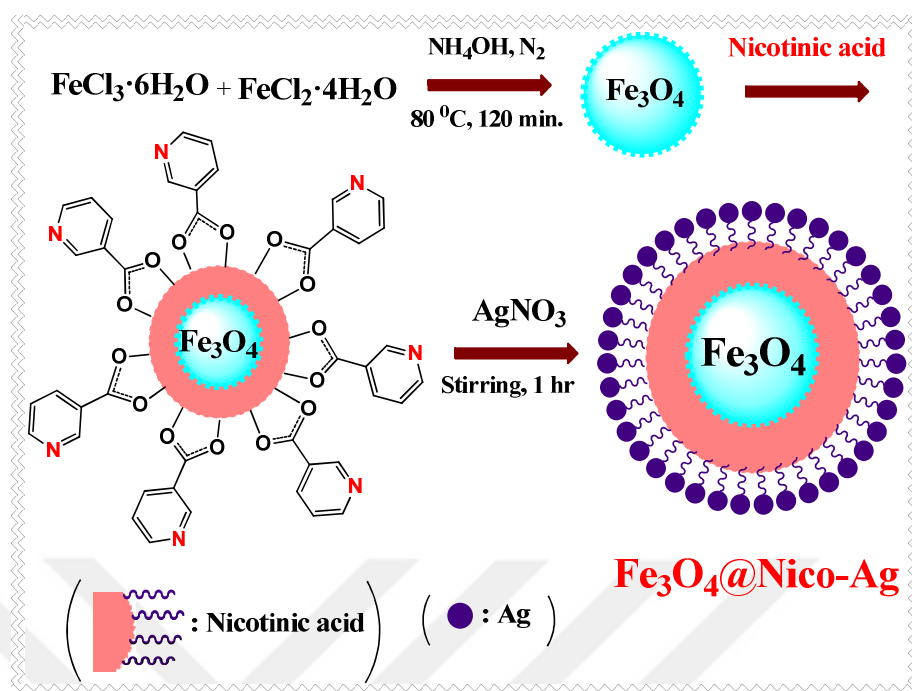


Figure 2.3: Formation process of the  $\text{Fe}_3\text{O}_4 @ \text{Nico-Ag}$  magnetic hybrid.

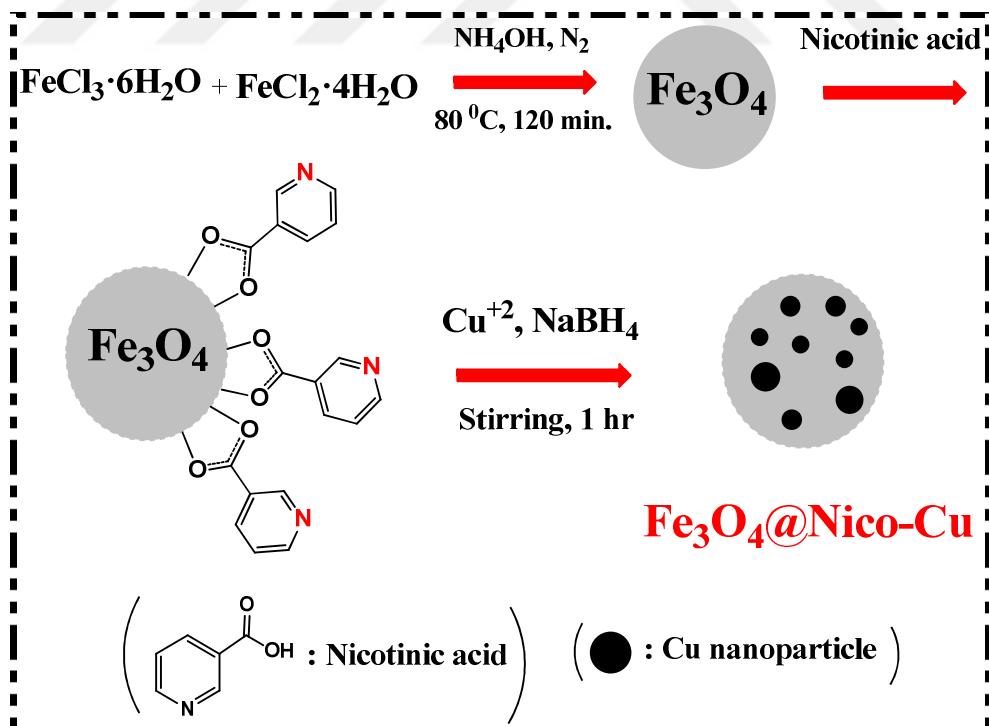


Figure 2.4: Formation process of the  $\text{Fe}_3\text{O}_4 @ \text{Nico-Cu}$  magnetic hybrid.

### 2.3.4. Preparation of MnFe<sub>2</sub>O<sub>4</sub>@PANI-Ag and MnFe<sub>2</sub>O<sub>4</sub>@SiO<sub>2</sub>-Ag Magnetic Hybrids

Thermal decomposition method was used to synthesize manganese ferrite samples. All the reagents used in this synthesis are commercially available and were used as received without further purification. Appropriate amounts of metallic salts were mixed with water and pH was almost at 10 by the concentrated ammonia solution. Then, the mixed solution was slowly heated up to reflux at 100°C for 5h under N<sub>2</sub> gas flow and stirring condition. After the solution was cooled down to r.t., the dark brown precipitates were collected with magnetic filtration.

The as-prepared MnFe<sub>2</sub>O<sub>4</sub> NPs were polymerized to obtain MnFe<sub>2</sub>O<sub>4</sub>@PANI nanocomposite. In this typical procedure, 0.1 mol/L aniline was mixed in 0.125 M of APS which is dissolved in 0.1 mol/L HNO<sub>3</sub> nitric acid and 50 ml of this solution was stirred with spinel manganese ferrites. For the polymerization of aniline, the solution was put into an ice bath with stirring during 24h at -4°C. Obtained material was as green color.

MnFe<sub>2</sub>O<sub>4</sub>@PANI-Ag magnetic hybrid was synthesized by the in-situ reduction method. Briefly, MnFe<sub>2</sub>O<sub>4</sub>@PANI was ultrasonically dispersed in H<sub>2</sub>O (50ml) followed by addition of AgNO<sub>3</sub> (30ml, 0.2M). After being stirred for about half an hr, NaBH<sub>4</sub> (0.6g) was added to the mixture and then Ag NPs were formed on the PANI coated MnFe<sub>2</sub>O<sub>4</sub> as outlined in Figure 2.5. Finally, the MnFe<sub>2</sub>O<sub>4</sub>@PANI-Ag nanocomposite was collected by magnetically.

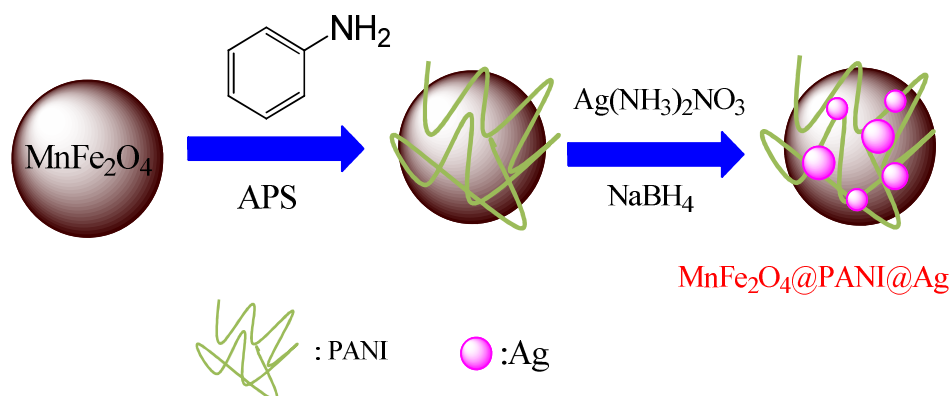


**Figure 2.5:** Synthesis route for the MnFe<sub>2</sub>O<sub>4</sub>@PANI-Ag.

The other experiment is the modification of  $\text{MnFe}_2\text{O}_4$  NPs with the  $\text{SiO}_2$ .  $\text{MnFe}_2\text{O}_4$  nanoparticles were coated by the following procedure: Dispersed  $\text{MnFe}_2\text{O}_4$  NPs and TEOS (6 ml) were mixed with mechanical stirring for about 4h at  $40^\circ\text{C}$ . The product  $\text{MnFe}_2\text{O}_4@\text{SiO}_2$  was isolated and dried in an oven. To introduce  $\text{Ag}^+$  onto  $\text{MnFe}_2\text{O}_4@\text{SiO}_2$ ,  $\text{MnFe}_2\text{O}_4@\text{SiO}_2$  was mixed with  $\text{AgNO}_3$  (30 mL, 0.2M) for 24 h at  $35^\circ\text{C}$  by stirring and reduced by excess amount of  $\text{NaBH}_4$  (0.6g).  $\text{MnFe}_2\text{O}_4@\text{SiO}_2\text{-Ag}$  nanocomposite was thus obtained after washing process (Fig. 2.6.).

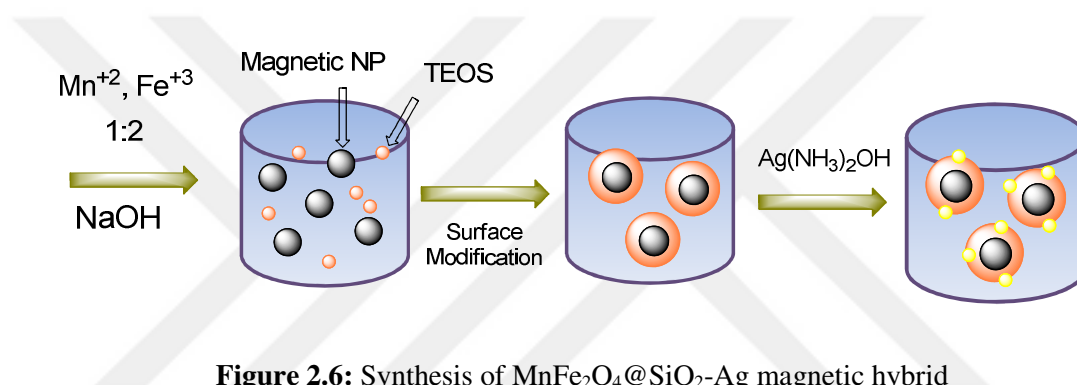


**Figure 2.6:** Synthesis of  $\text{MnFe}_2\text{O}_4@\text{SiO}_2\text{-Ag}$  magnetic hybrid

### 2.3.5. Preparation of $\text{Fe}_3\text{O}_4@\text{PAMAM}(\text{G}1)\text{-Ag}$ Magnetic Hybrid

Two different solutions of  $\text{FeCl}_3\cdot\text{H}_2\text{O}$  and  $\text{FeSO}_4\cdot 7\text{H}_2\text{O}$  (as the molar ratio are two) were prepared. pH was almost 10 with the concentrated  $\text{NH}_3$  solution. The solution was refluxed at  $80^\circ\text{C}$  by stirring under  $\text{N}_2$  atmosphere to protect the product from any oxidation. The final solution was cooled down to r.t., washed with ethanol. After,  $\text{Fe}_3\text{O}_4$  was dispersed in  $\text{EtOH}/\text{H}_2\text{O}$  mixture and was mixed with 3-aminopropyl-triethoxysilane, APTES. The mixture was kept at  $400^\circ\text{C}$  for 8 hr and then collected and dried in vacuum.

According to the techniques proposed by Liu and Pan,  $\text{Fe}_3\text{O}_4@\text{PAMAM}(\text{G}1)$  was formed [39, 40]. To produce  $\text{Fe}_3\text{O}_4@\text{PAMAM}(\text{G}1)\text{-Ag}$ , Ag NPs were encapsulated onto the surface  $\text{Fe}_3\text{O}_4@\text{PAMAM}(\text{G}1)$  nanocomposite with in-situ wet chemistry method as shown in Figure 2.7. During the in-situ coating, 0.06 g of  $\text{Fe}_3\text{O}_4@\text{PAMAM}(\text{G}1)$  was dispersed in  $3 \times 10^{-2}$  M of  $\text{Ag}(\text{NH}_3)_2\text{NO}_3$  solution. Afterwards, it was mixed with ethanol which contains 100 mg of PVP under stirring and kept for reflux for 4h at  $70^\circ\text{C}$ . The resulting products were separated and washed and dried in air overnight.

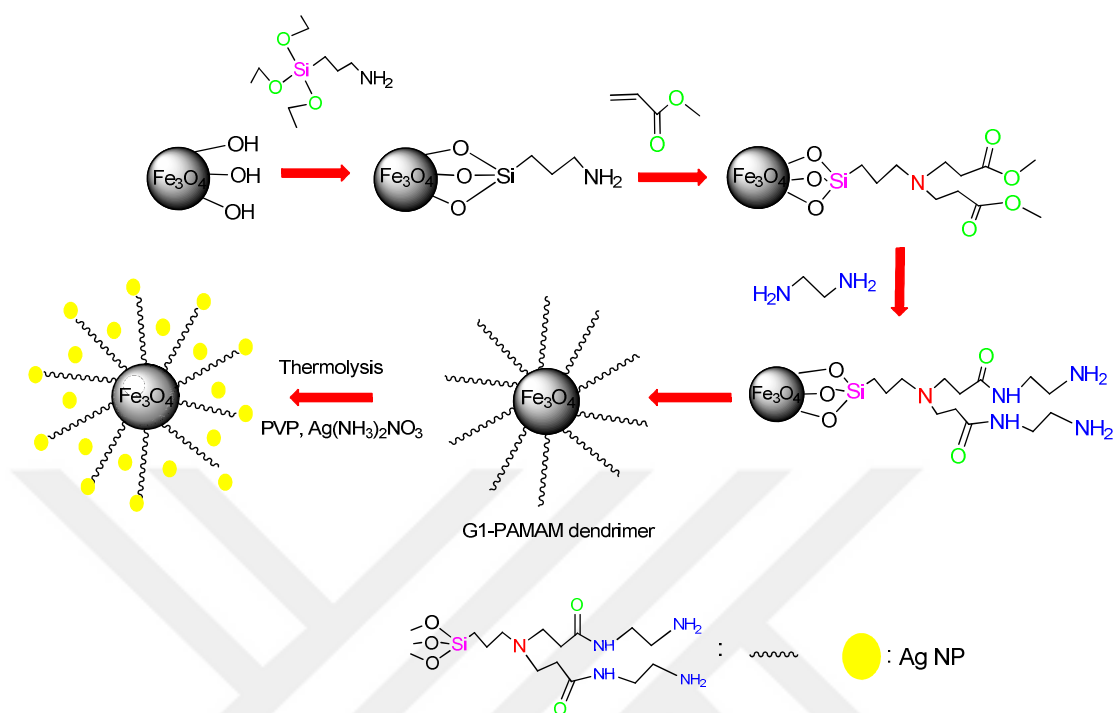


**Figure 2.7:** Formation process of the Fe<sub>3</sub>O<sub>4</sub>@PAMAM(G1)-Ag magnetic hybrid.

## 2.4. CATALYTIC STUDIES

In a typical reduction reaction, a suitable amount of magnetic nanocatalysts (1-5 mg) were added into the mixture of aromatic nitro compounds or azo dyes solution (100  $\mu$ l, 0.005 mol/l), fresh NaBH<sub>4</sub> solution (1ml, 0.2mol/ml), and 2 ml of distilled water in a quartz cuvette. Then, the solution was quickly subjected to UV-vis absorption spectrophotometer and the progress of the decolorization reaction was monitored. When the reaction was completed, the magnetic catalysts were easily removed from the solution by a magnet.

### 3. RESULTS

#### 3.1. ANALYSIS OF MAGNETIC NANOCATALYSTS

##### 3.1.1. Characterization Results of Fe<sub>3</sub>O<sub>4</sub>@Tween20-Ag Magnetic Hybrid

XRD curve of the Fe<sub>3</sub>O<sub>4</sub>@Tween20-Ag magnetic hybrid was shown in Figure 3.1a. The reflection peaks could be as Fe<sub>3</sub>O<sub>4</sub> in a cubic phase (JCPDS no. 19-629). Based on the highest intensity peak of (311), the mean grain size of the sample was almost 11 nm [41, 42]. No peaks from any impurities were seen in the XRD spectrum.

FTIR spectra of Ag loaded Fe<sub>3</sub>O<sub>4</sub>@Tween20-Ag nanocomposite (curve I), Tween-20 (curve II), oleic acid (curve III) and bulk Fe<sub>3</sub>O<sub>4</sub> (curve IV) were represented in Fig. 3.1b. The typical bands of Fe<sub>3</sub>O<sub>4</sub> at 570-590 cm<sup>-1</sup> can be seen in both Fig. 3.1b (curve I) and (curve IV), confirming that the Fe<sub>3</sub>O<sub>4</sub> NPs were protected after coating process [43-45]. The peak at ~ 1120 cm<sup>-1</sup> was the evidence of ether in Tween-20 and the signals at 2838 and 2905 cm<sup>-1</sup> were assigned to the absorption of C-H bond of oleic acid and Tween20 [46, 47]. Obviously, it can be explained as Fe<sub>3</sub>O<sub>4</sub> NPs were conjugated with oleic acid and Tween20.

The magnetization of the as-synthesized product was shown in Fig. 3.1c and can be observed that the obtained Fe<sub>3</sub>O<sub>4</sub>@Tween20-Ag nanocatalyst showed a superparamagnetic hysteresis loop with the saturation moment of almost 24 emu/g at room temperature, while lower moment of 92 emu/g is obtained from the bulk magnetite (Fig.1)[48]. This reduction is probably due to the surfactant's diamagnetic property and Ag NPs. Also, the core diameter was found to be almost as  $D_m = 16.5$  nm [44].

Fig. 3.1d showed the thermal behaviour of Fe<sub>3</sub>O<sub>4</sub>@Tween20-Ag nanocatalyst consisting of Fe<sub>3</sub>O<sub>4</sub>, oleic acid, Tween20 and Ag NPs. The weight loss was probably due to iron oxidation up to a temperature of 265°C. No significant weight loss was shown after 400 °C because of the existence of Fe<sub>3</sub>O<sub>4</sub> and Ag NPs and there was a thermal decomposition of the both oleic acid and Tween20 as observed in the DTA curve. Based on the TG curve, the weight residues of the organic parts were estimated to 35%.



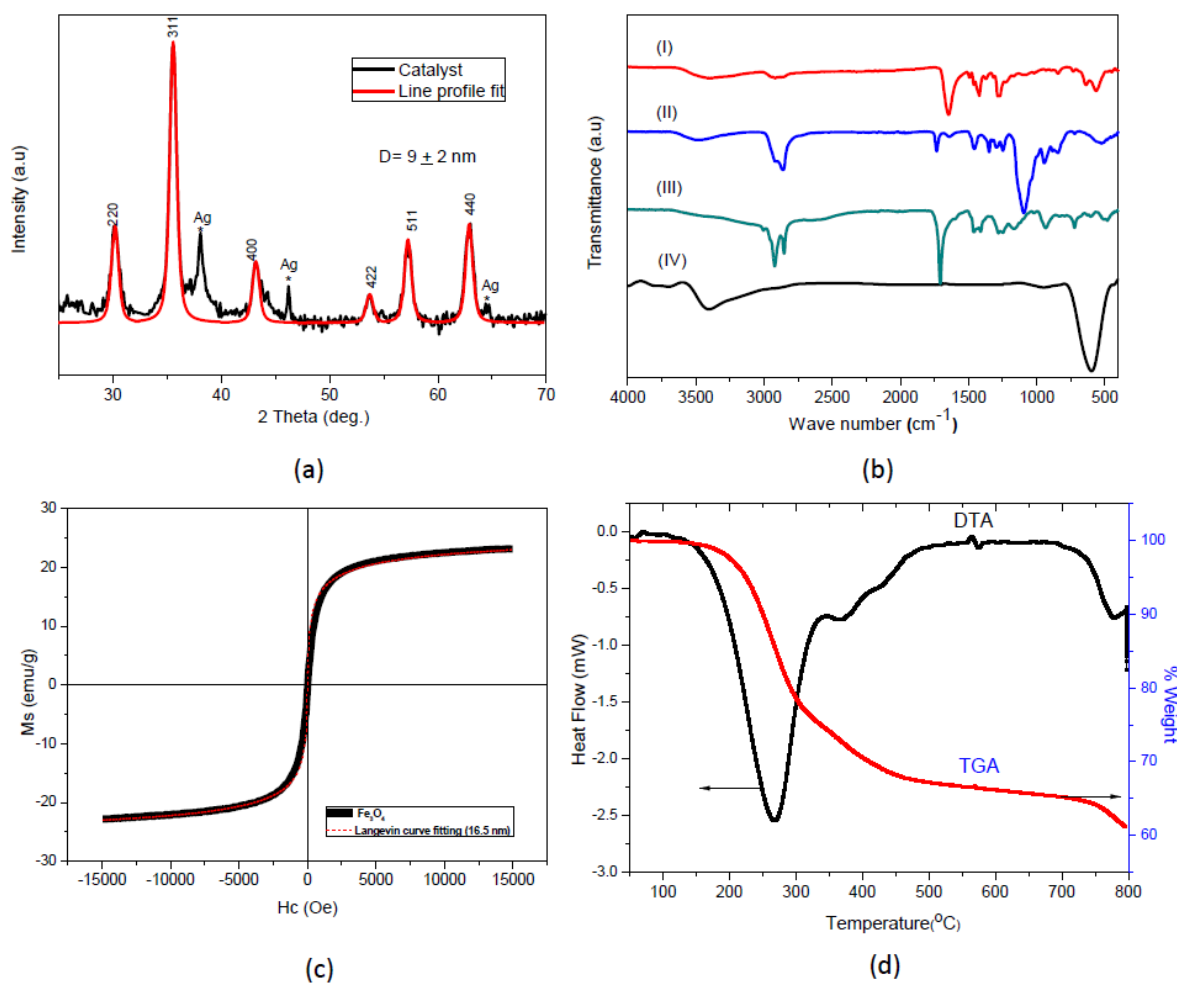


**Figure 3.1:** (a) XRD of Fe<sub>3</sub>O<sub>4</sub>@Tween20-Ag, (b) FTIR (I) Fe<sub>3</sub>O<sub>4</sub>@Tween20-Ag, (II) Tween-20, (III) Oleic acid and (IV) bare Fe<sub>3</sub>O<sub>4</sub> (c) magnetic hysteresis curve, (d) TG-DTA thermograms.

The morphological features of the prepared  $\text{Fe}_3\text{O}_4@\text{Tween20-Ag}$  magnetic hybrid were shown in Fig. 3.2. It was observed that that the product had many uniformly dispersed spheres and the diameters were almost 10 nm. EDX analysis suggested the elements in the product and its result confirmed that Ag, Fe, and C were present in the product. Overall, it proved that magnetic  $\text{Fe}_3\text{O}_4$  NPs was succesfully coated by Tween20 and  $\text{AgNO}_3$ .

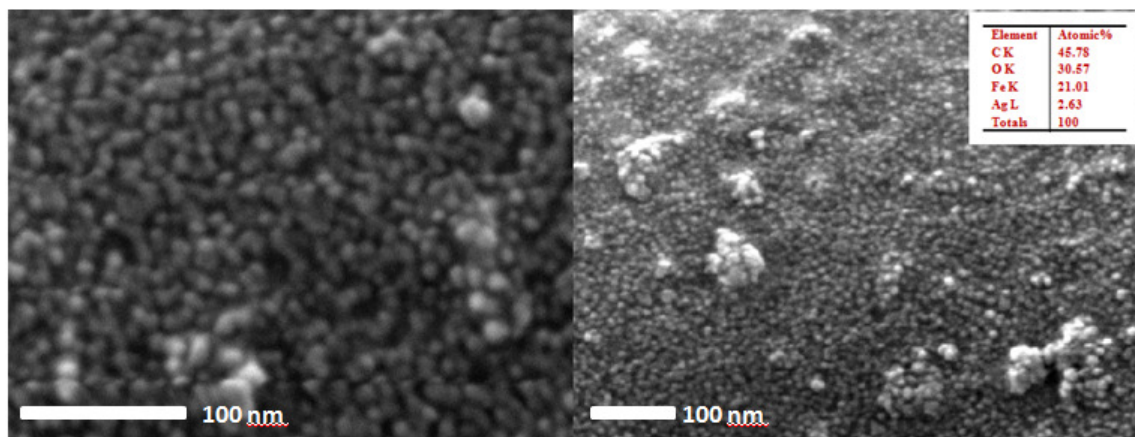
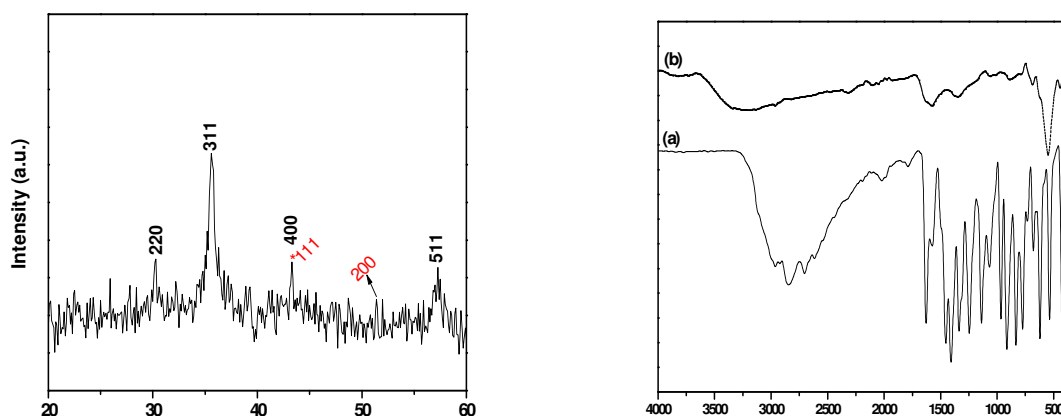


**Figure 3.2:** SEM micrographs of  $\text{Fe}_3\text{O}_4@\text{Tween20-Ag}$  nanocomposite with EDX result.

### 3.1.2. Characterization Results of $\text{Fe}_3\text{O}_4@\text{His-Cu}$ Magnetic Hybrid

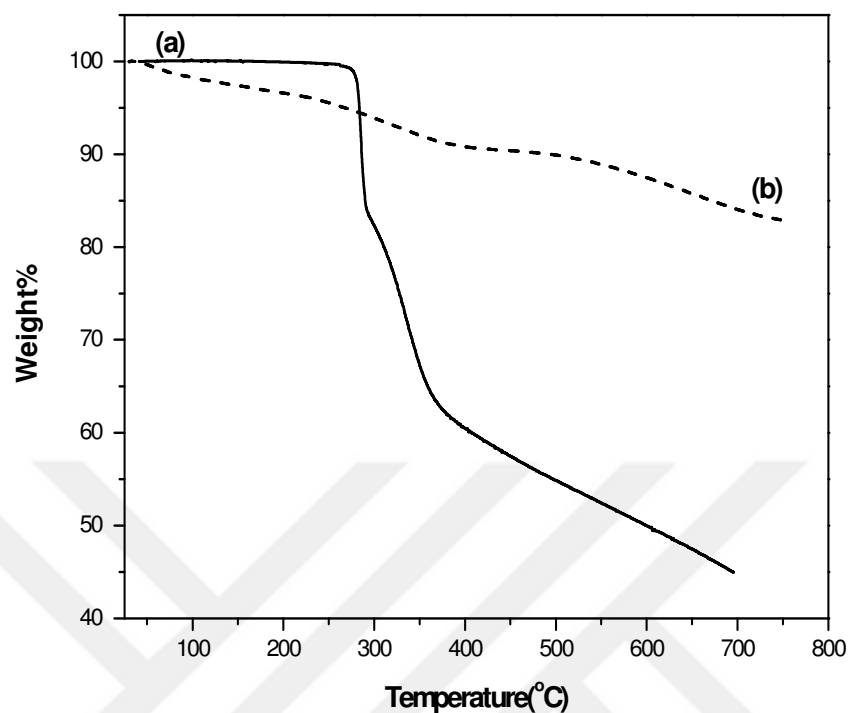
The phase investigation of the  $\text{Fe}_3\text{O}_4@\text{His-Cu}$  magnetic hybrid was illustrated in Fig. 3.3(I). All the diffractions indexed with the structure of  $\text{Fe}_3\text{O}_4$  (JCPDS no. 19-620) [49, 50]. Additionally, it was observed that the peaks for the (111) and (200) planes belong to the cubic Cu NPs (\*marked peaks belong to Cu and JCPDS no. 04-0836) [51]. The average crystallite sizes were estimated to be as almost 12 nm.

FTIR spectrum of His and  $\text{Fe}_3\text{O}_4@\text{His@Cu}$  were shown in Fig. 3.3(II). The signals at 3059, 2923 and  $1450\text{ cm}^{-1}$  were related to the stretching and bending vibrational modes of  $-\text{CH}_2$ . The signal at  $570\text{ cm}^{-1}$  was due to the metal-oxygen bonds in magnetite (Fig. 3.3(II)). There is an indication of complexation between  $\text{Fe}_3\text{O}_4$  and  $\text{COO}^-$  functional groups of His. The peaks at 1607 and  $1392\text{ cm}^{-1}$  were related to the carbonyl groups, respectively. Also, the intensity at  $\sim 3400\text{ cm}^{-1}$  was owing to the  $-\text{NH}$  vibrations of some aminocarboxylates since His provided  $-\text{NH}_2$  groups for binding of  $\text{Cu}^{2+}$ . All these results confirm that  $\text{Fe}_3\text{O}_4$  NPs were coated with His succesfully[52].



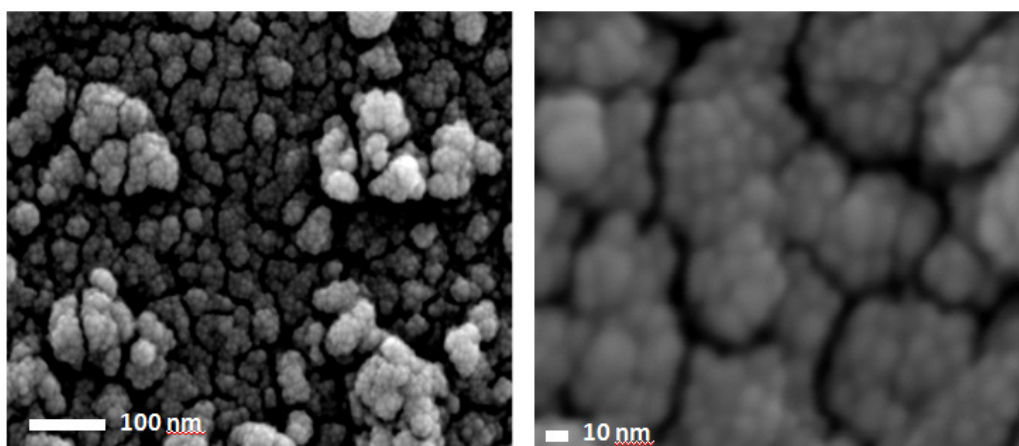
**Figure 3.3:**(I) XRD powder pattern of Fe<sub>3</sub>O<sub>4</sub>@His@Cu and (II) FTIR spectra of (a) His and (b) Fe<sub>3</sub>O<sub>4</sub>@His-Cu.

We conducted TG analysis as shown in Figure 3.4 to reveal the amount of organic part, which is His, in the product. Here, it was found that the weight loss occurred in two parts for L-His and it degraded through the following two steps as seen in Fig 3.4a. The first weight loss was 13% due to the evaporation of H<sub>2</sub>O at ~250 °C and the second weight loss of 57 % was corresponded to the organic backbone decomposition at ~370 °C. Then, it was clear that there were three main stages for the weight loss in Fig 3.4b. It revealed that the primary weight loss of product happened at 25°C-210°C, which could be ascribed to the separation of chemisorbed H<sub>2</sub>O. The other loss became between 215 and 380°C should correspond to the degradation of side groups and the final loss was at 390°C-750°C which was ascribed to the decomposition of organic parts. As a result, the organic content in the product was estimated to be as ~17%.



**Figure 3.4:** TG thermograms of (a) Histidine and (b) Fe<sub>3</sub>O<sub>4</sub>@His-Cu magnetic hybrid.

The morphological analysis of the prepared sample was investigated at different magnifications. Fig. 3.5 showed that Fe<sub>3</sub>O<sub>4</sub> NPs with about 10 nm in diameter were agglomerated by fabricating about 50-100 nm globules. The EDX spectrum of the Fe<sub>3</sub>O<sub>4</sub>@His@Cu was also seen in Fig. 3.5 meaning the presence of Fe, N, Cu in the sample.



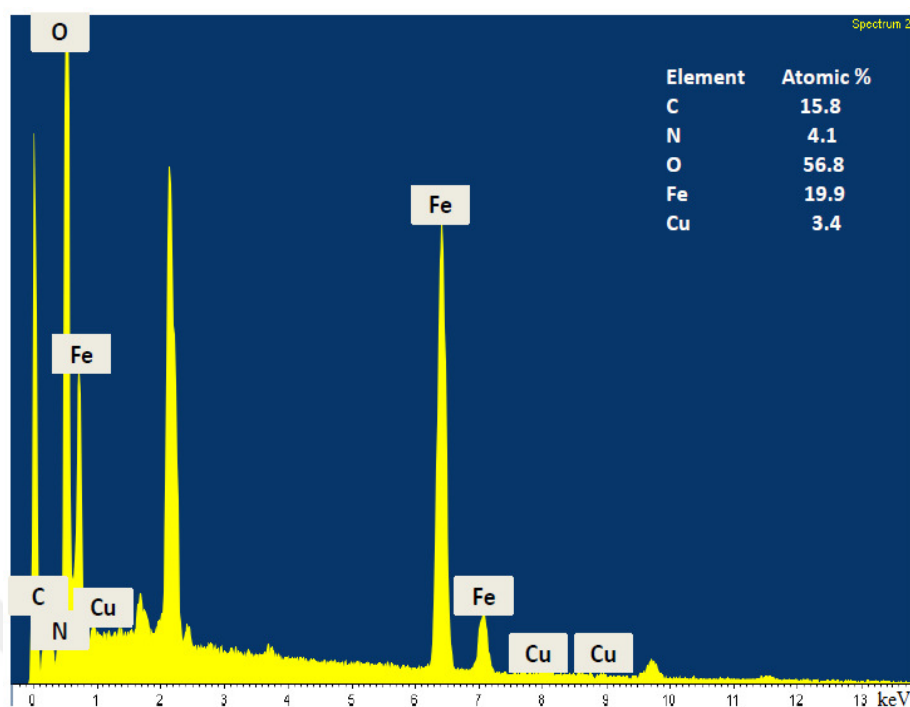


**Figure 3.5:** SEM micrographs and EDX spectra of  $\text{Fe}_3\text{O}_4@$ His-Cu magnetic nanocomposite at various magnifications.

Fig. 3.6 represented magnetization plot of the  $\text{Fe}_3\text{O}_4@$ His@Cu magnetic hybrid. The sample did not show remanence at 300 K and the saturation magnetization was around 35.2 emu/g which was smaller value compared to that of bulk magnetite, known as 92 emu/g [53]. The reason for this is originated from the canted spins on the surface of  $\text{Fe}_3\text{O}_4$  due to the weakened exchange interactions between surface and core spins [54, 55]. As we know, when the particle size decreases, surface to volume ratio increases. Eventually, it causes to determine the characteristic of the whole particle. In other words, because of the functional groups or molecules on the surface of magnetite, a reduced magnetization is seen. Thus, reduced magnetization, absence of coercivity and remanence are the key features of superparamagnetic particles. The above results clearly show that  $\text{Fe}_3\text{O}_4@$ His@Cu has a superparamagnetic character.

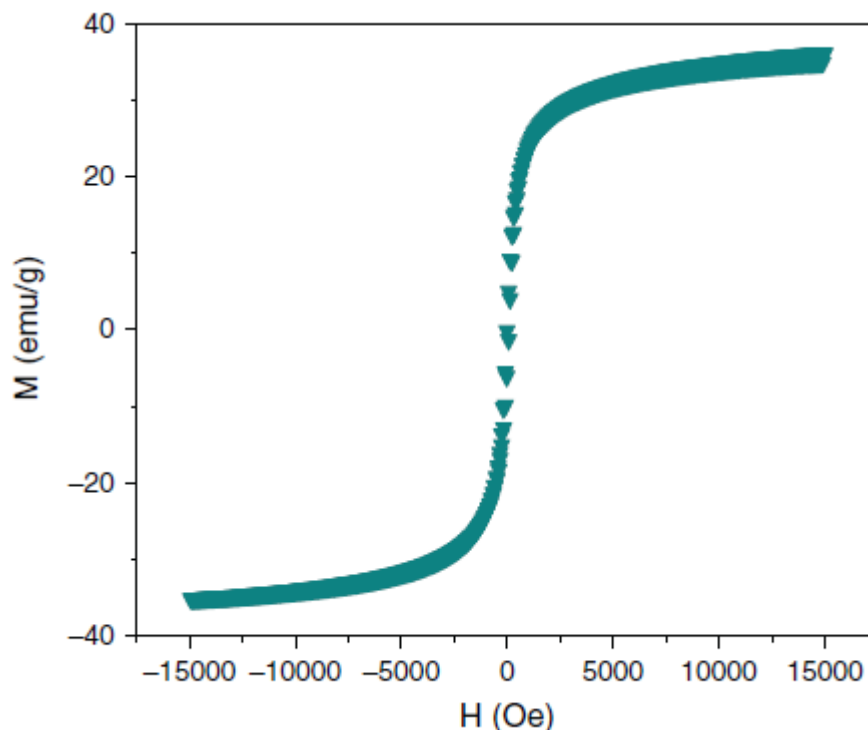


**Figure 3.6:** Magnetic hysteresis curve of  $\text{Fe}_3\text{O}_4@$ His-Cu magnetic hybrid.

### 3.1.3. Characterization Results of $\text{Fe}_3\text{O}_4@$ His-Ag Magnetic Hybrid

The XRD powder pattern of  $\text{Fe}_3\text{O}_4@$ His-Ag magnetic composite was represented in Fig. 3.7(I). The main peaks matched as the Ag (JCPDS No. 87-0721) and  $\text{Fe}_3\text{O}_4$  nanocrystals (JCPDS No. 75-002). Three remarkable peaks appear at  $2\theta=38.18^\circ$ ,  $44.38^\circ$  and  $64.48^\circ$  which correspond respectively to (1 1 1), (2 0 0) and (2 2 0) lattice planes meaning the fabrication of AgNPs on the surface of  $\text{Fe}_3\text{O}_4@$ His. The mean crystallite size of the product was obtained as 9 nm [51].

To predict the weight percentage value of the samples, thermogravimetric analysis was carried out. The TGA results of bulk  $\text{Fe}_3\text{O}_4$ ,  $\text{Fe}_3\text{O}_4@$ His-Ag magnetic nanocomposite and His were shown in Fig 3.7(II), respectively. It was seen that there was a resistance for  $\text{Fe}_3\text{O}_4$  up to  $700^\circ\text{C}$  according to the Fig 3.7(II)a. Decomposition temperatures obtained from thermograms of  $\text{Fe}_3\text{O}_4$  and  $\text{Fe}_3\text{O}_4@$ His-Ag displayed two step weight loss (Fig. 3.7(II)b and c).  $\text{Fe}_3\text{O}_4@$ His-Ag had a mild weight loss up to  $150^\circ\text{C}$  because of the moisture adsorption as His showed a remarkable thermal resistance up to  $300^\circ\text{C}$ . Decomposition of His on the surface of

$\text{Fe}_3\text{O}_4$  occurred faster at lower temperatures, this was an indication of catalyst effect of  $\text{Fe}_3\text{O}_4$  and the final weight loss was about 14 % for  $\text{Fe}_3\text{O}_4$ @His-Ag [56].

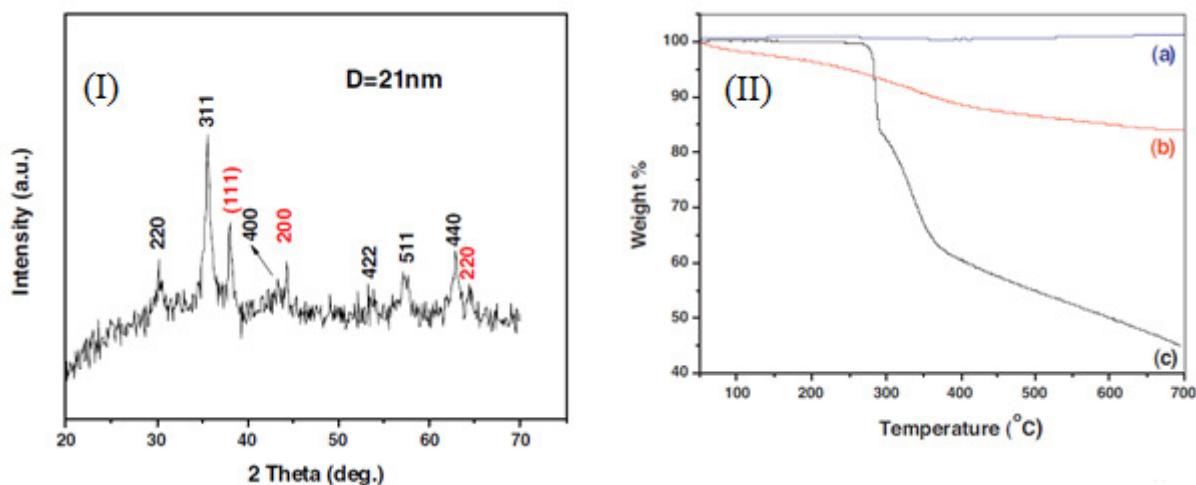


**Figure 3.7:**(I) XRD powder pattern of  $\text{Fe}_3\text{O}_4$ @His-Ag and (II) TG thermograms of (a) bare  $\text{Fe}_3\text{O}_4$ , (b)  $\text{Fe}_3\text{O}_4$ @His-Ag and (c) Histidine [82].

Figure 3.8(I) showed FTIR spectra all materials including  $\text{Fe}_3\text{O}_4$ @His-Ag, His and  $\text{Fe}_3\text{O}_4$ @His. For pure His (Fig 3.8(I)b), the presence of  $\text{NH}_2$  stretching vibrations was found at  $\sim 3330\text{ cm}^{-1}$  and symmetric and asymmetric carboxylate ( $\text{COO}^-$ ) stretching modes were seen at  $1411$  and  $1635\text{ cm}^{-1}$ , respectively. The signal at  $\sim 570\text{--}590\text{ cm}^{-1}$  was assigned to the M-O stretching mode (Fig 3.8(I)a and c). Based on them, we have seen that there was a chemisorption between His and  $\text{Fe}_3\text{O}_4$ . In addition, the typical band of C=N vibration at  $1630\text{ cm}^{-1}$  for His was observed at  $1640\text{ cm}^{-1}$  for  $\text{Fe}_3\text{O}_4$ @His-Ag (Fig. 3.8a and b). This shifting occurred if silver nanoparticles interact with functional group of His, confirming the encapsulation of Ag NPs on the product. Hence all these results indicate that  $\text{Fe}_3\text{O}_4$ @His-Ag formed successfully.

Magnetic hysteresis curve of the  $\text{Fe}_3\text{O}_4$ @His-Ag nanocomposite was displayed in Fig. 3.8(II) which is a typical curve for a superparamagnetic material. Its magnetization curve was taken at room temperature and can be found that it exhibited a well superparamagnetic property. Also, the coercivity was low and the saturation magnetization value as  $\sim 40\text{ emu/g}$ .

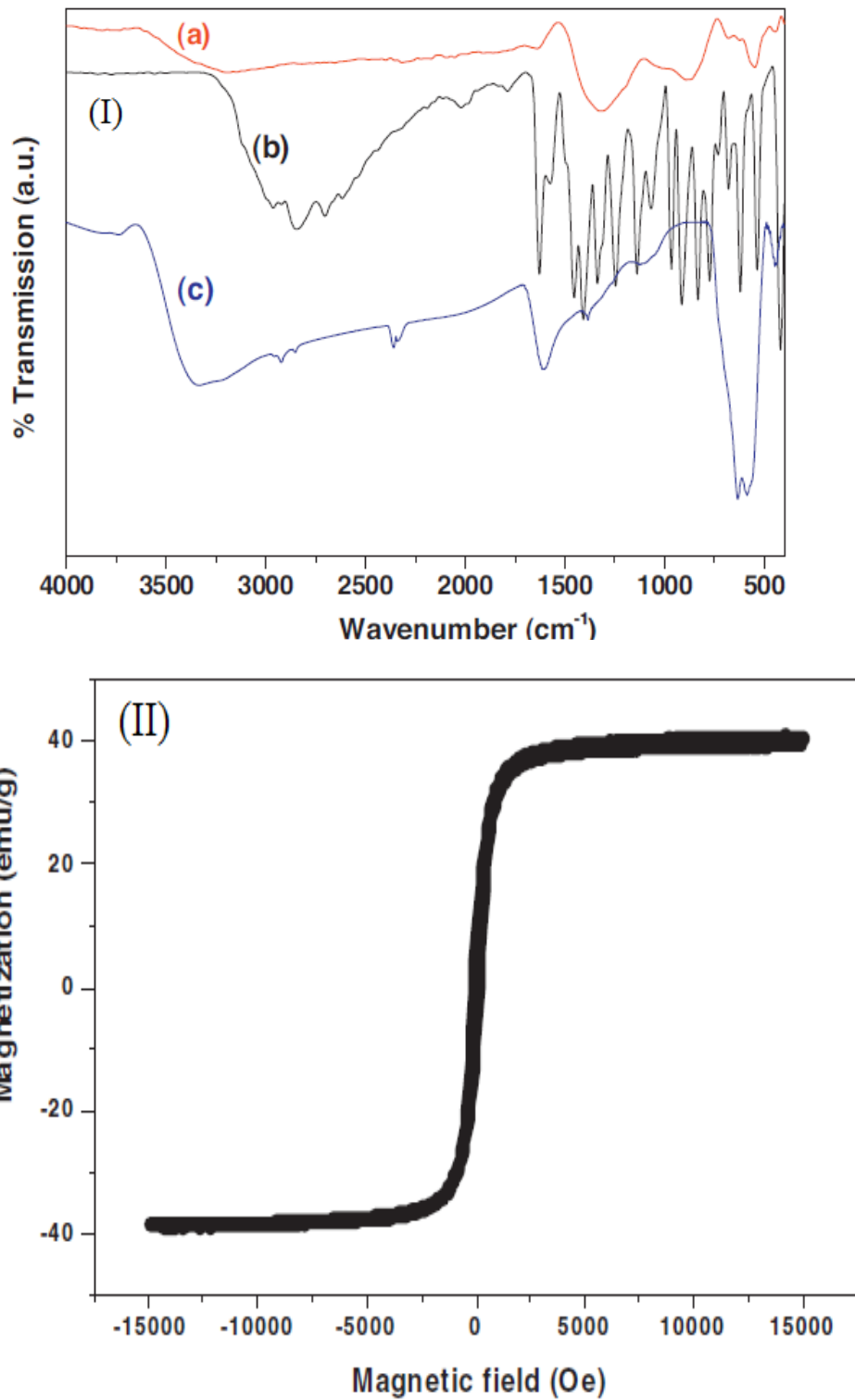
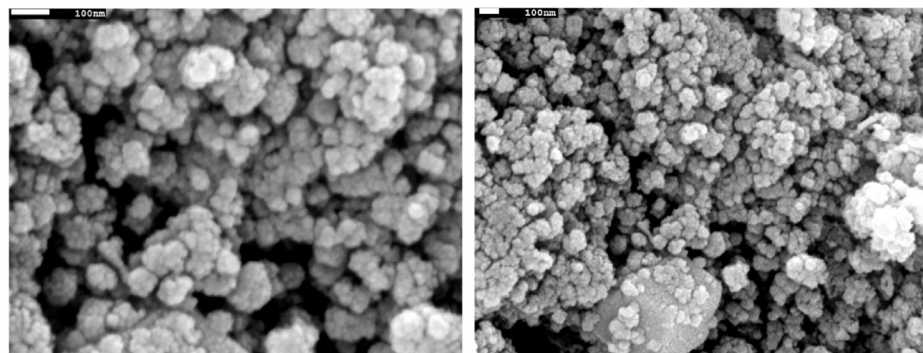


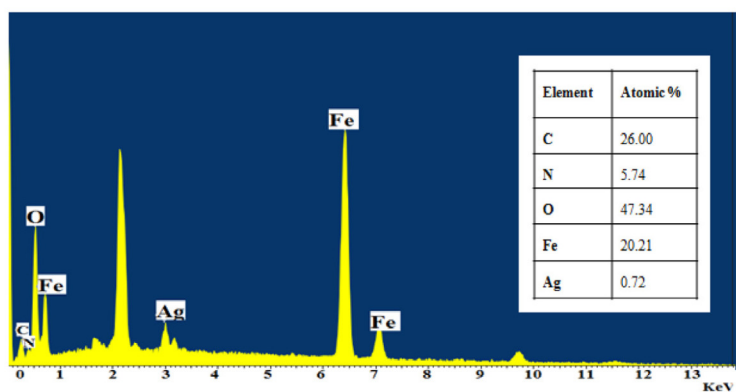
**Figure 3.8:** (I) FTIR spectra of (a)  $\text{Fe}_3\text{O}_4$ @His-Ag, (b) His and (c)  $\text{Fe}_3\text{O}_4$ @His and (II) magnetization plot of  $\text{Fe}_3\text{O}_4$ @His-Ag magnetic hybrid [82].



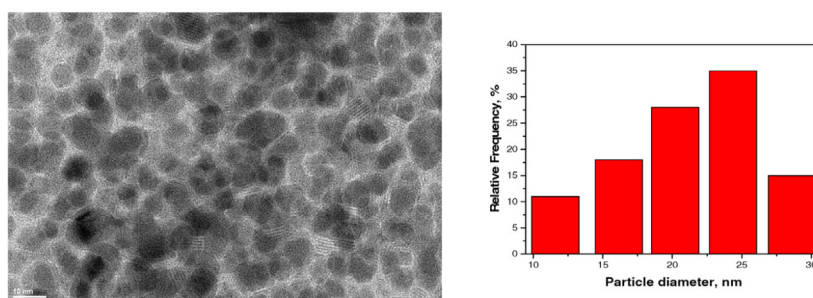
The SEM images with EDX results and TEM micrographs of the product were illustrated in Fig 3.9a-c, respectively. Agglomerations were seen to a certain degree and the mean particle size was estimated to be almost as 24 and 25 nm from SEM and TEM, respectively (Fig 3.9a and 3.9c). All metals were present in the sample according to the EDX result (Fig. 3.9b).



(a)



(b)

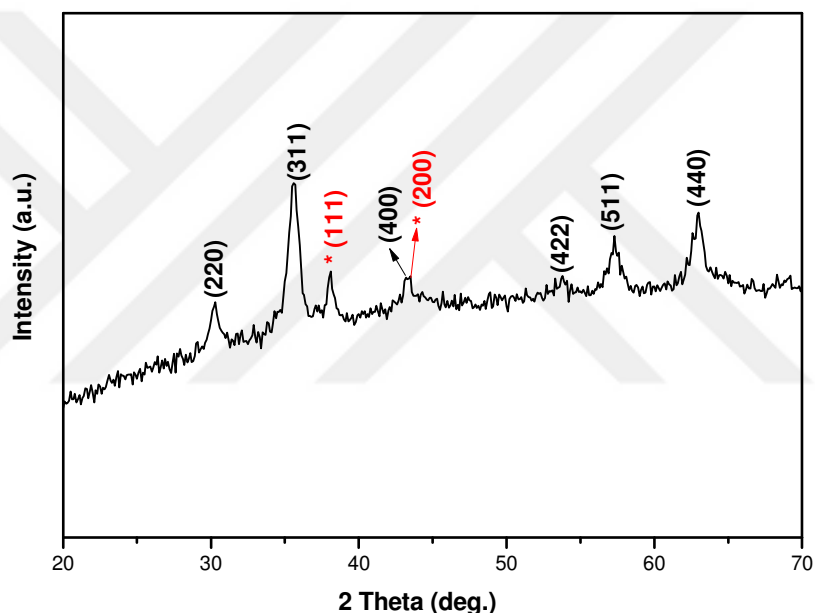


(c)

**Figure 3.9:** (a) The SEM images, (b) EDX and (c) TEM image with the particle size distribution diagram of  $\text{Fe}_3\text{O}_4@$ His-Ag magnetic hybrid.

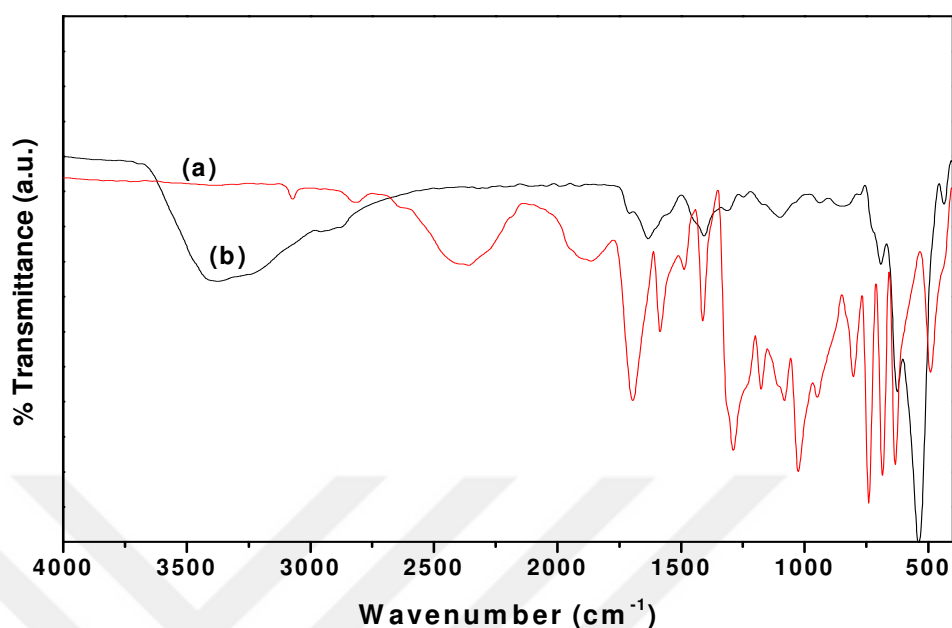
### 3.1.4. Characterization Results of Fe<sub>3</sub>O<sub>4</sub> @Nico-Ag Magnetic Hybrid

The diffraction pattern of prepared magnetic hybrid was presented in Fig. 3.10. The reflections at (220), (311), (400), (422), (511), (440) and (111) and (200) can be attributed to the Fe<sub>3</sub>O<sub>4</sub> (JCPDS No. 75-0033) and Ag (JCPDS No. 87-0720, labeled with\*), respectively. No crystalline impurities were seen suggesting the good crystalline quality of the sample. In order to estimate the average crystallite size for Fe<sub>3</sub>O<sub>4</sub>@Nico-Ag, the Scherrer equation was used with the peak width of the (311) reflection and found to be as 10 nm [57].



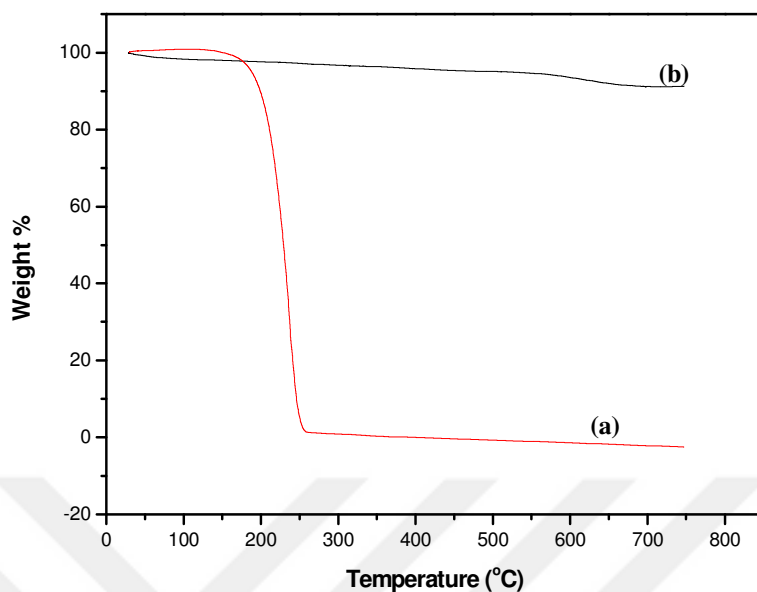
**Figure 3.10:** XRD powder pattern of Fe<sub>3</sub>O<sub>4</sub>@Nico-Ag magnetic hybrid.

FTIR spectra of the products were shown in Fig 3.11. For pure Nico (Fig. 3.11a), the presence of C=O, C-O and C-N stretching vibrations were found at 1700, 1300 and 1326 cm<sup>-1</sup>, respectively. The typical carbonyl stretching signal shifted to 1630 cm<sup>-1</sup> with binding process of the Fe<sub>3</sub>O<sub>4</sub> since carbonyl group was involved in binding process (Fig. 3.11b). Also, typical band of C-N at 1320 cm<sup>-1</sup> changed to 1340 cm<sup>-1</sup> due to the coordination of pyridine in Nicotinic acid and Ag NPs [51, 58, 59].



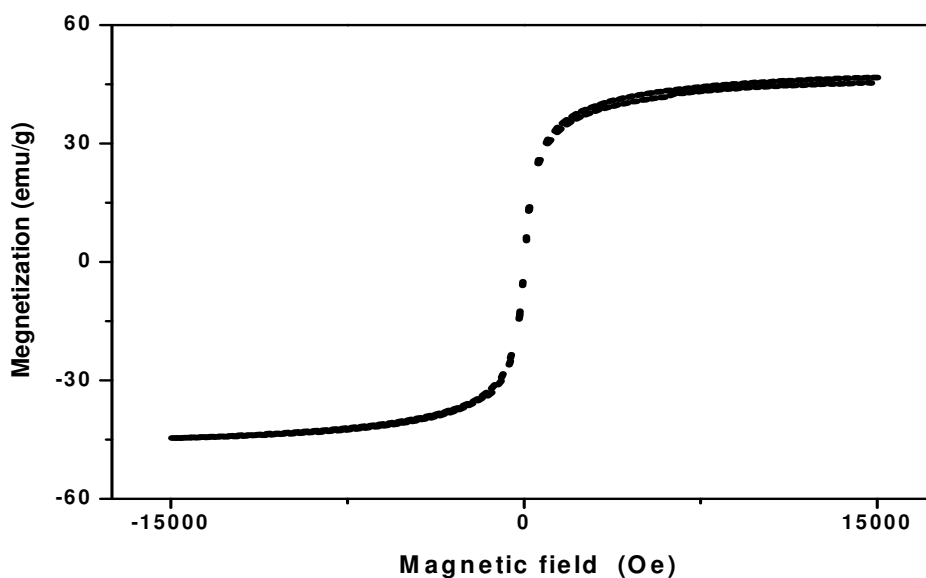
**Figure 3.11:** FTIR spectra of (a) Nicotinic acid and (b) Fe<sub>3</sub>O<sub>4</sub>@Nico-Ag magnetic hybrid.

Fig 3.12 presented thermal curves of pure nico and the prepared magnetic nanocatalyst, Fe<sub>3</sub>O<sub>4</sub>@Nico-Ag. In Fig 3.12a, it was noted that the weight loss was between 180 and 271°C, which was ascribed to the removal of H<sub>2</sub>O and decomposition of organic layer. The observation of Fig. 3.12b illustrated that there were two stages of weight loss. The first weight loss occurred in temperature around 80°C owing to the hydration and there was almost no weight loss up to 300°C. The second weight loss above 300 °C must be associated with the thermal decomposition of organic parts. Consequently, it was clear that Fe<sub>3</sub>O<sub>4</sub>@Nico-Ag consisted of 10 % organic part.



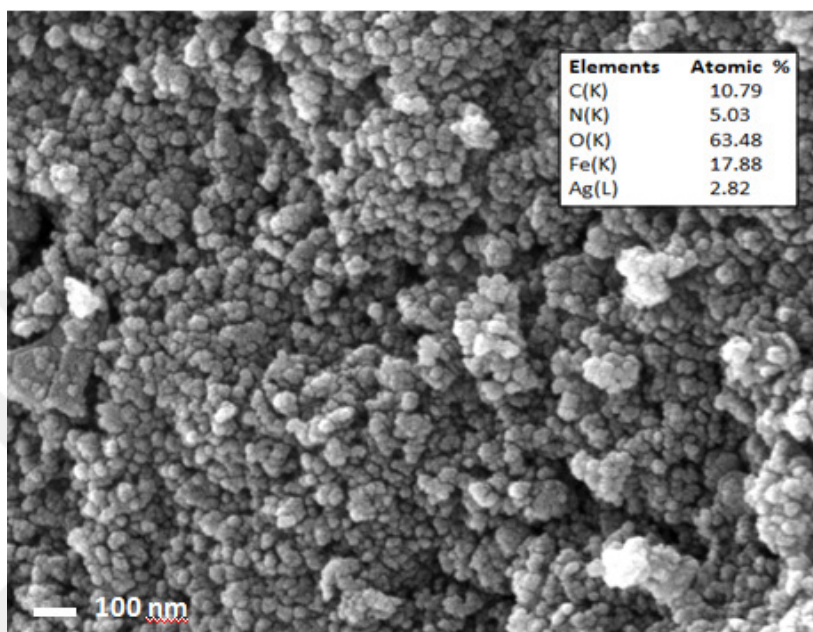
**Figure 3.12:** TG plot of (a) Nicotinic acid and (b)  $\text{Fe}_3\text{O}_4$ @Nico-Ag magnetic hybrid.

Fig. 3.13 showed the degree of magnetization of  $\text{Fe}_3\text{O}_4$ @Nico-Ag magnetic hybrid and its saturation magnetization was around 52.4 emu/g. In addition, since the sample does not have remanance or coercivity at 300 K and it could be thought to have superparamagnetic character.



**Figure 3.13:** Magnetic hysteresis curve of  $\text{Fe}_3\text{O}_4$ @Nico-Ag magnetic hybrid.

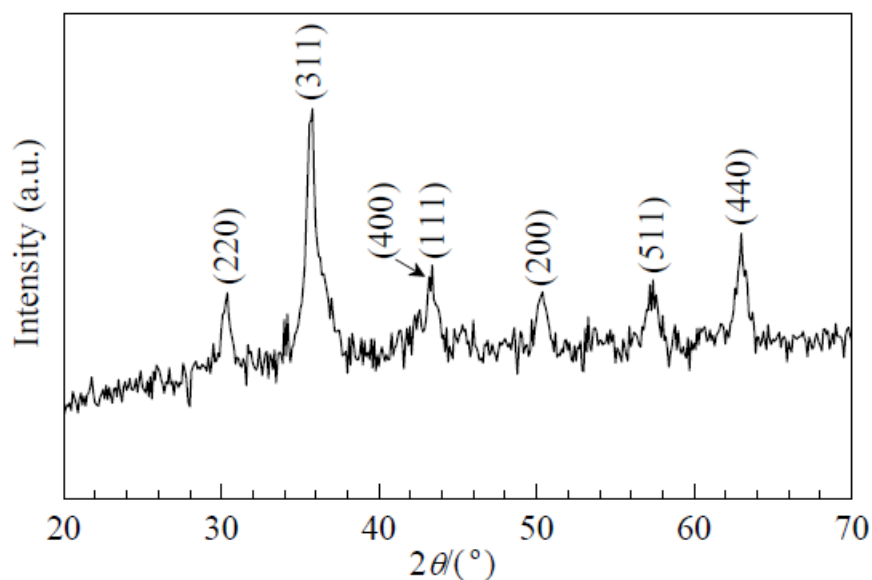
To estimate the elements in the synthesized material, the  $\text{Fe}_3\text{O}_4@\text{Nico-Ag}$ , both SEM and EDX analysis were performed. Accordingly,  $\text{Fe}_3\text{O}_4$  nanoparticles had nearly spherical shapes and agglomerated resulting to form almost 20-50 nm particles (Fig. 3.14).



**Figure 3.14:** SEM image of  $\text{Fe}_3\text{O}_4@\text{Nico-Ag}$  magnetic hybrid.

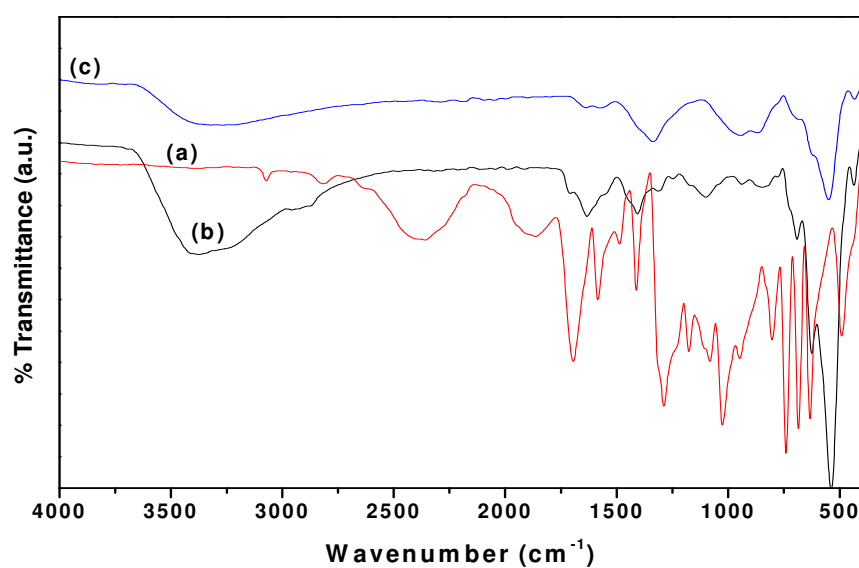
### 3.1.5. Characterization Results of $\text{Fe}_3\text{O}_4@\text{Nico-Cu}$ Magnetic Hybrid

Diffraction pattern of  $\text{Fe}_3\text{O}_4@\text{Nico-Cu}$  magnetic hybrid was shown in Fig 3.15. Two inorganic phases are  $\text{Fe}_3\text{O}_4$  ((220), (311), (400), (422), (511), (440)) (ICDD card no: 19-0629) and Cu NPs ((111), (200)) [20] (ICDD card no: 85- 1326) with the given hkl values, respectively.



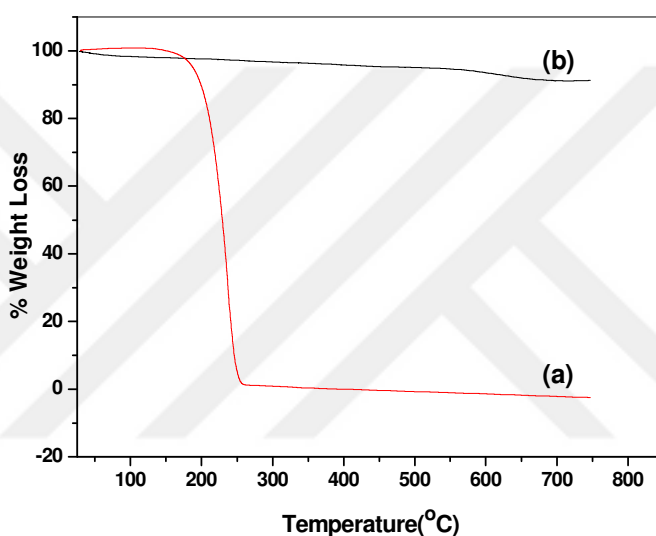
**Figure 3.15:** XRD powder pattern of  $\text{Fe}_3\text{O}_4@\text{Nico-Ag}$  magnetic hybrid.

Fig. 3.16 represented the FTIR spectra of nicotinic acid which has the stretchings;  $\nu_{(\text{C}=\text{O})} = 1670 \text{ cm}^{-1}$ ,  $\nu_{(\text{C}-\text{O})} = 1280 \text{ cm}^{-1}$ ,  $\nu_{(\text{C}-\text{N})} = 1325 \text{ cm}^{-1}$  [21] (Fig. 3.16a). In addition, carbonyl group of organic part was used for the connection to the  $\text{Fe}_3\text{O}_4$  nanoparticles. The typical nicotinic acid is C-N stretching ( $\nu = 1,321 \text{ cm}^{-1}$ ) owing to the pyridine.



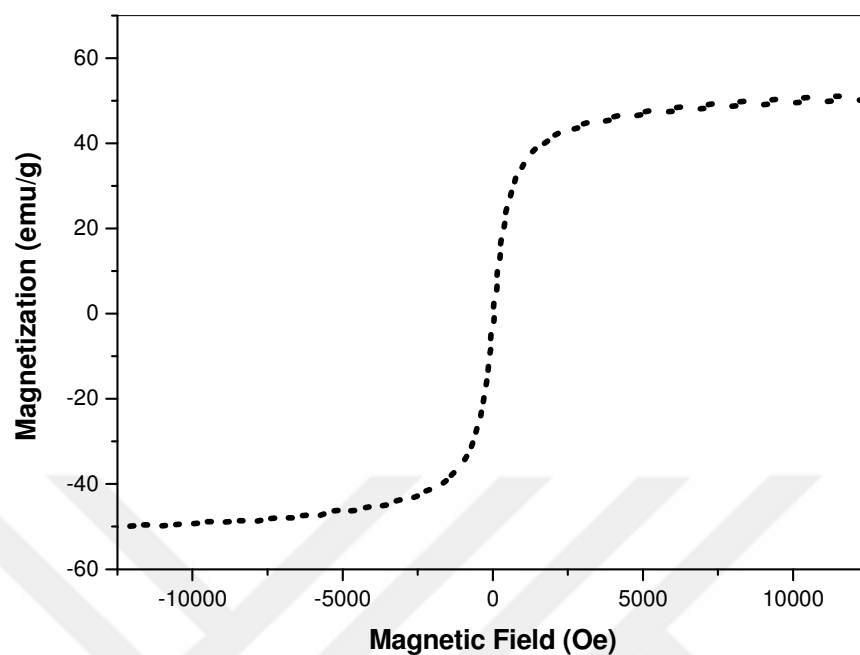
**Figure 3.16:** FTIR spectra of (a) Nico, (b)  $\text{Fe}_3\text{O}_4@\text{Nico}$  and (c)  $\text{Fe}_3\text{O}_4@\text{Nico-Cu}$  samples.

Nicotinic acid had almost single step decomposition including the evaporation of physisorbed water and the degradation of the organic layer up to 270 °C. The complete degradation of nicotinic acid itself happened at higher temperatures (Fig. 3.17a). Fig. 3.17b showed the degradation behaviour of the product which has two step of degradations. The first degradation was continued up to 500 °C which was due to degradation of functional groups. Up to 700 °C, the second decomposition was observed, this degradation was due to organic back bone.



**Figure 3.17:** TG thermogram of (a) Nicotinic acid and (b) Fe<sub>3</sub>O<sub>4</sub>@Nico-Cu magnetic hybrid.

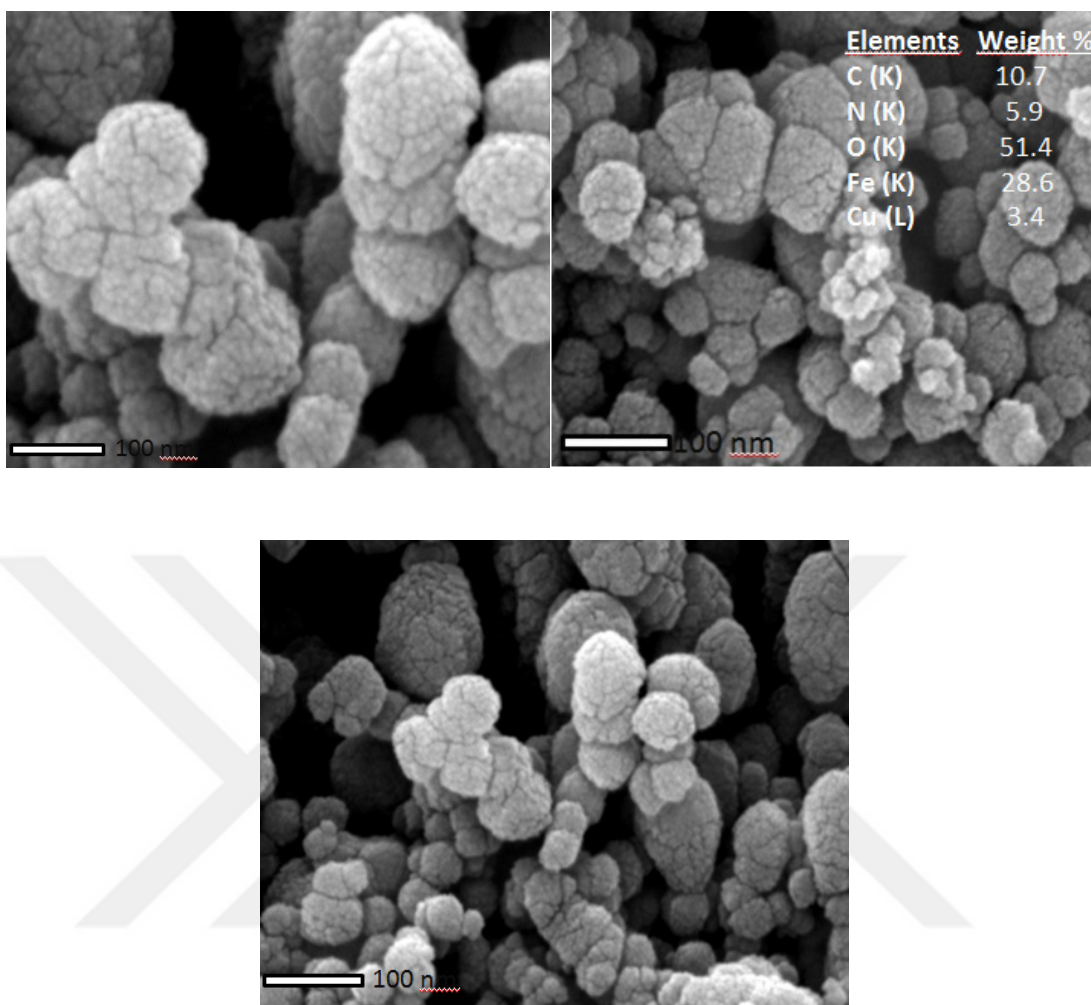
Figure 3.18 showed the magnetization slope of Fe<sub>3</sub>O<sub>4</sub>@Nico-Cu magnetic nanocomposite. The coercivity was not observed at 300 K which indicated that Fe<sub>3</sub>O<sub>4</sub>@Nico-Cu sample had superparamagnetic character and the saturation magnetization was around as 50 emu/g.



**Figure 3.18:** Magnetic hysteresis curve of Fe<sub>3</sub>O<sub>4</sub>@Nico-Cu magnetic hybrid.

The morphological characteristics of the nicotinic acid stabilized magnetic nanoparticles were analyzed and were presented in Fig. 3.19. The pictures revealed that the synthesized material have the homogeneous structure with spherical shapes. In addition, EDAX analysis confirmed the presence of metallic species accurately.

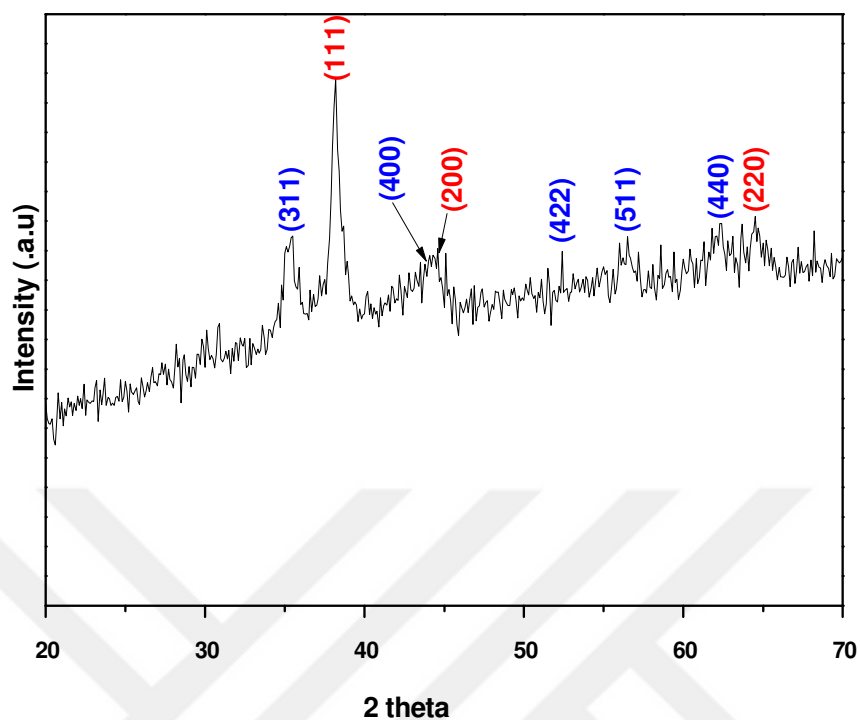




**Figure 3.19:** SEM micrographs of  $\text{Fe}_3\text{O}_4$ @Nico-Cu magnetic hybrid.

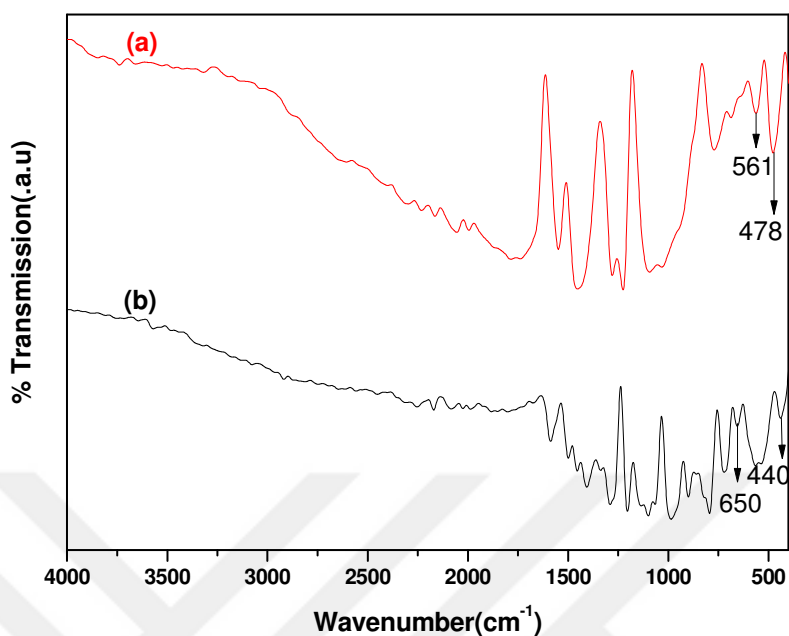
### 3.1.6. Characterization Results of $\text{MnFe}_2\text{O}_4$ @PANI-Ag Magnetic Hybrid

The crystallinity and the diffraction peaks of the as prepared  $\text{MnFe}_2\text{O}_4$ @PANI-Ag hybrid material was presented in Fig. 3.20. According to the JCPDS reference (73-1964) and (99-200-4306), the miller indices of (220), (311), (400), (511), (440) and (110), (200), (220) demonstrated that  $\text{MnFe}_2\text{O}_4$  and Ag NPs are present, respectively. Also, sharper and more intense peaks are observed for AgNPs in the product indicating that it has a better crystallinity than  $\text{MnFe}_2\text{O}_4$ . The crystal size determined by the (311) and (111) peak based on Debye-Scherrer equation from XRD is 12.80 and 20.32 nm for  $\text{MnFe}_2\text{O}_4$  and Ag NPs, respectively.



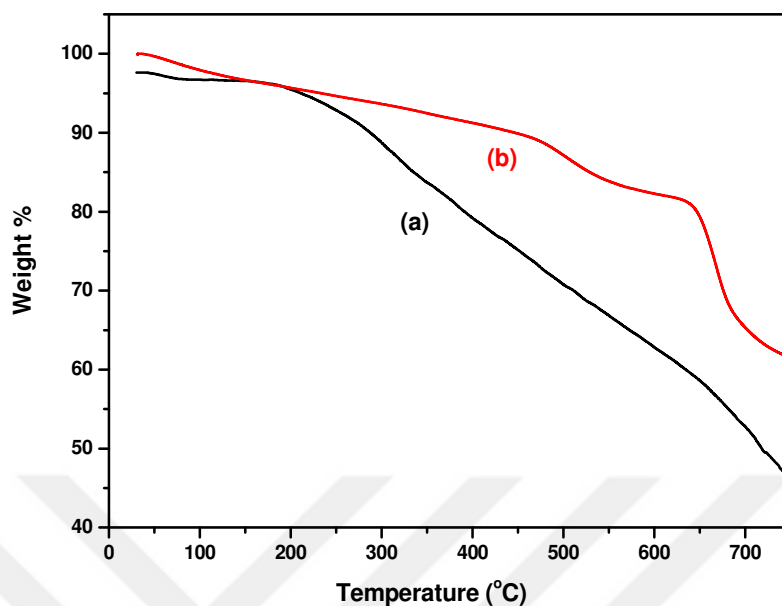
**Figure 3.20:** XRD pattern of the MnFe<sub>2</sub>O<sub>4</sub>@PANI-Ag magnetic hybrid.

To understand the formation of polyaniline on the surface of MnFe<sub>2</sub>O<sub>4</sub> magnetic core, we conducted FTIR spectroscopy. Fig. 3.21 presented the spectra of PANI coated MnFe<sub>2</sub>O<sub>4</sub> and MnFe<sub>2</sub>O<sub>4</sub>@PANI-Ag magnetic hybrids. Strong stretchings at almost 400 and 650 cm<sup>-1</sup> were for the metal-oxygen vibrations for both spectrum (Fig 3.21a and 3.21b). T<sub>d</sub> absorption peaks were seen at a lower frequency compared to the O<sub>h</sub> absorption bands since metal-oxygen bond length in T<sub>d</sub> is shorter than O<sub>h</sub>. In addition to metal-oxygen stretching vibrations, all the characteristic bands of aniline were present in both spectrum. The intensities at 1546 and 1447 cm<sup>-1</sup> could be ascribed to the C–C stretching. Also, it contained the bands at 1102 (δ<sub>CH</sub>(in-plane)) and 777 cm<sup>-1</sup> (δ<sub>CH</sub>(out-of-plane)) due to the benzene. On the basis of these results, we could say that the polymerization was successful for coating process.



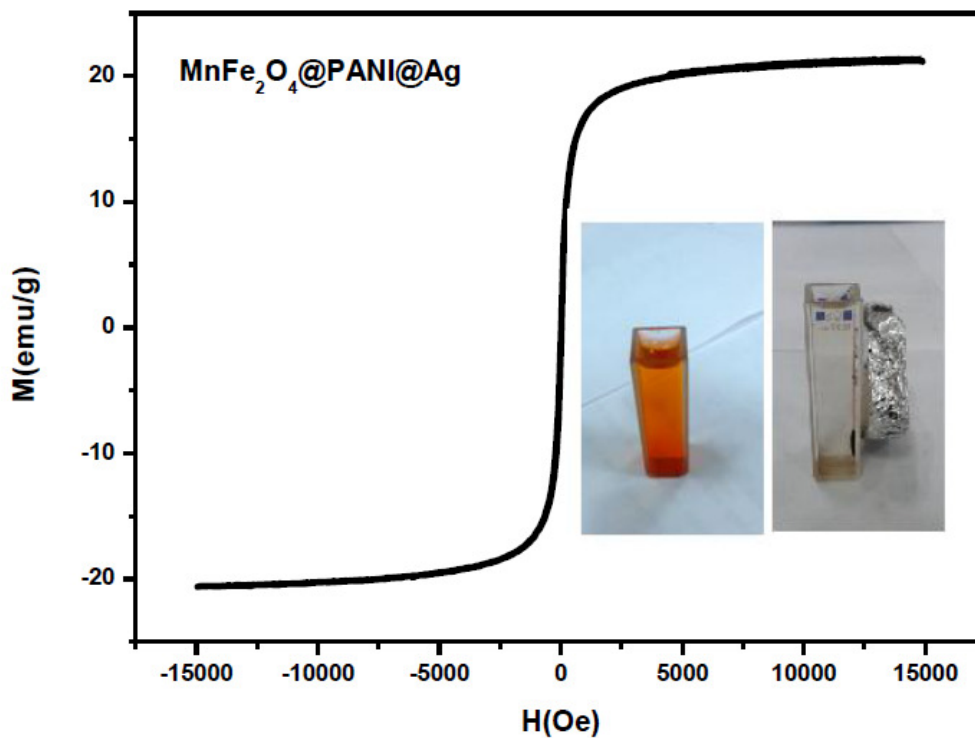
**Figure 3.21:** FTIR spectra (a) MnFe<sub>2</sub>O<sub>4</sub>@PANI and (b) MnFe<sub>2</sub>O<sub>4</sub>@PANI-Ag magnetic hybrid.

Thermograms of only polymer and polymer coated magnetic material was shown in Fig. 3.22. According to the several research work before, PANI showed three step weight loss behavior. Similar decomposition of PANI was seen in Fig 3.22a. When it comes to the Fig 3.22b, MnFe<sub>2</sub>O<sub>4</sub>@PANI-Ag magnetic hybrid had a similar degradation with PANI but it had lower weight loss because of the higher interaction between PANI and MnFe<sub>2</sub>O<sub>4</sub>. As a result, this thermal result demonstrated that MnFe<sub>2</sub>O<sub>4</sub>@PANI@Ag magnetic nanocomposite consisted of almost 40 % as organic residue[60].



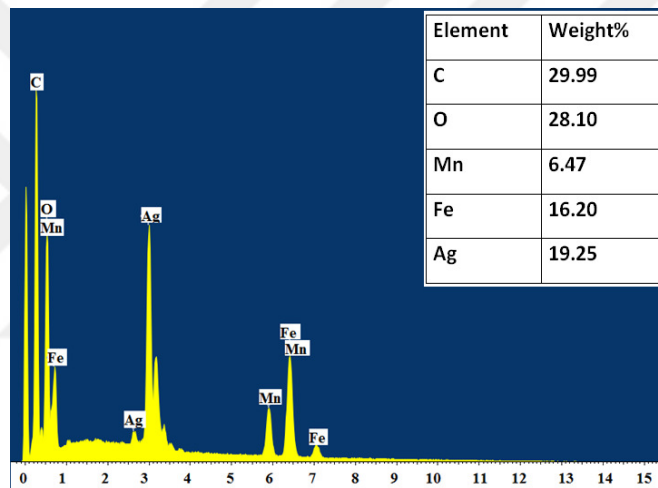
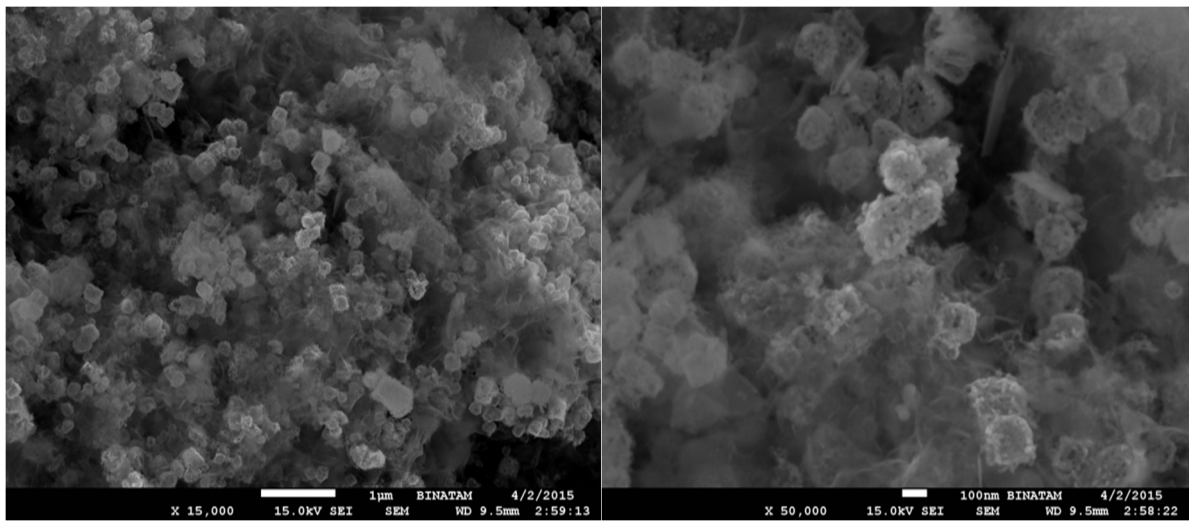
**Figure 3.22:** TG curves of (a) PANI and (b) MnFe<sub>2</sub>O<sub>4</sub>@PANI-Ag samples.

The specific M-H slope of the prepared MnFe<sub>2</sub>O<sub>4</sub>@PANI-Ag magnetic nanocomposite obtained from room temperature VSM measurement was represented in Fig. 3.23. Fig. 3.23 is a typical graph for a superparamagnetic material without the coercivity. This helps to recover of the MnFe<sub>2</sub>O<sub>4</sub>@PANI-Ag magnetic hybrid easily with a magnet. The saturation magnetization value was as 22 emu/g and inset in Fig. 3.23 showed the effect of the magnetic nanocatalyst as color change in the reaction.



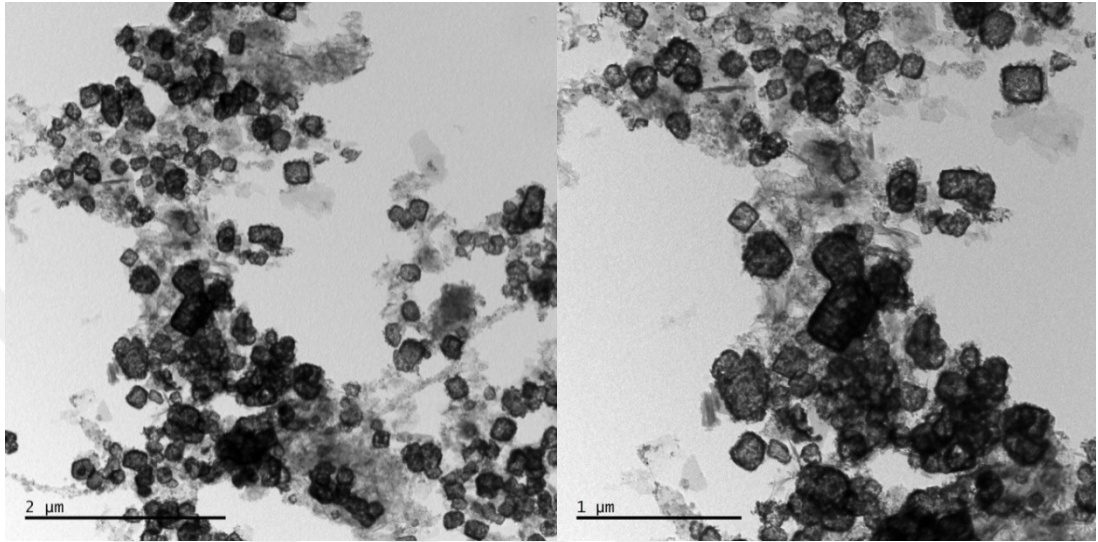
**Figure 3.23:** Magnetic hysteresis curve of  $\text{MnFe}_2\text{O}_4@\text{PANI}-\text{Ag}$  magnetic hybrid.

The SEM images of  $\text{MnFe}_2\text{O}_4@\text{PANI}-\text{Ag}$  magnetic nanocomposite taken at low and high magnification were illustrated in Fig. 3.24a. Nanocomposites were randomly oriented forming irregular spherical microcrystals. The EDX image as shown in Fig 3.24 demonstrated the presence of metallic species in  $\text{MnFe}_2\text{O}_4@\text{PANI}-\text{Ag}$  magnetic nanocomposite confirming that the product was successfully fabricated.



**Figure 3.24:** (a) SEM images and (b) EDX spectra of MnFe<sub>2</sub>O<sub>4</sub>@PANI-Ag sample.

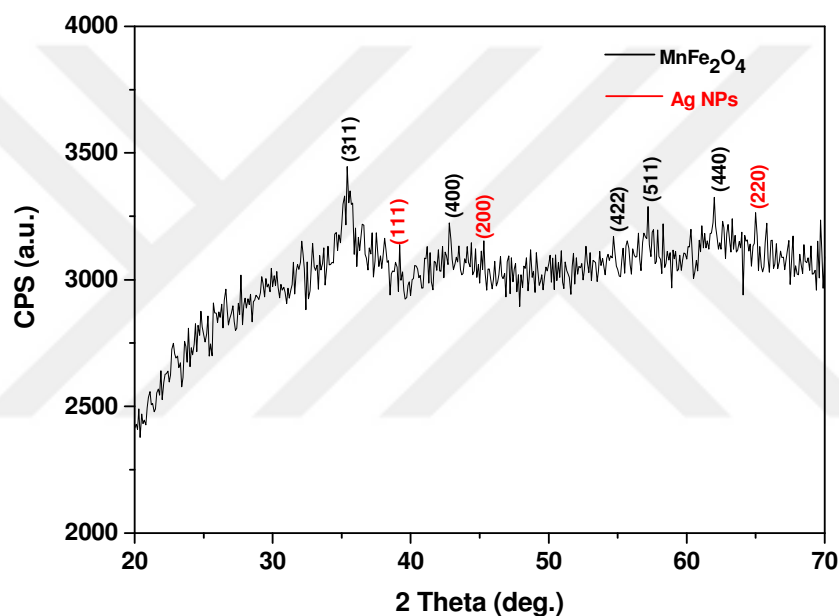
The micrographs of the  $\text{MnFe}_2\text{O}_4@\text{PANI-Ag}$  were further investigated by transmission electron microscopy in Fig. 3.25. The black core was the  $\text{MnFe}_2\text{O}_4$  NPs and light one was considered to be PANI in the matrix. Therefore, it can be concluded from the TEM images that magnetic nanoparticles were embedded to PANI matrix successfully.



**Figure 3.25:** TEM images for  $\text{MnFe}_2\text{O}_4@\text{PANI-Ag}$  magnetic hybrid.

### 3.1.7. Characterization Results of MnFe<sub>2</sub>O<sub>4</sub> @SiO<sub>2</sub>-Ag Magnetic Hybrid

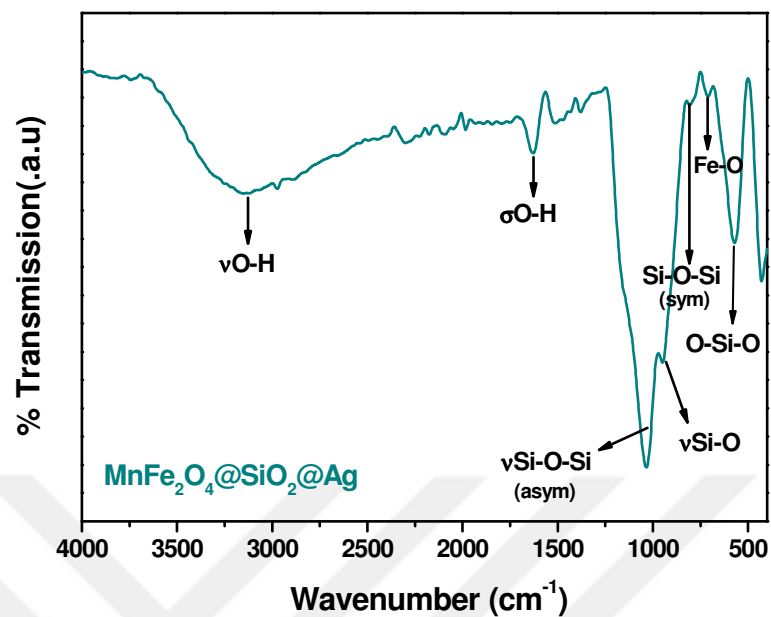
Figure 3.26 showed XRD pattern with the reflections of (311), (400), (422), (511) and (440). According to the JCPDS reference (73-1964), it corresponded to spinel structure of MnFe<sub>2</sub>O<sub>4</sub>. The mean crystallite size of MnFe<sub>2</sub>O<sub>4</sub>@SiO<sub>2</sub>-Ag was almost 10 nm. It was observed that there were three extra peaks with the (111), (2 0 0) and (2 2 0) indicating Ag NPs were also present (JCPDS No. 4-0783) and any other impurities were detected.



**Figure 3.26:** XRD powder pattern of MnFe<sub>2</sub>O<sub>4</sub>@SiO<sub>2</sub>-Ag magnetic hybrid.

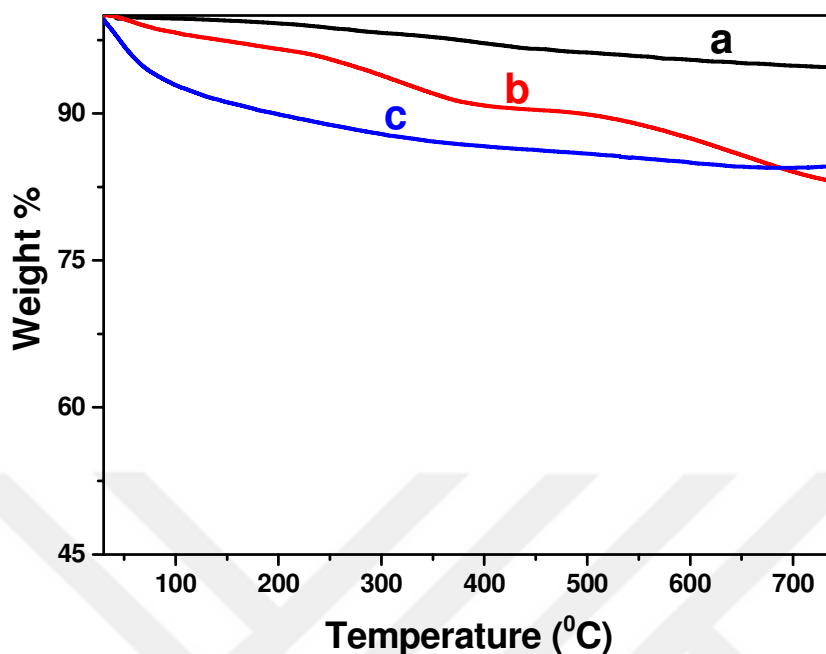
The FTIR spectrum for MnFe<sub>2</sub>O<sub>4</sub>@SiO<sub>2</sub>-Ag magnetic hybrid was shown in Fig. 3.27. The typical infrared frequencies at 570 and 430 cm<sup>-1</sup> which belong to the metal-oxygen stretching bonds were observed and the broad peak of O-H stretching vibration at 3450 cm<sup>-1</sup> was so clear. The stretching vibrations of asymmetric and symmetric silicon-oxygen-silicon bond at 1080 cm and 800 cm<sup>-1</sup> were due to the amorphous silica in the product[61].





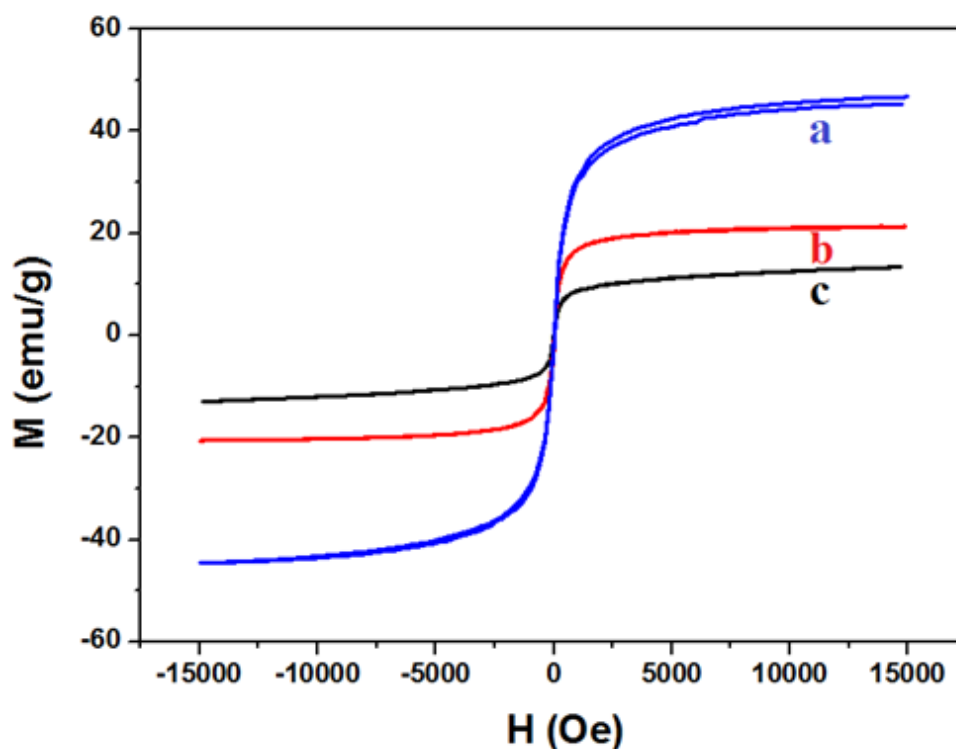
**Figure 3.27:** FTIR spectrum of  $\text{MnFe}_2\text{O}_4@SiO_2\text{-Ag}$  magnetic hybrid.

Thermographs of all materials were performed to investigate the interaction between  $\text{MnFe}_2\text{O}_4$  and  $\text{SiO}_2$ . No remarkable weight loss was seen for  $\text{MnFe}_2\text{O}_4$  (Fig. 3.28a). Magnetic nanocomposites had similar decomposition steps and the weight loss was about 15% for both of them and they probably were due to the residual water and  $\text{SiO}_2$  (Fig. 3.28b and 3c).



**Figure 3.28:** TG curves of (a) MnFe<sub>2</sub>O<sub>4</sub>, (b) SiO<sub>2</sub> coated MnFe<sub>2</sub>O<sub>4</sub> and (c) MnFe<sub>2</sub>O<sub>4</sub>@SiO<sub>2</sub>-Ag samples.

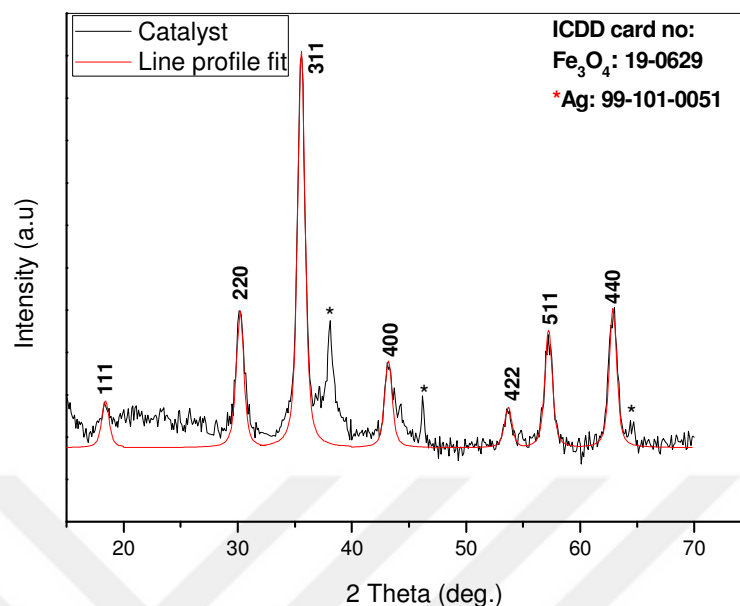
Magnetization curves of bulk MnFe<sub>2</sub>O<sub>4</sub>, SiO<sub>2</sub> coated MnFe<sub>2</sub>O<sub>4</sub> and MnFe<sub>2</sub>O<sub>4</sub>@SiO<sub>2</sub>-Ag magnetic nanocomposite, measured were shown in Fig. 3.29. The final product was superparamagnetic since there was no coercivity. The saturation magnetization was found to be as 50, 20 and 13.44 emu/g bulk MnFe<sub>2</sub>O<sub>4</sub>, SiO<sub>2</sub> coated MnFe<sub>2</sub>O<sub>4</sub> and MnFe<sub>2</sub>O<sub>4</sub>@SiO<sub>2</sub>-Ag magnetic nanocomposite, respectively. Owing to the diamagnetic layer, M<sub>s</sub> was found to be low compared to that of bulk sample (MnFe<sub>2</sub>O<sub>4</sub>).



**Figure 3.29:** Magnetic hysteresis plots of (a)  $\text{MnFe}_2\text{O}_4$ , (b)  $\text{SiO}_2$  coated  $\text{MnFe}_2\text{O}_4$  and (c)  $\text{MnFe}_2\text{O}_4@ \text{SiO}_2$ -Ag magnetic hybrids.

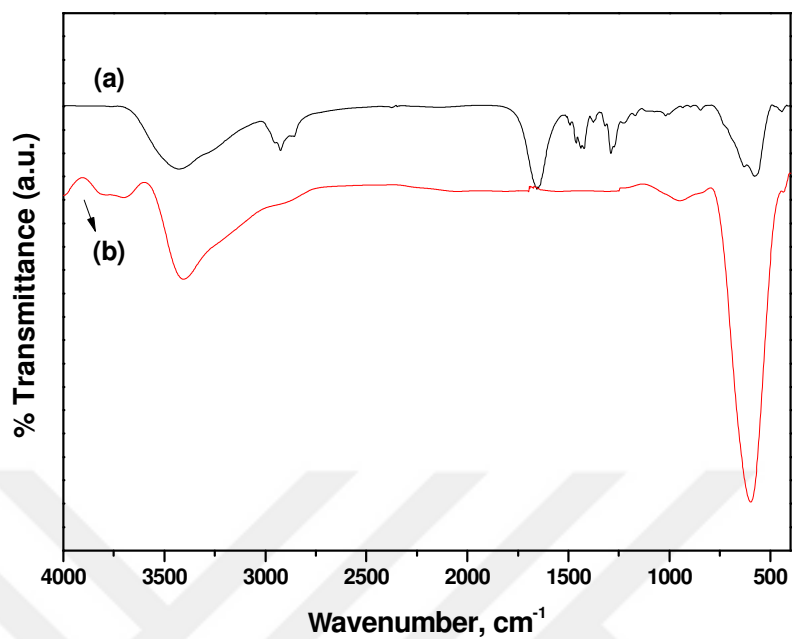
### 3.1.8. Characterization Results of $\text{Fe}_3\text{O}_4@ \text{PAMAM}(\text{G}1)$ -Ag Magnetic Hybrid

Fig. 3.30 showed the diffraction peaks of  $\text{Fe}_3\text{O}_4@ \text{PAMAM}(\text{G}1)$ -Ag. According to the JCPDS reference (19-0629), the diffraction peaks at  $2\theta=30^\circ, 35^\circ, 43^\circ, 53^\circ, 57^\circ,$  and  $62^\circ$  were observed for the cubic structure for  $\text{Fe}_3\text{O}_4$ . The additive peaks at  $2\theta=38.14^\circ, 46.30^\circ, 64.56^\circ$  were compatible for the Ag (JCPDS no. 99-101-0051). The mean crystallite size,  $D$ , was obtained 10 nm with line profile fitting.



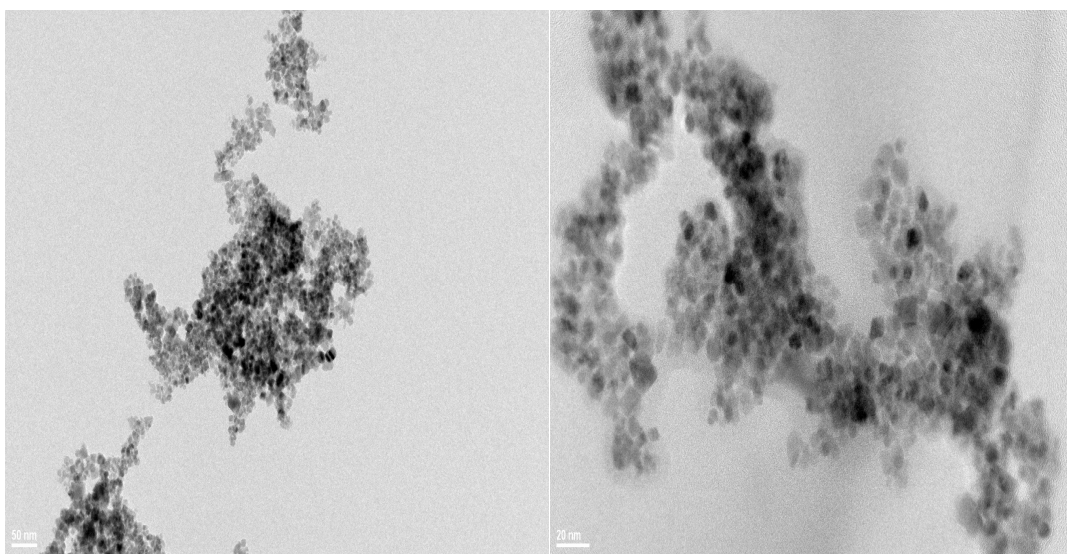
**Figure 3.30:** XRD powder pattern of  $\text{Fe}_3\text{O}_4$ @PAMAM(G1)-Ag magnetic hybrid.

One of the most characteristic vibration in infrared measurements for  $\text{Fe}_3\text{O}_4$  was the presence of metal-oxygen stretching and seen by the strong absorption peaks located around at 570-590  $\text{cm}^{-1}$  (Fig. 3.31). The broad signal at 3430  $\text{cm}^{-1}$  was related to the  $\text{NH}_2$  bending. The peak at 980  $\text{cm}^{-1}$  was usually ascribed to the Si-O-Fe bonds. The signals at 1135 and 1540  $\text{cm}^{-1}$  represented Si-O bonds, which confirm the interaction of APTES to the  $\text{Fe}_3\text{O}_4$  surface. Additionally, the signals at 2850 and 2925  $\text{cm}^{-1}$  clearly showed the existence of  $\text{CH}_2$  bonds. Thus, all these results confirmed that dendrimer and APTES were present on the surface  $\text{Fe}_3\text{O}_4$  NPs.



**Figure 3.31:** FTIR spectra of (a) Fe<sub>3</sub>O<sub>4</sub> and (b) Fe<sub>3</sub>O<sub>4</sub>@PAMAM(G1)-Ag samples.

TEM micrographs of Fe<sub>3</sub>O<sub>4</sub>@PAMAM(G1)-Ag magnetic hybrid material were represented in Fig 3.32 with the size distribution diagram. Particles had spherical morphology but they were aggregated because of the magnetic attraction each other[62]. A mean size,  $D$ , was almost 12 nm.



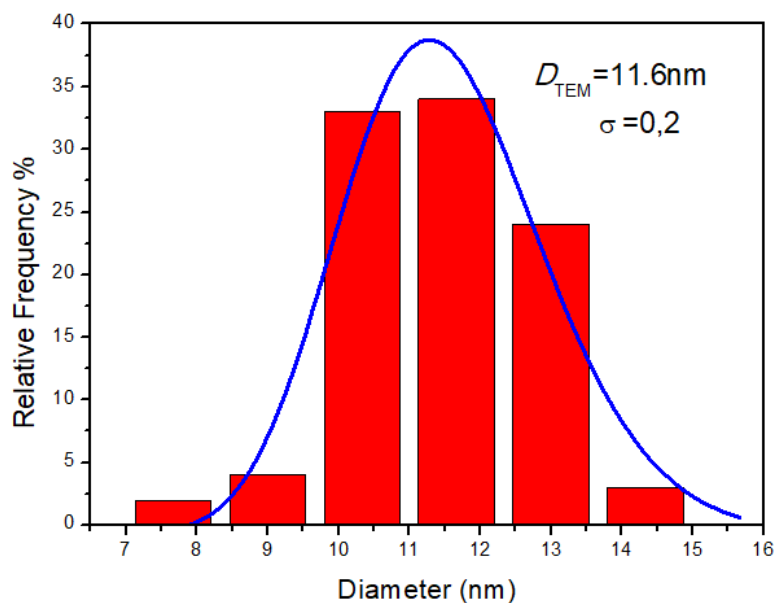


**Figure 3.32:** TEM images of  $\text{Fe}_3\text{O}_4$ @PAMAM(G1)-Ag nanocomposite different magnifications with particle size distribution diagram.

Spherical shapes with uniform size were seen from the Fig. 3.33. EDX demonstrated that metallic species were present in the composition of the product. This was the evidence of  $\text{SiO}_2$  and PAMAM are coated to the surface of  $\text{Fe}_3\text{O}_4$  NPs successfully.

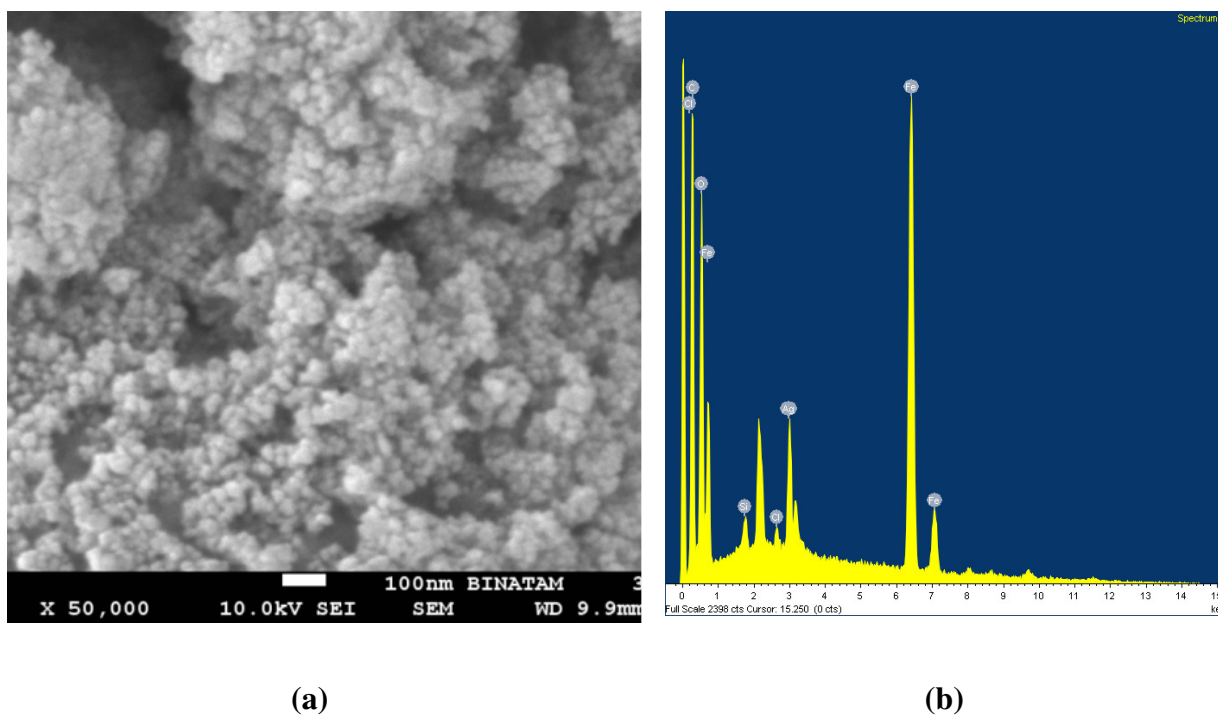


**Figure 3.33:** (a) The SEM image and (b) EDX of  $\text{Fe}_3\text{O}_4$ @PAMAM(G1)-Ag magnetic hybrid.

TGA plot of prepared material was seen in Fig. 3.34. As understood from the curve, weight loss started at  $\sim 100^{\circ}\text{C}$  by the removal of water and maintained up to  $700^{\circ}\text{C}$ . The total weight loss was 55 % which is related to the organic part since inorganic phases such as  $\text{Fe}_3\text{O}_4$  and Ag could be only at higher temperatures.

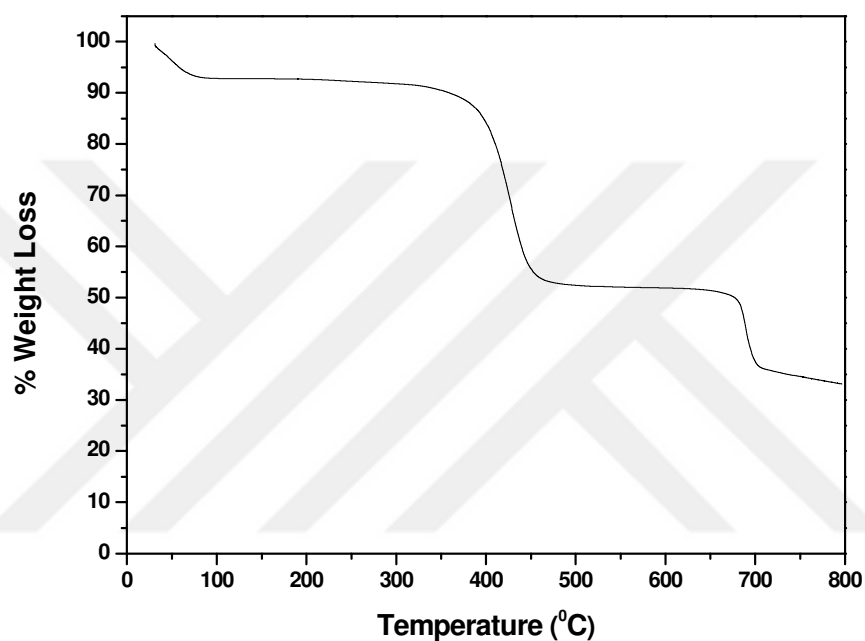


**Figure 3.33:** TG plot of the  $\text{Fe}_3\text{O}_4@PAMAM-Ag$  magnetic hybrid.

The magnetization curve was depicted in Fig. 3.34 and showed no coercivity. Besides, magnetization increased with applied magnetic field and did not saturate up to high field of 15 kOe. These are standard behaviors of superparamagnetic materials if the size is lower than 20 nm.

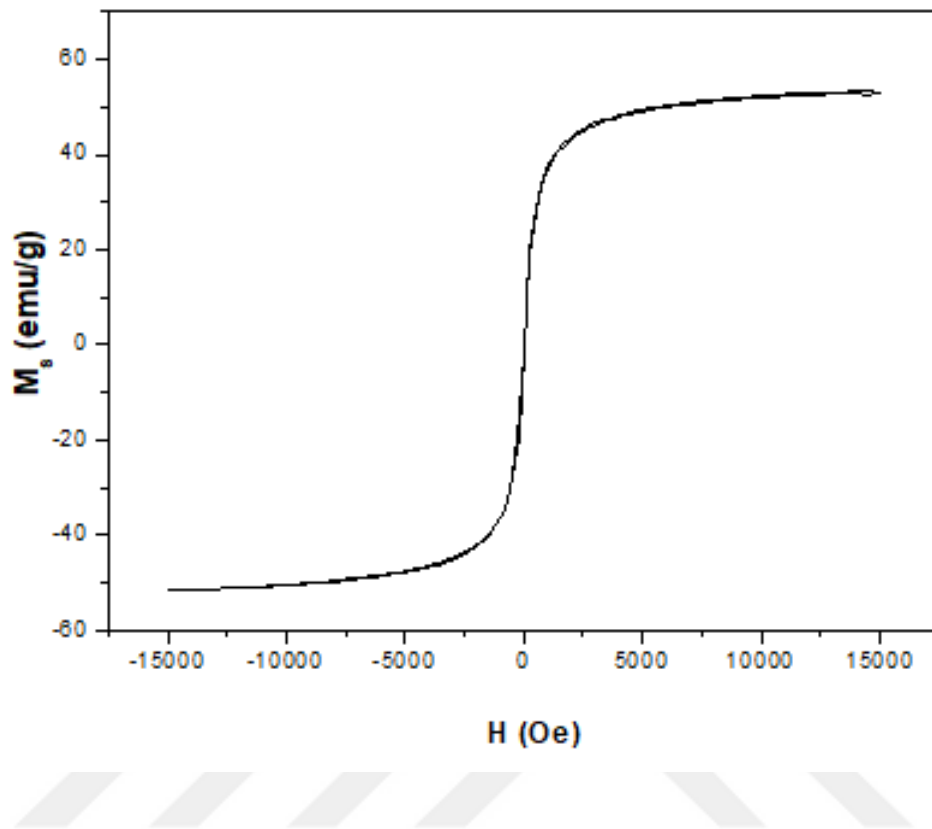


**Figure 3.34:** Magnetic hysteresis curve of Fe<sub>3</sub>O<sub>4</sub>@PAMAM-Ag magnetic hybrid.



## 4. DISCUSSION

### 4.1. EVALUATION OF UV-VIS RESULTS OF MAGNETIC NANOCATALYSTS

The concentration of the reducing agent, sodiumborohydride, is much larger than nitro aromatics or azo dyes in all experiments thus it is assumed that its concentration does not change during the reaction. Thus, the kinetic equation of all reactions catalyzed by magnetic hybrids proceeds through pseudo-first-order kinetics and is shown as in Equation 4.1:

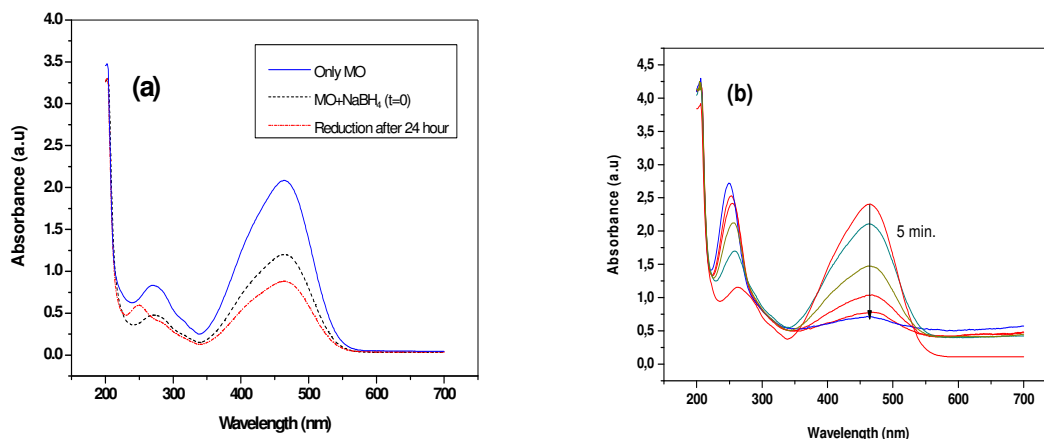
$$\ln(C_t/C_0)=\ln (A_t/A_0)= -kt \quad (4.1)$$

where  $k$  is the apparent reaction rate, the ratio of absorbance or concentration of aromatic nitro compound or azo dyes at  $t=0$  or  $t$  and  $t$  is the reaction time.

#### 4.1.1. Catalytic Tests of Fe<sub>3</sub>O<sub>4</sub>@Tween20-Ag Magnetic Nanocatalysts

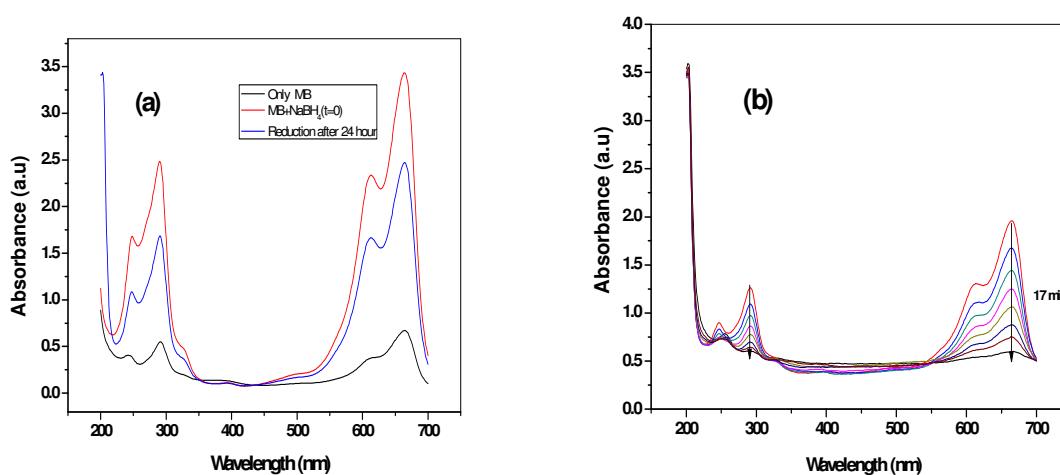
##### 4.1.1.1. *For azo dyes reduction*

Various types of azo dyes containing MO or MB were investigated. Figure 4.1a presents the absorbance of MO dye with the help of NaBH<sub>4</sub> as a reducing agent. It is seen that the 465 nm peak for MO did not change significantly after addition of NaBH<sub>4</sub> after 24 hr, which demonstrates that the reduction occurs but it is so very slow in the presence of NaBH<sub>4</sub>. On the other hand, when trace amount of Fe<sub>3</sub>O<sub>4</sub>@Tween20-Ag were added to the medium, the reaction was completed quickly thus it clearly shows that Fe<sub>3</sub>O<sub>4</sub>@Tween20-Ag has excellent catalytic performance for MO dye reduction.



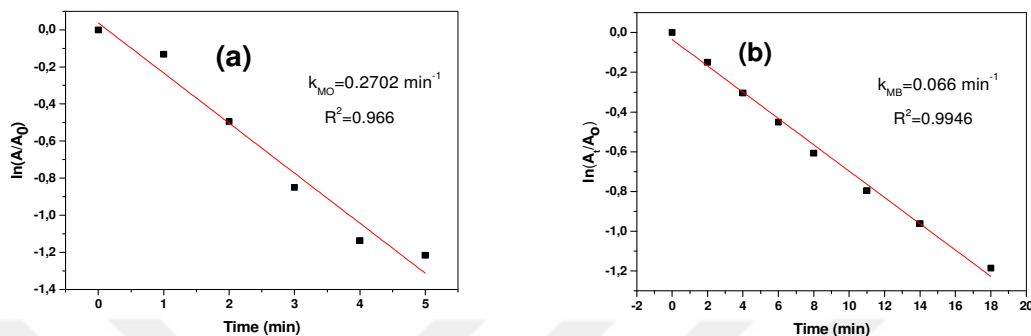
**Figure 4.1:** Absorbance of (a) MO dye, MO dye solution after immediate addition of NaBH<sub>4</sub> to MO and NaBH<sub>4</sub> solution after for 24 h; (b) MO dye and NaBH<sub>4</sub> mixture in the presence of Fe<sub>3</sub>O<sub>4</sub>@Tween20-Ag nanocatalyst.

MB is another kind of azo dye and presents as blue. It converts to its colorless form when a reducing agent is added since leuco methylene blue (LMB) is formed. As seen in Fig. 4.2., methylene blue reduction did not occur immediately when the magnetic nanocatalyst is absent. On the other hand, the main peak at 665 nm of MB disappeared in 17 min with the help of Fe<sub>3</sub>O<sub>4</sub>@Tween20-Ag, indicating that the Fe<sub>3</sub>O<sub>4</sub>@Tween20-Ag composites exhibit the catalytic activity for the degradation of methyl blue (Fig 4.2b).



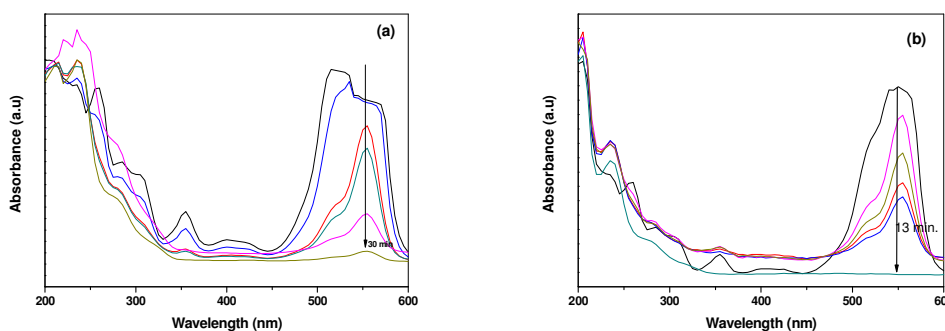
**Figure 4.2:** Absorbance of MB dye solution (a) after immediate addition of NaBH<sub>4</sub> to MB and NaBH<sub>4</sub> solution after reaction for 24 h; (b) with the help of Fe<sub>3</sub>O<sub>4</sub>@Tween20-Ag nanocatalyst.

Estimated from Figure 4.3a and 4.3b,  $k$  values were almost as  $0.27 \text{ min}^{-1}$  and  $0.066 \text{ min}^{-1}$  for methyl orange and methyl blue, respectively. Thus, it is suggested that  $\text{Fe}_3\text{O}_4@\text{Tween}20\text{-Ag}$  is more efficient nanocatalyst for MO reduction.



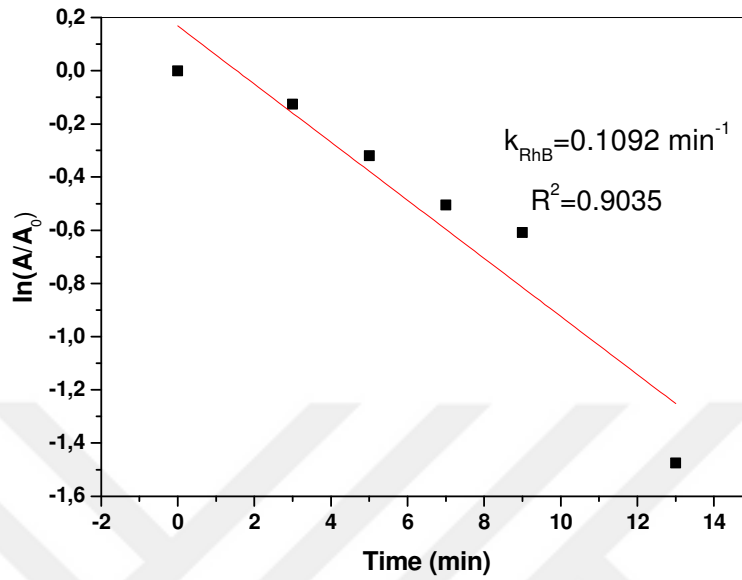
**Figure 4.3:** Plots of first order rates for reduction of (a) MO and (b) MB dye.

Similarly, another kind of an azo dye, RhB, which is a cationic dye was also studied. As shown in Fig 4.4a, RhB reduction happened half an hour using only  $\text{NaBH}_4$ . However, the reduction occurred in 13 min with  $\text{Fe}_3\text{O}_4@\text{Tween}20\text{-Ag}$  magnetic nanocatalyst as shown in Fig.4.4b which is a better value compared to Zhang's study in literature [63].

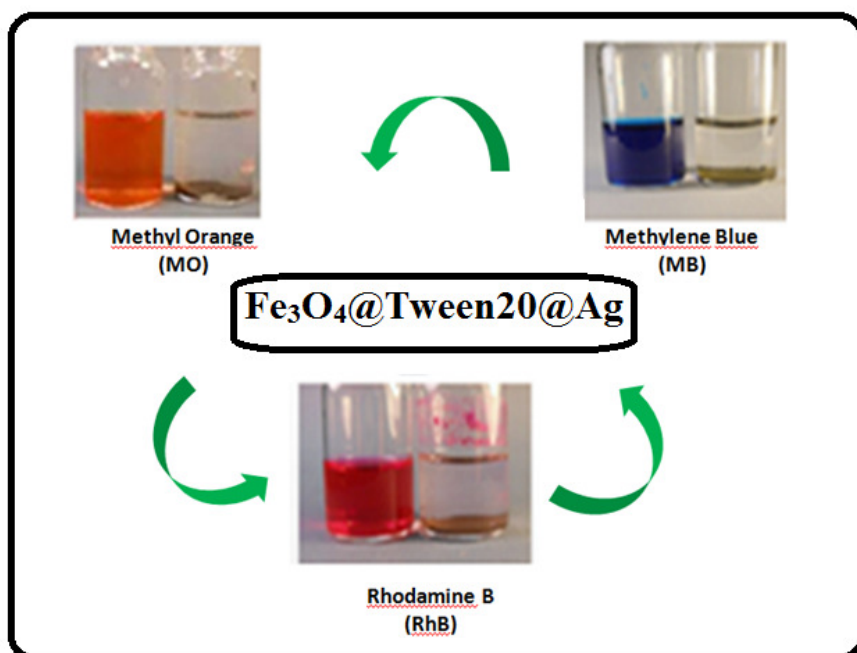


**Figure 4.4:** Absorbance of (a) RhB dye solution after immediate addition of  $\text{NaBH}_4$  only and (b) in the presence of  $\text{Fe}_3\text{O}_4@\text{Tween}20\text{-Ag}$  magnetic nanocatalyst.

Its reaction rate constant was found to be as almost  $0.1 \text{ min}^{-1}$  (Figure 4.5). As a consequence, this observation suggested that the dye's characters such as charge and hydrophobicity could effect the reduction rate of magnetic nanocatalyst [64]. The color changes before and after  $\text{Fe}_3\text{O}_4@\text{Tween}20@\text{Ag}$  addition to reaction medium is shown in Fig. 4.6.

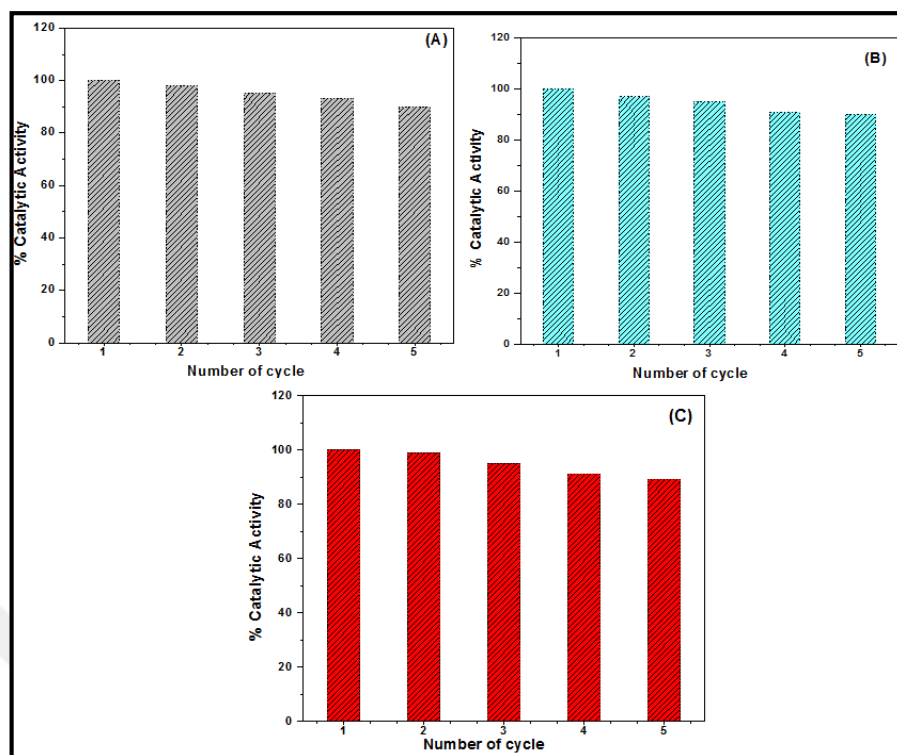


**Figure 4.5:** The relation between  $\ln(A_t/A_0)$  and reduction time for RhB reduction.



**Figure 4.6:** Photographs of the azo dyes catalytically reduced by  $\text{NaBH}_4$  with the help of  $\text{Fe}_3\text{O}_4@\text{Tween}20-\text{Ag}$  magnetic nanocatalyst.

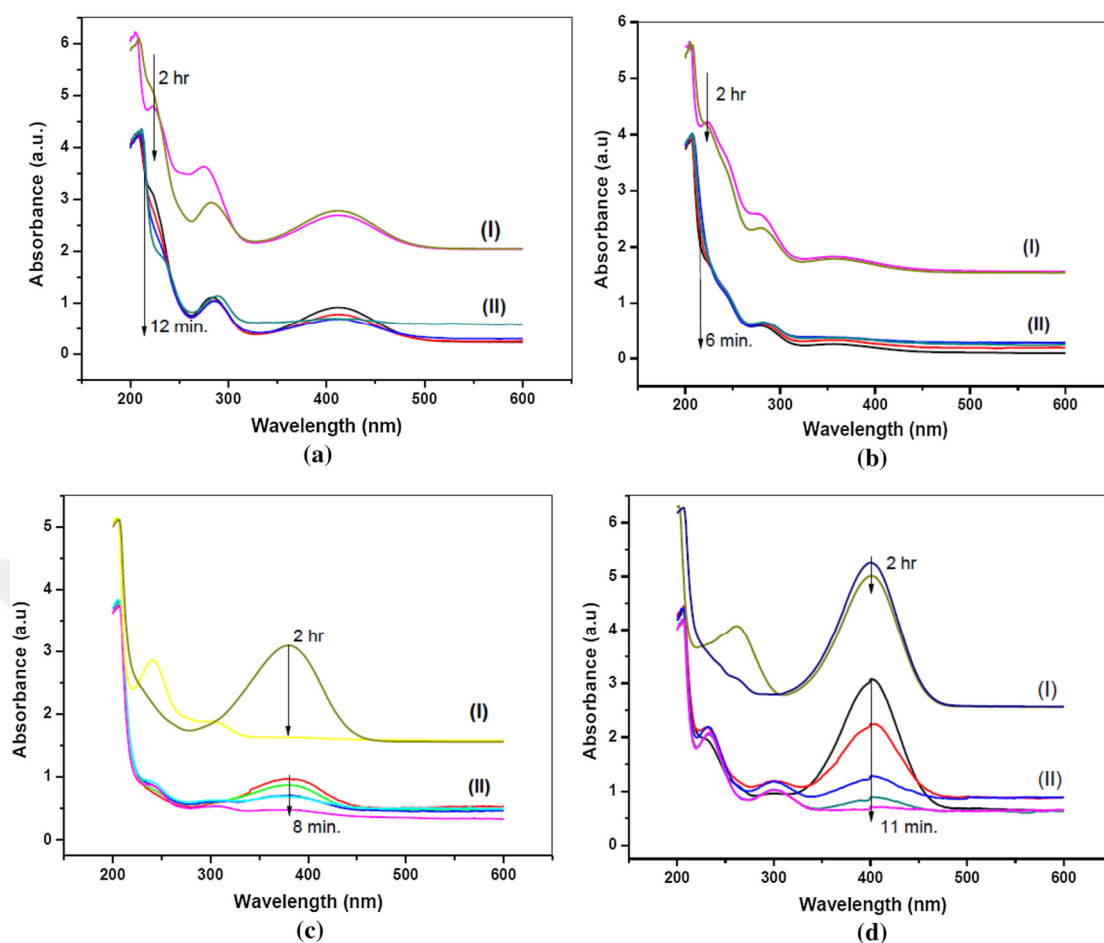
After a catalytic reaction is completed,  $\text{Fe}_3\text{O}_4@\text{Tween}20-\text{Ag}$  is recovered magnetically and could be used again to catalyze for other dye reduction reactions. Figure 4.7 represents the recyclability of the  $\text{Fe}_3\text{O}_4@\text{Tween}20-\text{Ag}$  and as understood from Figure 4.7, there is no significant change after five cycles of the catalysis reaction.



**Figure 4.7:** Changes in catalytic performance of  $\text{Fe}_3\text{O}_4@\text{Tween}20\text{-Ag}$  magnetic hybrid for (a) MO, (b) MB and (c) RhB azo dyes with  $\text{NaBH}_4$ , respectively.

#### 4.1.1.2. For nitroaromatics reduction

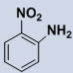
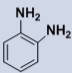
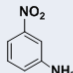
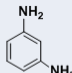
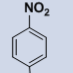
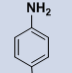
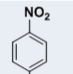
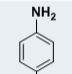
Various nitro aromatic compounds were chosen to investigate the catalytic activity of the prepared sample. The maximum signal at 400 nm unaltered by the addition of  $\text{NaBH}_4$  resulting that the reduction of 2-NA did not happen with the  $\text{NaBH}_4$  solution (Figure 4.8a). But the reaction lasted for only 12 min by the addition of 3 mg of  $\text{Fe}_3\text{O}_4@\text{Tween}20\text{-Ag}$  magnetic nanocatalyst and a new absorbance appeared due to the formation of the 2-phenylenediamine at 280 nm [65].



**Figure 4.8:**(I) Absorbance of (a) 2-NA, (b) 3-NA, (c) 4-NA and (d) 4-NP solution immediate addition of  $\text{NaBH}_4$  only and (II) one of nitro compounds and  $\text{NaBH}_4$  mixture in the existence of  $\text{Fe}_3\text{O}_4@\text{Tween}20\text{-Ag}$  nanocatalyst.

The reaction was stable during 2 hr and the absorbance at 280 nm did not change even after 2 hr. On the other hand, the maximum absorbance declined within 6 and 8 min for 3-NA and 4-NA with the help of  $\text{Fe}_3\text{O}_4@\text{Tween}20@\text{Ag}$  nanocatalyst, respectively (Figure 4.8b and 4.8c). For the degradation process of 4-NP, the intensity of maximum wavelength reduced after 11 min by the addition of  $\text{Fe}_3\text{O}_4@\text{Tween}20\text{-Ag}$  (Figure 4.8d). All these results showed that  $\text{Fe}_3\text{O}_4@\text{Tween}20\text{-Ag}$  was found to be efficient nanocatalyst for nitro compounds reduction reactions. All reaction rates and required reduction time are listed in Table 1.

**Table 4.1:** The reaction rates and time of various nitro compounds by Fe<sub>3</sub>O<sub>4</sub>@Tween20-Ag.

Entry	Substrate	Product	Time	Rate Constant (min <sup>-1</sup> )
1			12 min.	0.0142
2			6 min.	0.0793
3			8 min.	0.0109
4			12 min.	0.12

The catalytic degradation of aromatics on the surface of Ag or AuNPs was also frequently studied in literature. For example, Vadakkekra's research paper found the complete conversion to o-PPD was found to be as 8 min by their group [66]. In another research paper Le and his group members found that degradation of 2-nitroaniline with the help of Au based nanocatalyst took almost 12 min [65]. Compared to the all these literature surveys, Fe<sub>3</sub>O<sub>4</sub>@Tween20-Ag nanocatalyst showed superior catalytic performance.

For heterogeneous nanocatalysts, the level of recyclability is a key parameter. Thus, the recyclability of Fe<sub>3</sub>O<sub>4</sub>@Tween20-Ag nanocatalyst was examined here and four successive cycles of the catalytic hydrogenation reaction towards 4-NP were carried out (Figure 4.9b and c). 0.12 min<sup>-1</sup> was the *k* value obtained from the slope of the Figure 4.9a and this value was higher than reported literature values[67, 68]. In addition, stability and recyclability are significant for catalyst applications and therefore it was used for four cycles for the 4-NP reduction and rate constant slightly changed (Figure 4.9d).



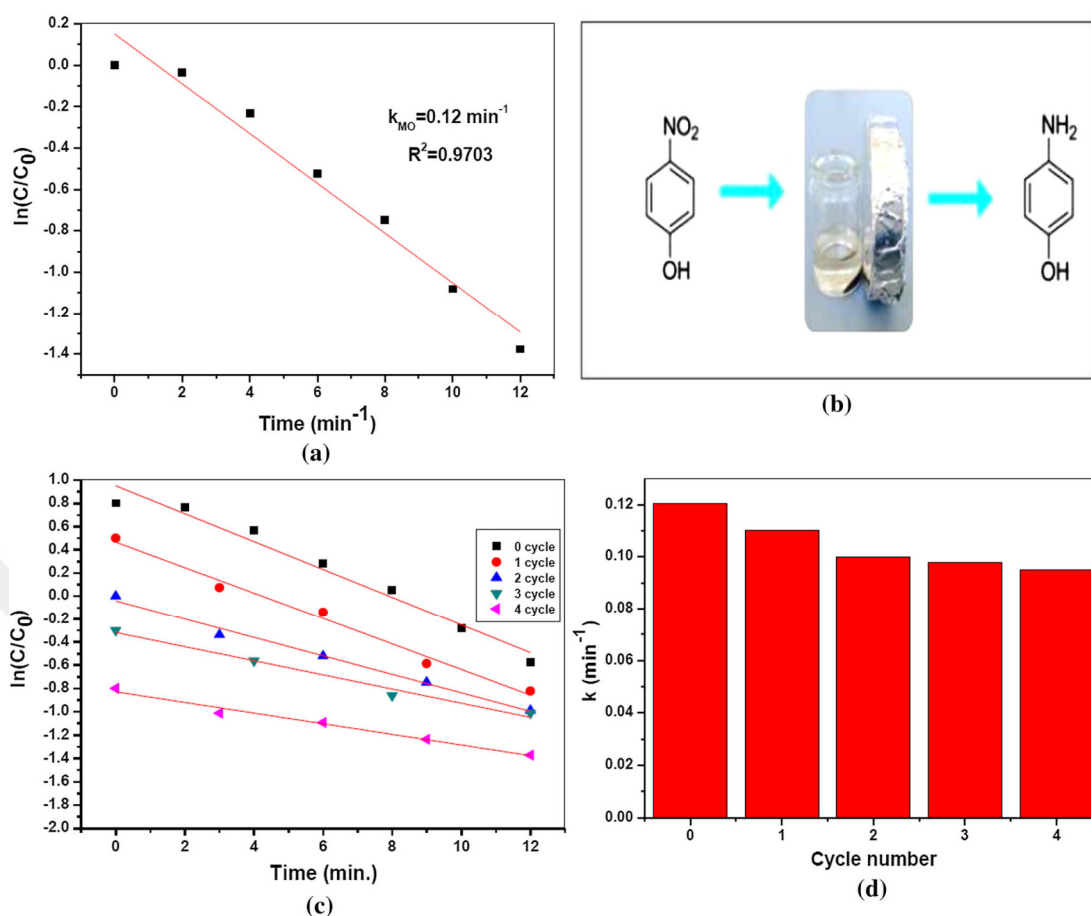


**Figure 4.9:**(a) The slope of straight line of  $\ln(C_t/C_0)$  vs. reaction time for 4-NP degradation (b) Photographs of the 4-NP catalytically reduced by  $\text{Fe}_3\text{O}_4@\text{Tween}20\text{-Ag}$  nanocatalyst and its magnetic separation (c) Graph of  $\ln(C_t/C_0)$  vs. time for four cycles and (d) Comparison of rate constants for each cycle.

#### 4.1.2. Catalytic Tests of $\text{Fe}_3\text{O}_4@\text{His}@\text{Cu}$ Magnetic Nanocatalysts

Pure MO dye has a specific absorption max. 465 nm in UV-vis spectra and it remains unchanged with time in existence of only  $\text{NaBH}_4$  (Fig. 4.10a). Upon addition of histidine coated magnetic nanocomposite, the absorbance at 465 nm quickly disappeared within 3 min and a new band gradually appeared which shows that Cu NPs are an efficient factor for the reduction of MO as seen in Figure 4.10b.  $\text{Fe}_3\text{O}_4@\text{His}@\text{Cu}$  nanocatalyst was removed by a magnetic filtration after reduction and the reactions were done again for recyclability. As shown in Figure 4.10c, rate constant of  $\text{Fe}_3\text{O}_4@\text{His}@\text{Cu}$  is found to be comparable and time needed to complete reduction of MO is less than written in literature since the magnetic properties play a significant role for an efficient of any catalyst [69-71]. Figure 4.10d presents that catalyst particles are active after separation from the medium and the activity of the

product reduced since the loss of catalyst can not be avoided during the procedure of separation after four successive cycles.

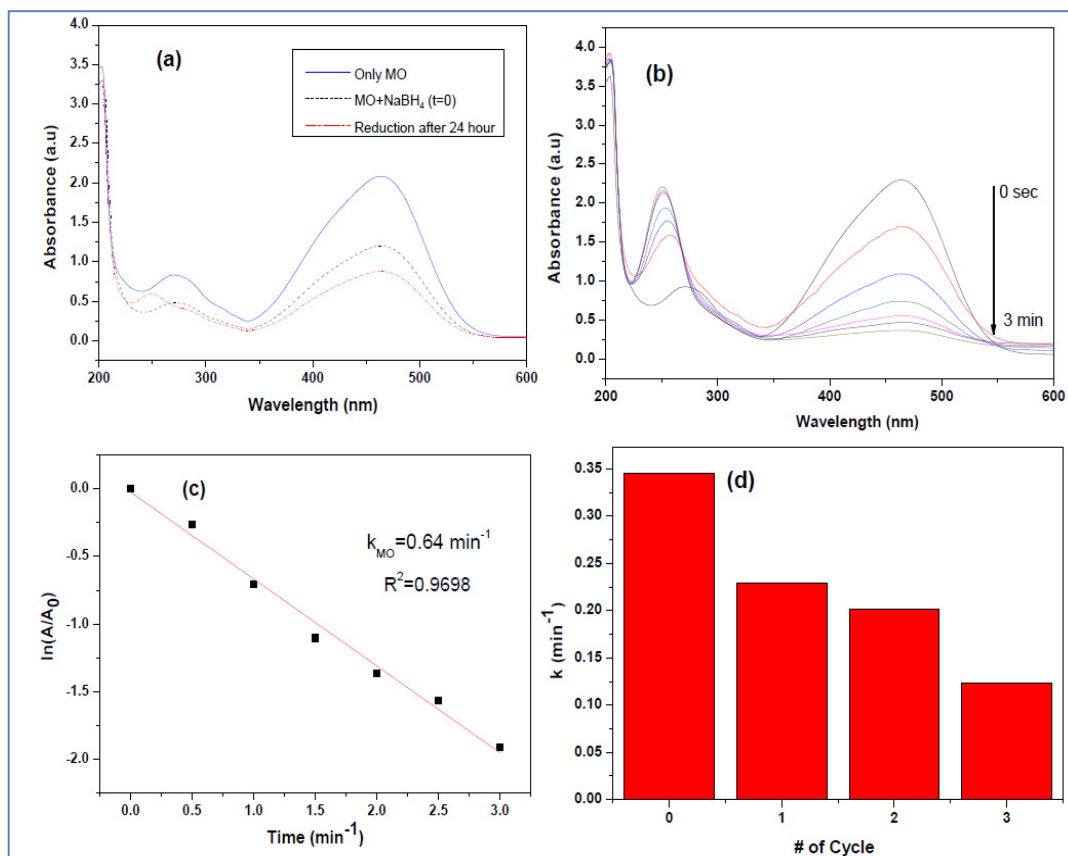


**Figure 4.10:** Absorption spectra of MO dye (a) after immediate addition of  $\text{NaBH}_4$  only, (b) methyl orange and sodiumborohydride mixture in the existence of  $\text{Fe}_3\text{O}_4@\text{His}@\text{Cu}$  as nanocatalyst, (c) the first order kinetic plot for MO degradation and (d) catalytic activity of  $\text{Fe}_3\text{O}_4@\text{His}@\text{Cu}$  in different cycling number.

The catalytic properties of  $\text{Fe}_3\text{O}_4@\text{His}@\text{Cu}$  catalyst were also studied extensively for MB reduction. Figure 4.11a presents the main absorption peak of MB at 665-670 nm and did not change over two days without nanocatalyst. However,  $\text{Fe}_3\text{O}_4@\text{His}@\text{Cu}$  nanocatalyst was present in the solution, the band intensity at 665-670 nm disappeared within only 4 min. as seen in Figure 4.11b. It clarifies that  $\text{Fe}_3\text{O}_4@\text{His}@\text{Cu}$  nanocomposite catalyzes the reaction and reduces MB rapidly.  $0.39 \text{ min}^{-1}$  was the  $k$  value as illustrated in Figure 4.11c which is higher than reported catalysts [71]. In addition to catalytic activity, we have also carried out the cycling test to study the reusability of  $\text{Fe}_3\text{O}_4@\text{His}@\text{Cu}$  nanocatalyst. We repeat the

separation-reuse cycles 3 times (Fig. 4.11d). The mass of catalyst decreased during separation process therefore it causes to decrease in rate constants.

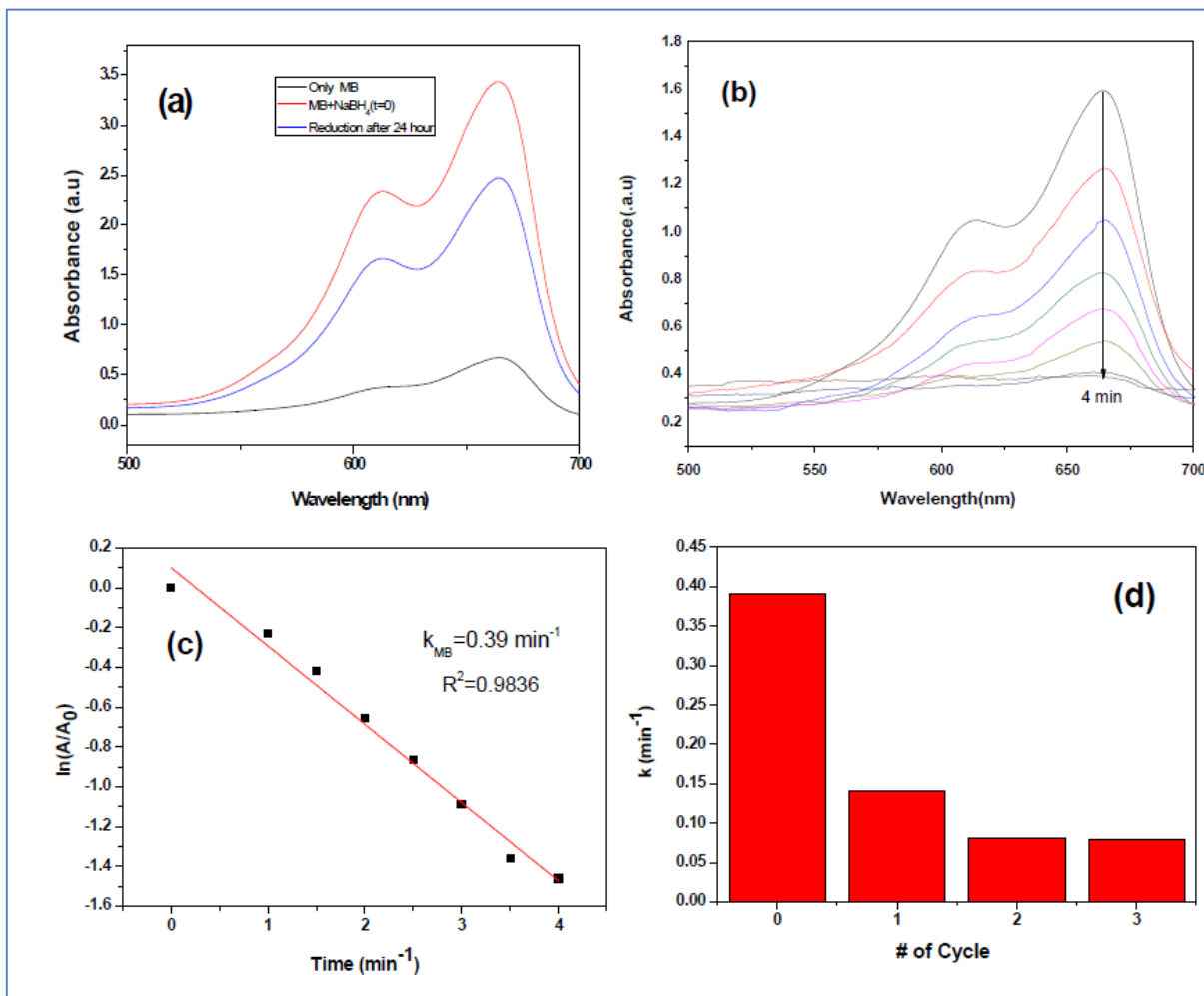


**Figure 4.11:** Absorbance of (a) methyl blue solution by only NaBH<sub>4</sub> and (b) methyl blue NaBH<sub>4</sub> mixture with the help of  $\text{Fe}_3\text{O}_4@\text{His}@\text{Cu}$  as nanocatalyst, (c) first order kinetic plot of MB reduction using  $\text{Fe}_3\text{O}_4@\text{His}@\text{Cu}$  as catalyst and (d) catalytic activity of  $\text{Fe}_3\text{O}_4@\text{His}@\text{Cu}$  in different cycling number.

Furthermore, the simultaneous reduction was also studied by mixing of each 10 mM of MO and MB (100  $\mu\text{l}$ ) and 100 mM of NaBH<sub>4</sub> (1 ml) catalyzed by  $\text{Fe}_3\text{O}_4@\text{His}@\text{Cu}$  as seen in Figure 4.12a. It was found that the reduction of MB happened more rapidly than that of MO (Figure 4.12b and 4.12c).

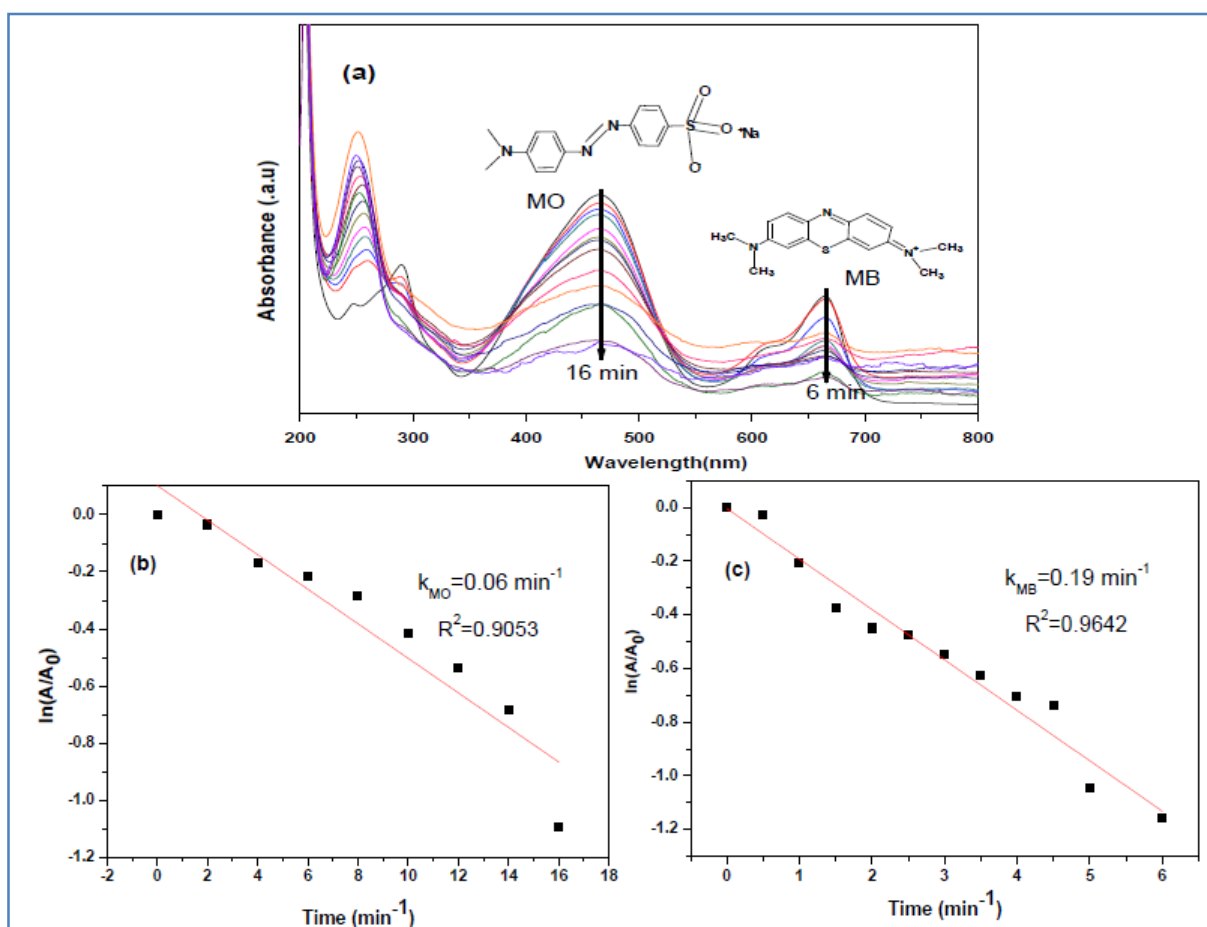


**Figure 4.12:** Absorbance of (a) azo dyes and reducing agent mixture with the help of  $\text{Fe}_3\text{O}_4@\text{His}@\text{Cu}$  as nanocatalyst, (b) first order kinetic plot of MO and (c) MB reduction using  $\text{Fe}_3\text{O}_4@\text{His}@\text{Cu}$  as catalyst.

It is well known that the composition of any nanocatalyst influences its catalytic activity [69, 72]. Figure 4.13 showed the mechanism of any azo dye after being catalyzed  $\text{Fe}_3\text{O}_4@\text{His}@\text{Cu}$  in the existence of borohydrate ions. Dyes and borohydrate ions are hold on Cu NPs surface of  $\text{Fe}_3\text{O}_4@\text{His}@\text{Cu}$  nanocatalyst, the reduction happens with transfer of  $e^-$ s from the donor  $\text{BH}_4^-$  to the acceptor dyes.

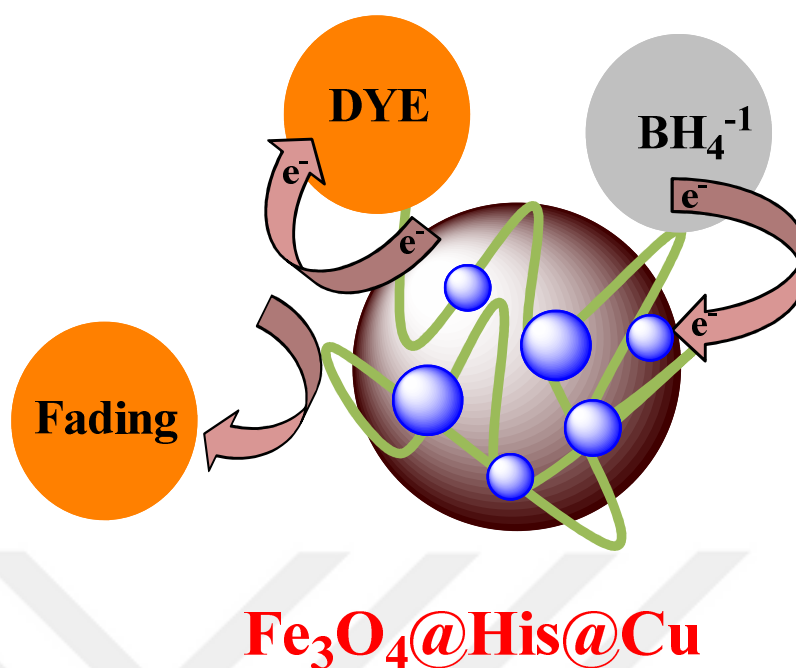


**Figure 4.13:** The mechanism of any azo dye on Fe<sub>3</sub>O<sub>4</sub>@His-Cu nanocatalyst surface in the reduction process.

#### 4.1.3. Catalytic Tests of Fe<sub>3</sub>O<sub>4</sub>@His-Ag Magnetic Nanocatalysts

As shown in Figure 4.14a, pure MO dye gives a specific absorption max. at 465 nm and the reduction did not complete even after 24 hr. However, as shown in Figure 4.14b, after adding the Fe<sub>3</sub>O<sub>4</sub>@His-Ag nanocatalyst into the reaction of MO and NaBH<sub>4</sub> mixture, the reaction was completed within 8 min becoming colorless after the reaction. The photographs before and after reaction were seen in Figure 4.15.

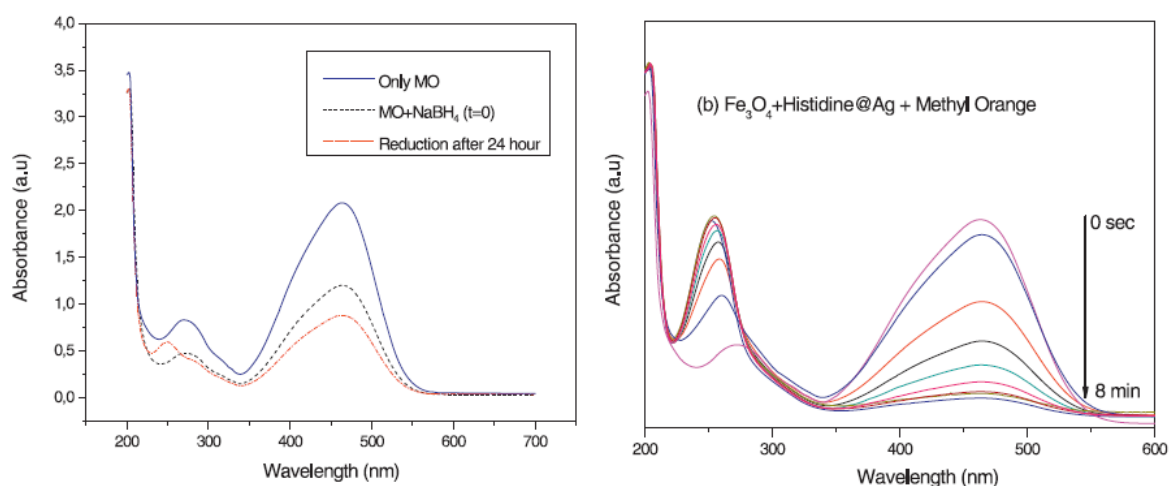


**Figure 4.14:** Absorbance of (a) MO solution by only  $\text{NaBH}_4$  and (b) MO and  $\text{NaBH}_4$  mixture in the existence of  $\text{Fe}_3\text{O}_4@\text{His-Ag}$ .

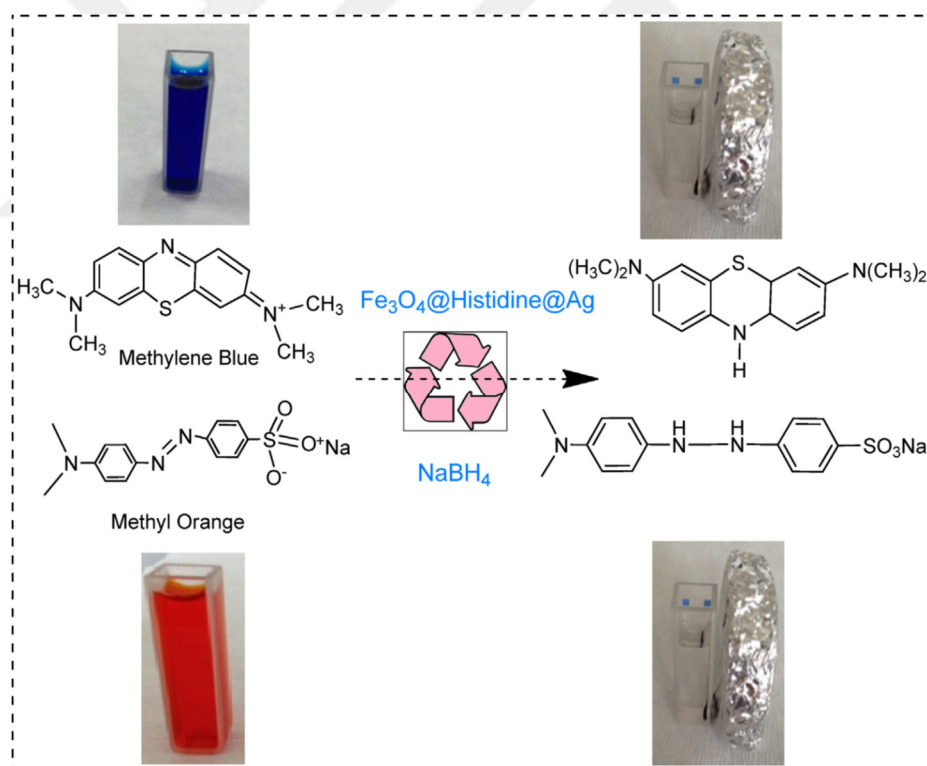


**Figure 4.15:** Photographs of azo dyes reduction in the presence of and  $\text{Fe}_3\text{O}_4@\text{His-Ag}$  and  $\text{NaBH}_4$  nanocatalyst.

MB reduction in the absence and existence of  $\text{Fe}_3\text{O}_4@\text{His}@\text{Ag}$  nanocatalyst results are seen in Figure 4.16. According to the Figure 4.16a, the absorbance at 665 nm did not change so much even after 24 hr without the  $\text{Fe}_3\text{O}_4@\text{His}-\text{Ag}$  nanocatalyst. However, when trace amount of the  $\text{Fe}_3\text{O}_4@\text{His}-\text{Ag}$  nanocatalyst was reacted with the solution, the band at 665 nm reduced slowly and disappeared within 4 min., which clearly demonstrates that the  $\text{Fe}_3\text{O}_4@\text{His}-\text{Ag}$  nanocatalyst is an efficient catalyst for MB dye reduction (Figure 4.16b).

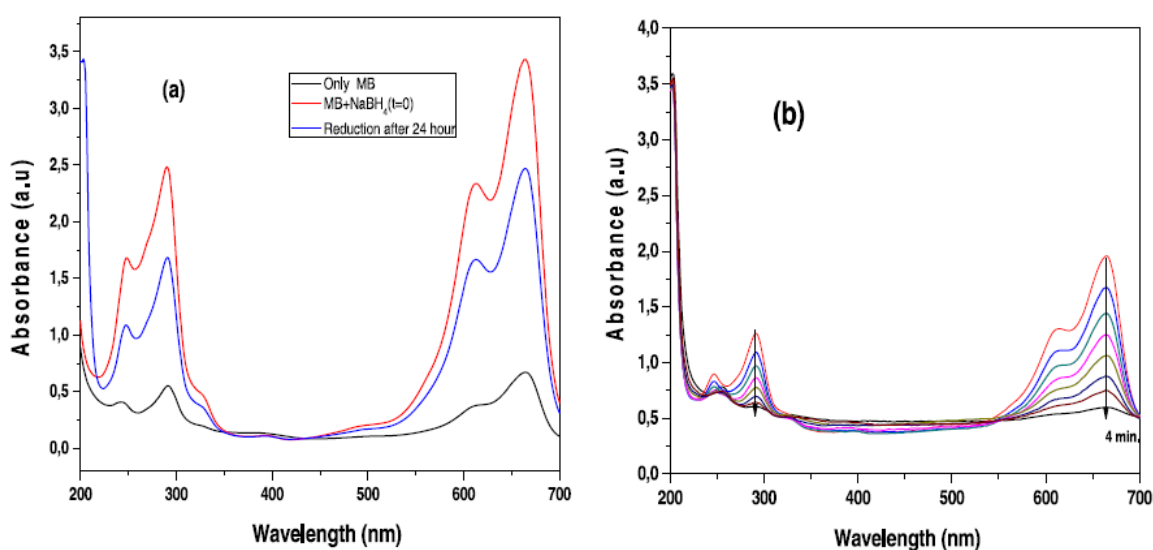


**Figure 4.16:** Absorbance of (a) MB and (b) MB and  $\text{NaBH}_4$  mixture in the existence of  $\text{Fe}_3\text{O}_4@\text{His}-\text{Ag}$  as nanocatalyst.

Their reduction kinetics were also investigated and Figure 4.17 showed the logarithmic slope of the absorbance of azo dyes separately with respect to time. The  $k$  values for degradation of methyl orange and methyl blue of MO and MB are  $0.270$  and  $0.254 \text{ min}^{-1}$ , respectively. Figure 4.18 also proved that the catalytic activity did not change significantly after four cycles, which demonstrated that the synthesized product exhibited superior performance for MO and MB reduction.

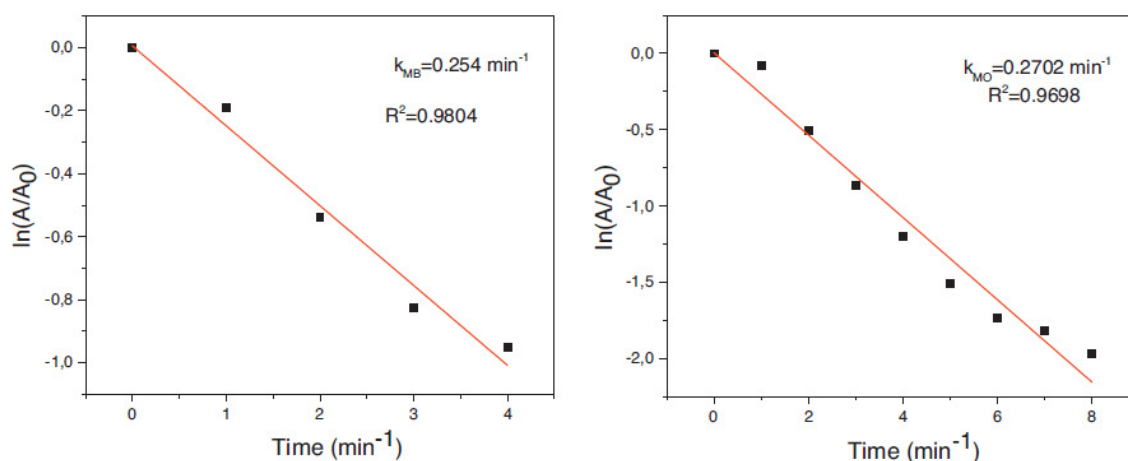


**Figure 4.17:** The kinetic curve of azo dyes reduction using  $\text{Fe}_3\text{O}_4@\text{His-Ag}$  as nanocatalyst, respectively.

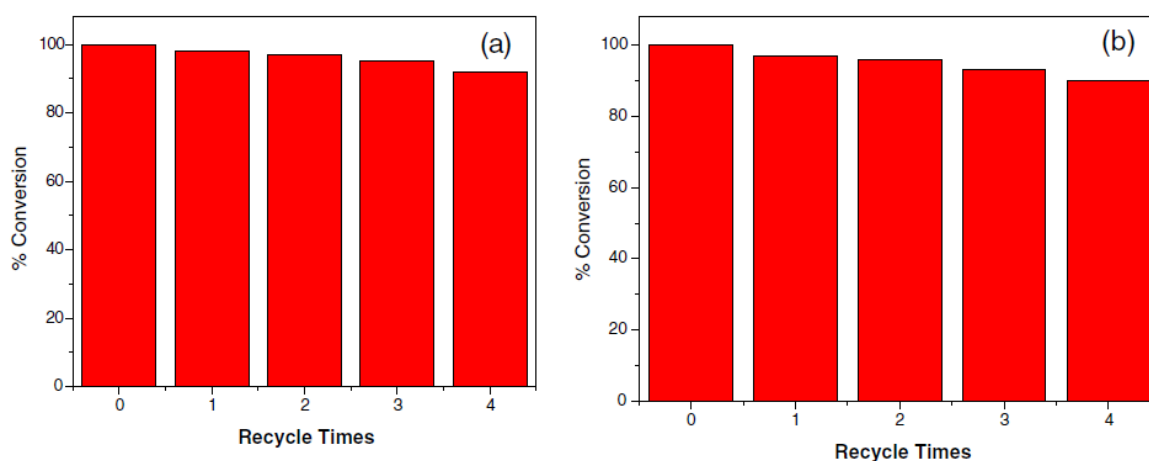


**Figure 4.18:** Changes in conversion of (a) MO and (b) MB reduction as the cycling continues.

#### 4.1.4. Catalytic Tests of $\text{Fe}_3\text{O}_4@\text{Nico-Ag}$ Magnetic Nanocatalysts

##### 4.1.4.1. For Nitro aromatics

The catalytic behaviour of nicotinic acid coated magnetic nanoparticle was demonstrated in Figure 4.19a. It showed that the absorbance at 400 nm did not change over 5 hr (Fig 4. 20a). However, as soon as the  $\text{Fe}_3\text{O}_4@\text{Nico-Ag}$  was added to 4-NP solution, the maximum absorption intensity reduced quickly indicating of destruction of nitrate group and production 4-aminophenol (Fig 4.20c). Similarly, the catalytic behaviour of  $\text{Fe}_3\text{O}_4@\text{Nico-Ag}$  towards 4-NA reduction was studied. As understood from Figure 4.20 b, max absorbance remained same



when the time passed but the peak at 380 nm for 4-NA disappeared within only 4 minute (Fig 4.20d). It clarifes that 4-NA reduction by  $\text{Fe}_3\text{O}_4@\text{Nico-Ag}$  magnetic hybrid in the existence of sodiumborohydride was achieved succesfully as shown in Fig. 4.20d [73-76].

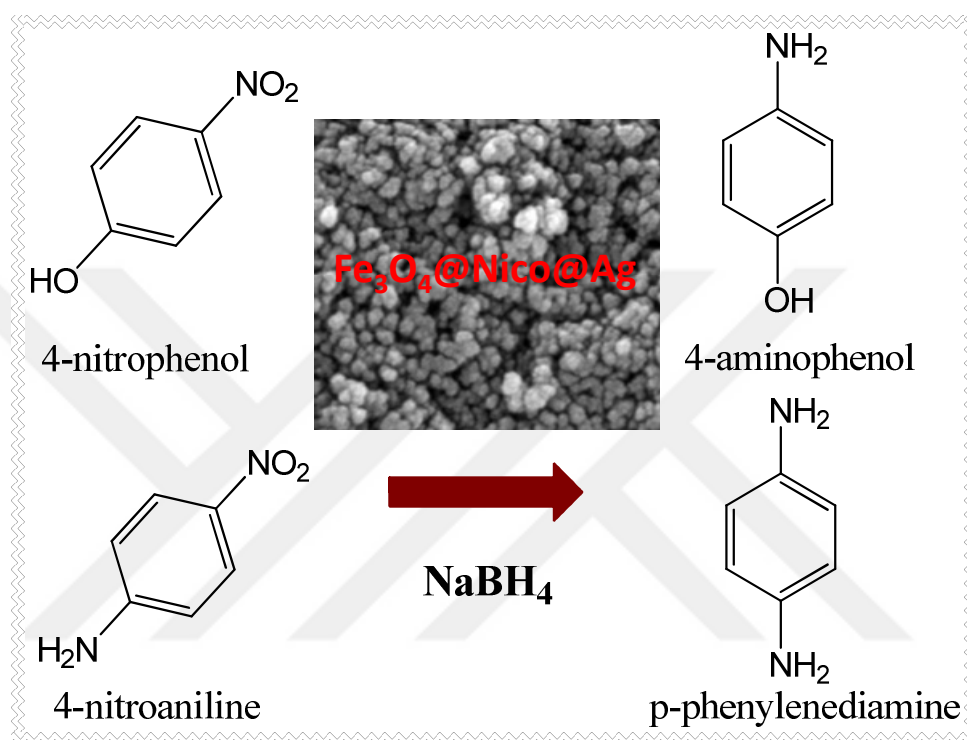


**Figure 4.19:** The schematic illustration for the reduction of 4-nitrophenol and 4-nitroaniline compounds in the existence of  $\text{Fe}_3\text{O}_4@\text{Nico-Ag}$  nanocatalyst.

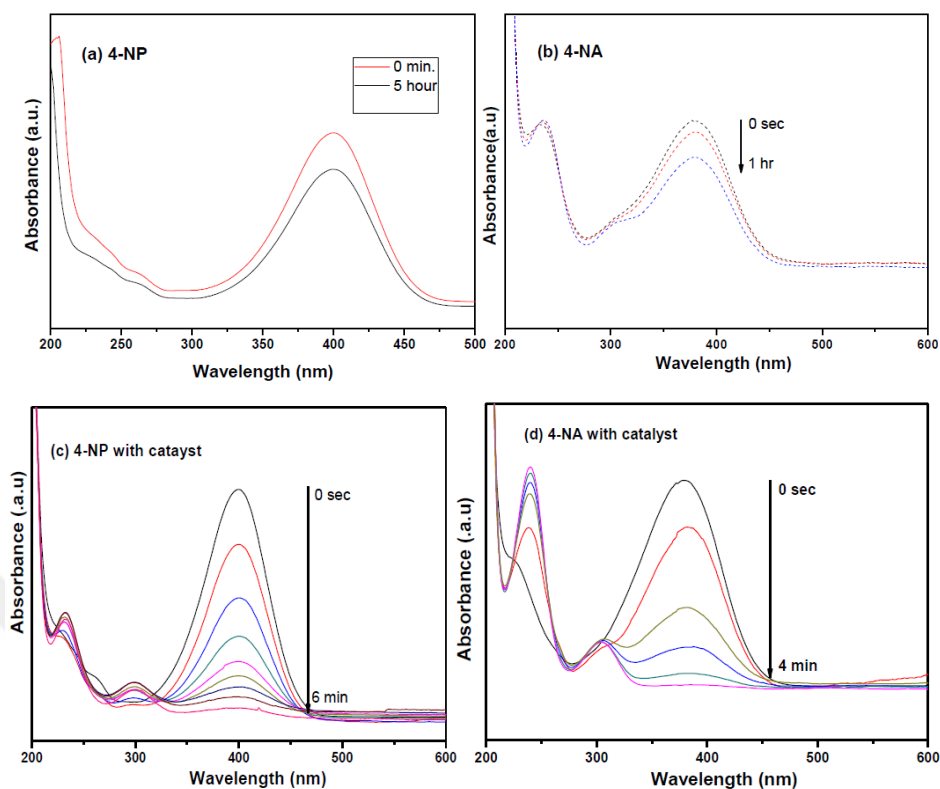


**Figure 4.20:** Absorbance of (a) 4-NP and (b) 4-NA by only  $\text{NaBH}_4$  and (c) 4-NP and (d) 4-NA with the help of  $\text{Fe}_3\text{O}_4@\text{Nico-Ag}$  magnetic hybrid.

The catalytic performance of Ag nanoparticle loaded Nicotinic acid coated magnetic nanoparticle nitro aromatics was also investigated. After 7 min, the intensity of  $\lambda_{\text{max}}$  disappeared (Figure 4.21).  $0.35 \text{ min}^{-1}$  was the k value and these results were higher than reported literature studies [77, 78].

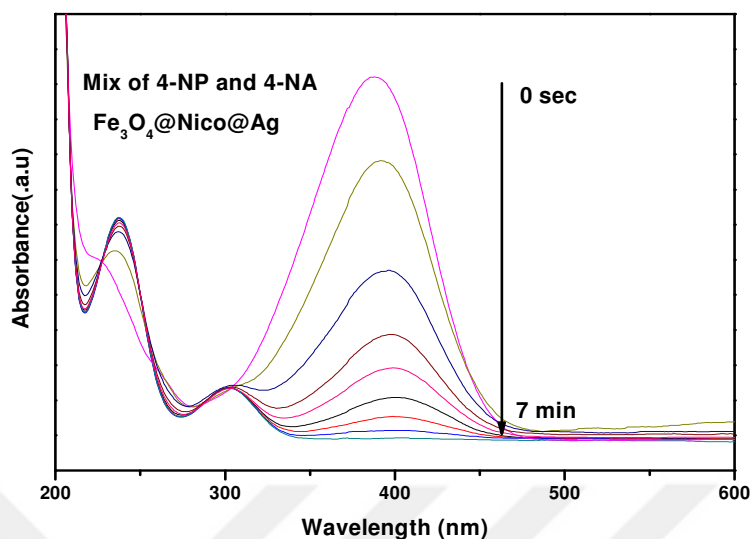


**Figure 4.21:** Absorbance for the reduction process of mixture of 4-NP and 4-NA compounds.

The reaction rate constants were estimated to be  $0.35$  and  $0.50 \text{ min}^{-1}$  for 4-nitrophenol and 4-nitroaniline, respectively (Figure 4.22a). The reusability, another important key parameter for the recyclable magnetic nanocatalysts, was also investigated and it did show significant change for nitro compounds reduction up to three cycles (Figure 4.22b).

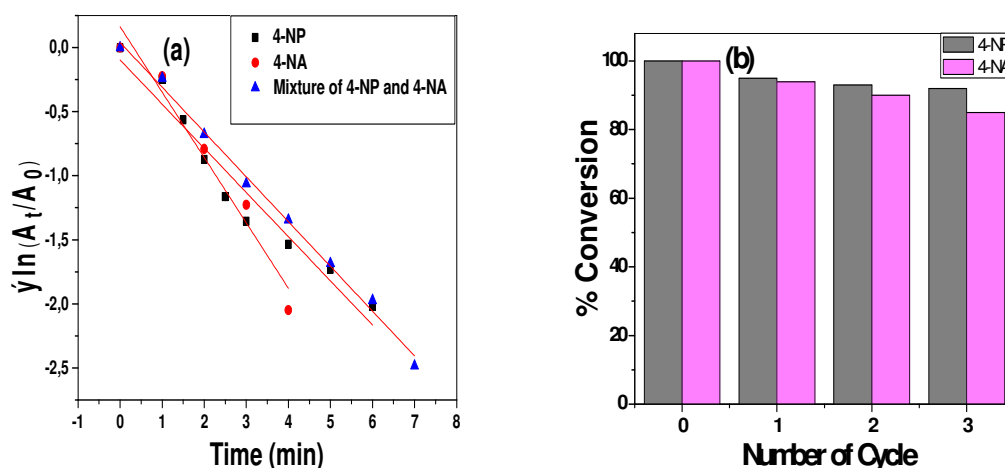


**Figure 4.22:** The relation between  $\ln(A_t/A_0)$  and reduction time using  $\text{Fe}_3\text{O}_4@\text{Nico}@\text{Ag}$  as nanocatalyst and (b) Changes in conversion of 4-NP and 4-NA as the cycling continues.

#### 4.1.4.2. For Azo dyes

Furthermore, we also studied the catalytic properties of Ag loaded  $\text{Fe}_3\text{O}_4@\text{Nico}$  nanocomposite by investigating the degradation of different kinds of azo dyes. The same procedure which is explained above for nitro compounds was applied in this section. Instead of nitro compounds, one of azo dyes was added into the reaction solution followed by Ag loaded  $\text{Fe}_3\text{O}_4@\text{Nico}$  nanocomposite addition in the existence of sodiumborohydride. The maximum wavelength ( $\lambda_{\text{max}}$ ) of azo dyes did not change for more than 1h after sodiumborohydride was added (Figure 4.23).

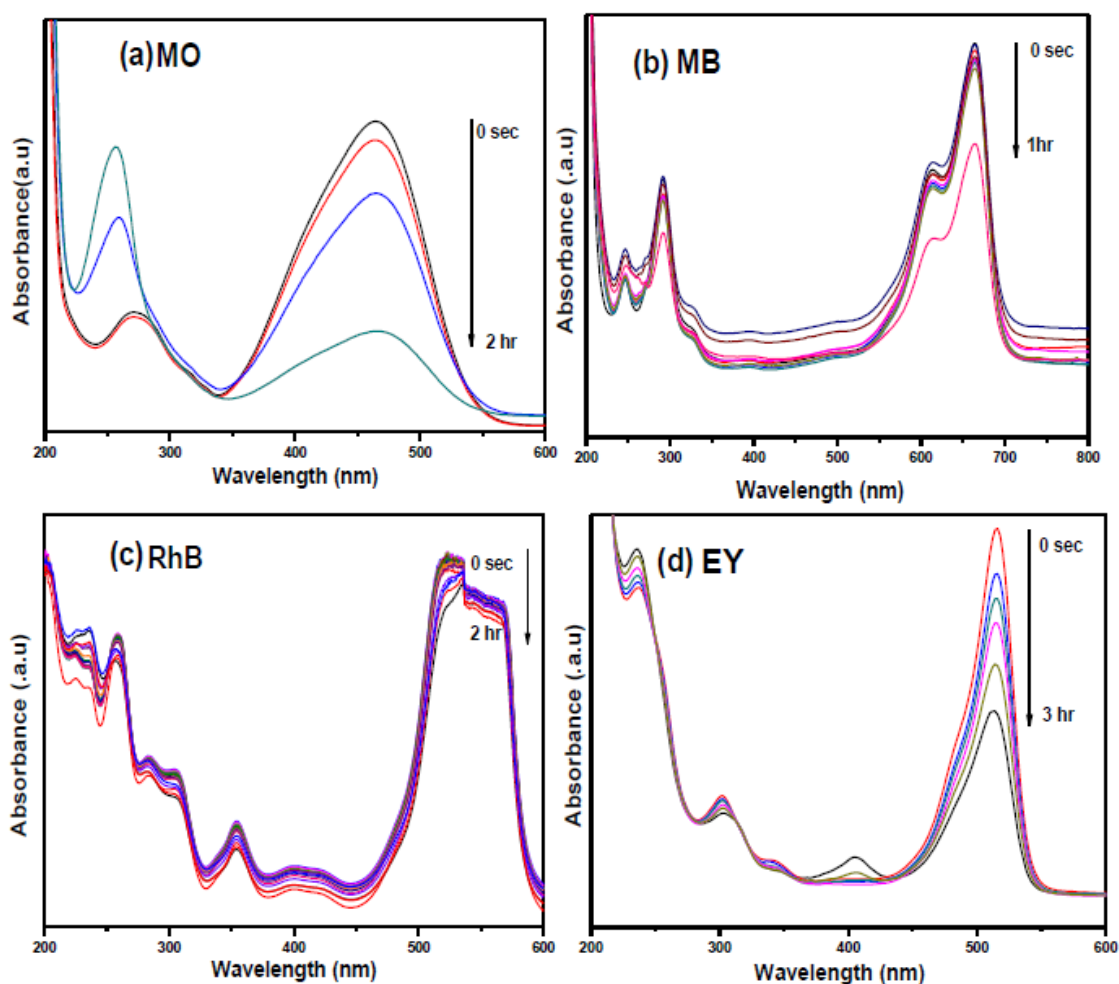


**Figure 4.23:** Absorbance of various azo dyes in the presence of  $\text{NaBH}_4$  only.

As represented in Figure 4.24, the absorbance at  $\lambda_{\text{max}}$  declined and delocalization occurred within different times with the help of Ag loaded nicotinic acid coated  $\text{Fe}_3\text{O}_4$  nocomposite. This time difference was probably because of the different functional groups such as hydroxyl

or methyl. It was clearly seen that the catalytic reduction was also found to be successful for all of them. Previous studies showed that nano Ag NPs have good catalytic performance on various amounts of organic materials like nitro aromatics or azo dyes and have significant effect for azo dyes reduction [63, 69, 79].

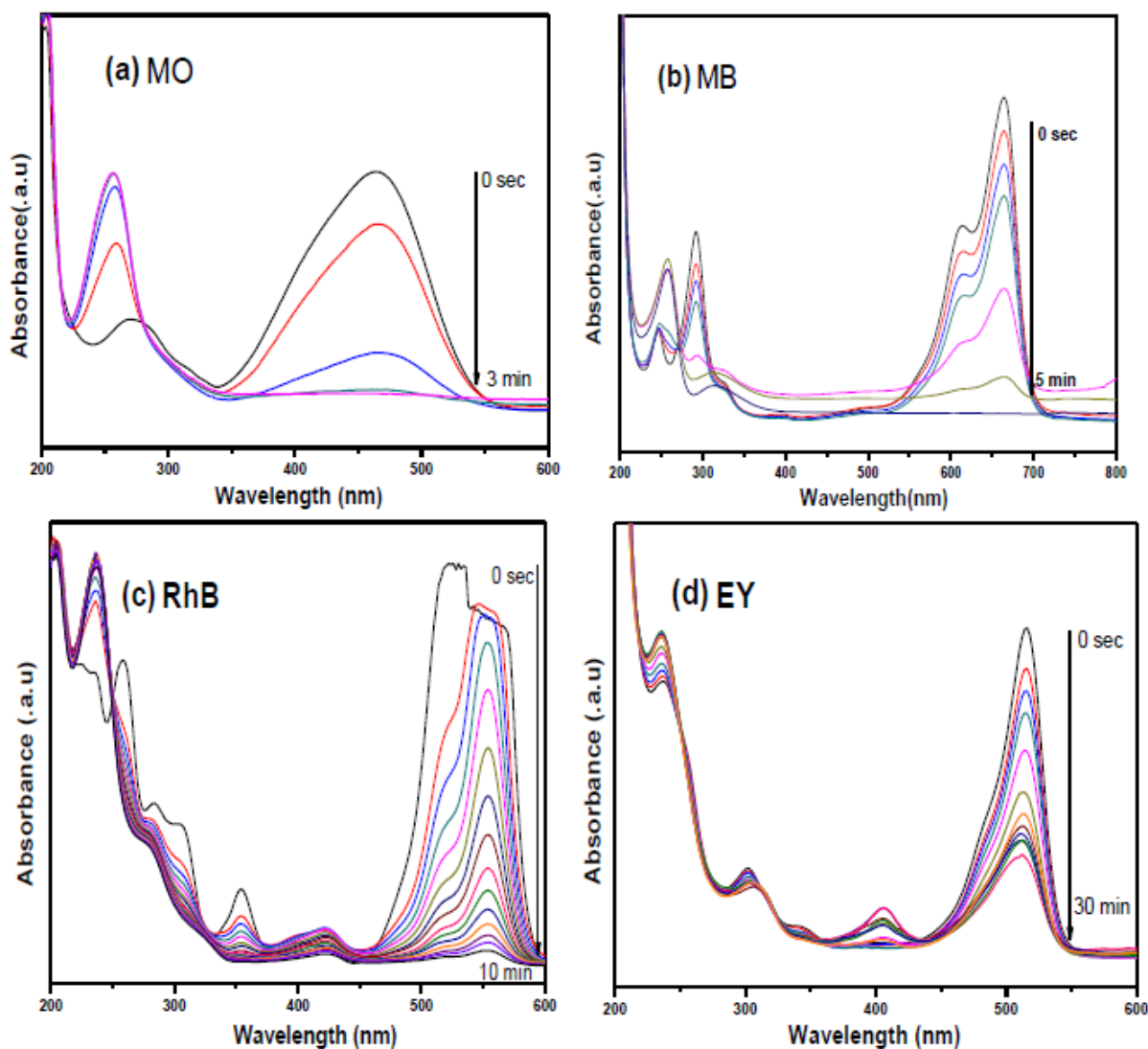


**Figure 4.24:** (a) Absorbance of various azo dyes with the help of  $\text{Fe}_3\text{O}_4@\text{Nico-Ag}$ .

Figure 4.25a showed slopes of  $\ln(A_t/A_0)$  with reduction time for the catalysts. The  $k$  values were summarized in Table 2. The highest rate was for MO azo dye and the rate values were better than reported ones [32, 80]. The recovery of Ag loaded  $\text{Fe}_3\text{O}_4@\text{Nico}$  nanocomposite was studied for only MB dye and is shown in Figure 4.25b. It is seen that the conversion

efficiency reduced after four cycle, this could be due to the loss of nanocatalyst during recycle process.

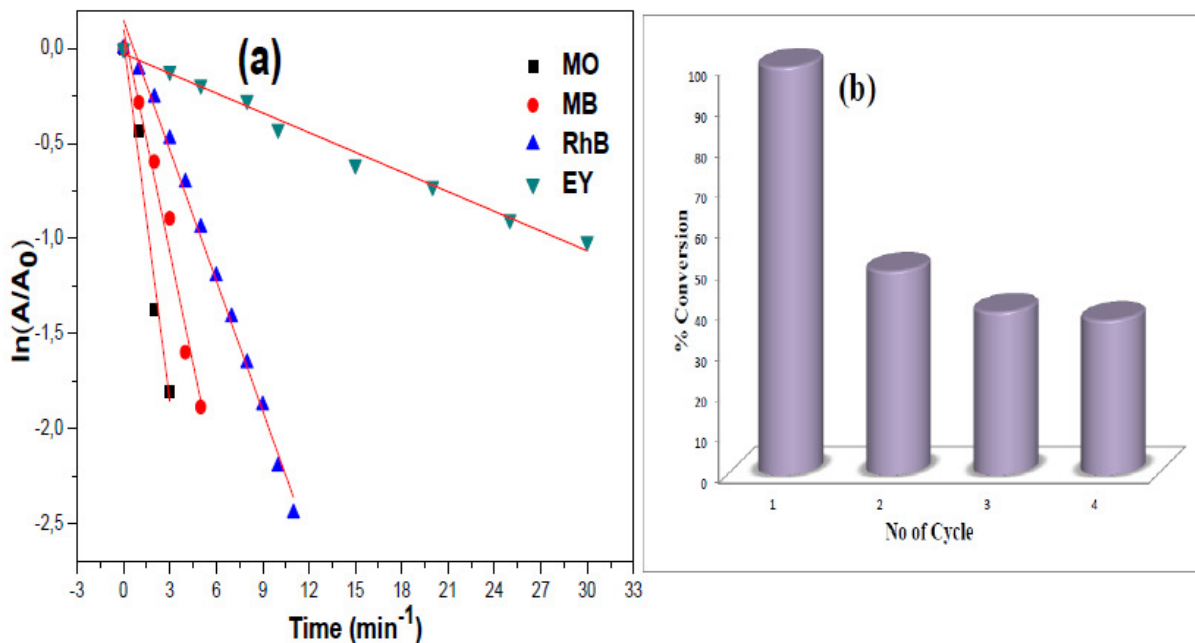


**Figure 4.25:**(a) Plots of first order rate for reduction of various azo dyes and (b) Changes in catalytic activity of  $\text{Fe}_3\text{O}_4@\text{Nico-Ag}$  in different cycling number.

**Table 4.2:** The required time and  $k$  for the reduction reactions of MO, MB, RhB and EY.

Azo Dye	Completion Time ( $\text{min}^{-1}$ )	Rate Constant ( $k$ )	Correlation Coefficient <sup>a</sup>
<u>Methyl Orange (MO)</u>	3	0.64	0.97
<u>Methylene Blue (MB)</u>	5	0.40	0.98
<u>Rhodamine B (RhB)</u>	10	0.23	0.99
<u>Eosin Y (EY)</u>	30	0.04	0.99

It has been experimentally demonstrated that Ag loaded  $\text{Fe}_3\text{O}_4@\text{Nico}$  nanocomposite was also effective nanocatalyst for dye mixtures reduction in the existence of sodiumborohydride as the reducing agent (Figure 4.26a). It was seen MB was reduced faster than MO and was

probably related to the dye properties and the reaction rates were also calculated (Figure 4.26b) [81].

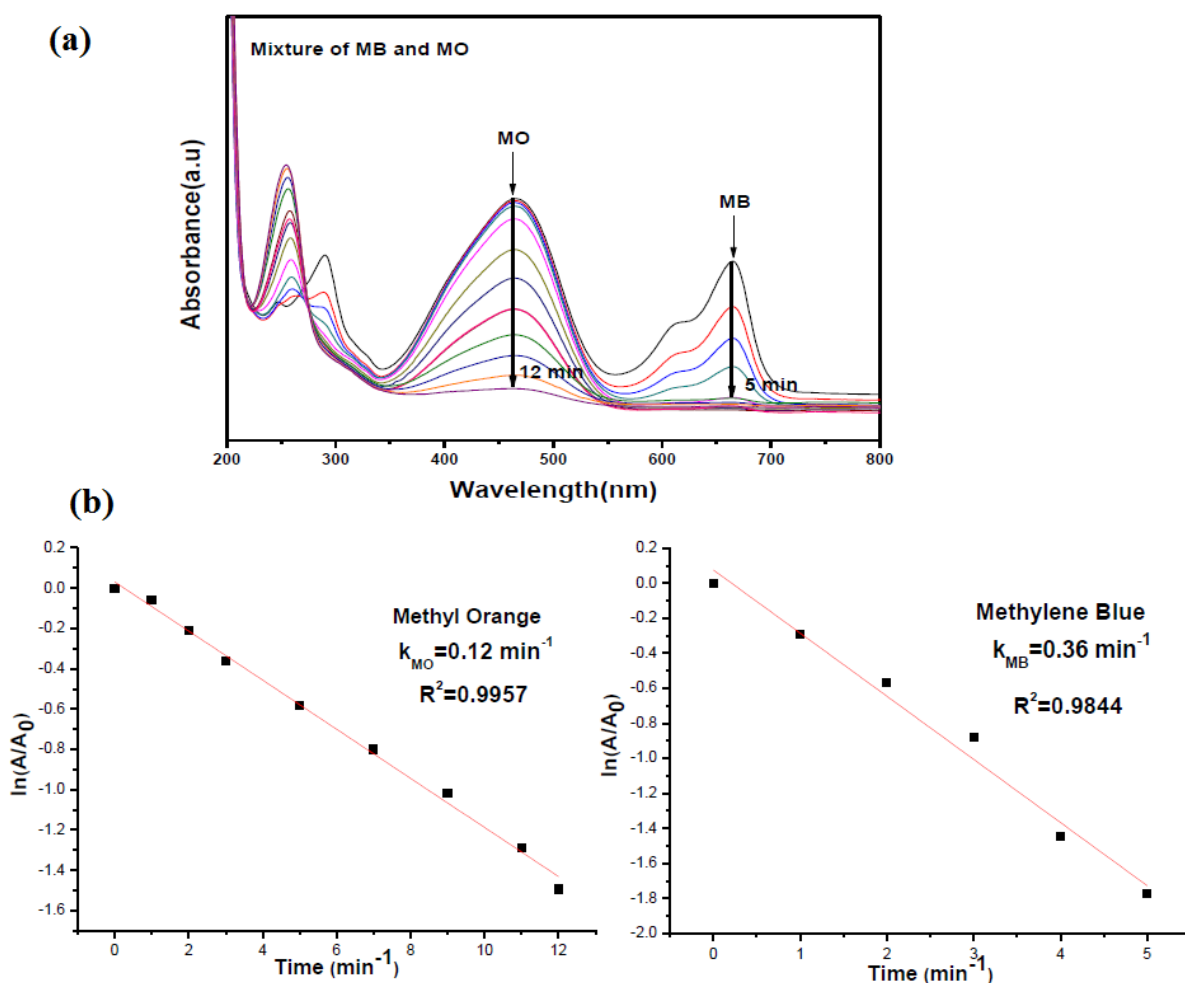


**Figure 4.26:** (a) Absorbance for the degradation of azo dye mixtures with the help of  $\text{Fe}_3\text{O}_4@\text{Nico-Ag}$  and (b) Plots of first order rate of azo dyes.

The reduction of rhodamine B and eosin Y was also investigated to report the catalytic performance as synthesized material. It took only 6 min. and RhB was reduced faster than EY as seen in Figure 4.27. This result was compatible with Sun Lijuan's study in the literature [32]. Figure 4.28 represented the performance of Ag loaded  $\text{Fe}_3\text{O}_4@\text{Nico}$  nanocomposite during reduction of azo dyes and their leuco forms by  $\text{NaBH}_4$ .

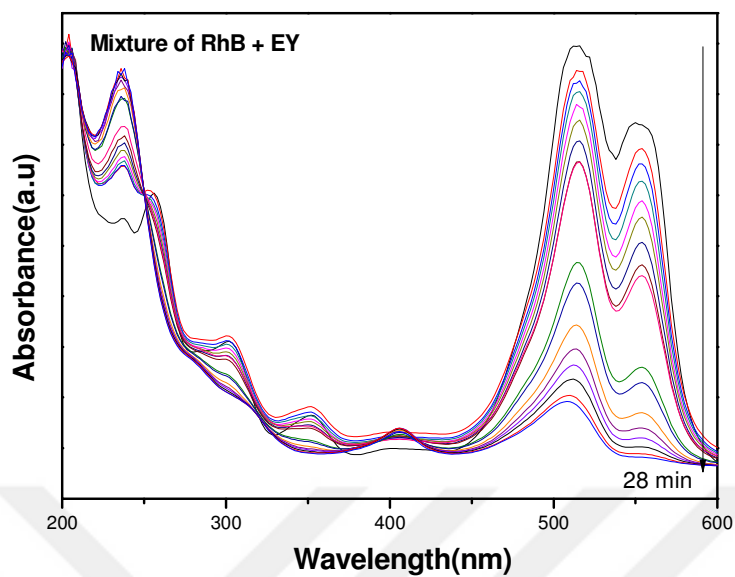


Figure 4.27: Absorbance of azo dye mixtures with the help of  $\text{Fe}_3\text{O}_4@\text{Nico}@\text{Ag}$  nanocatalyst.

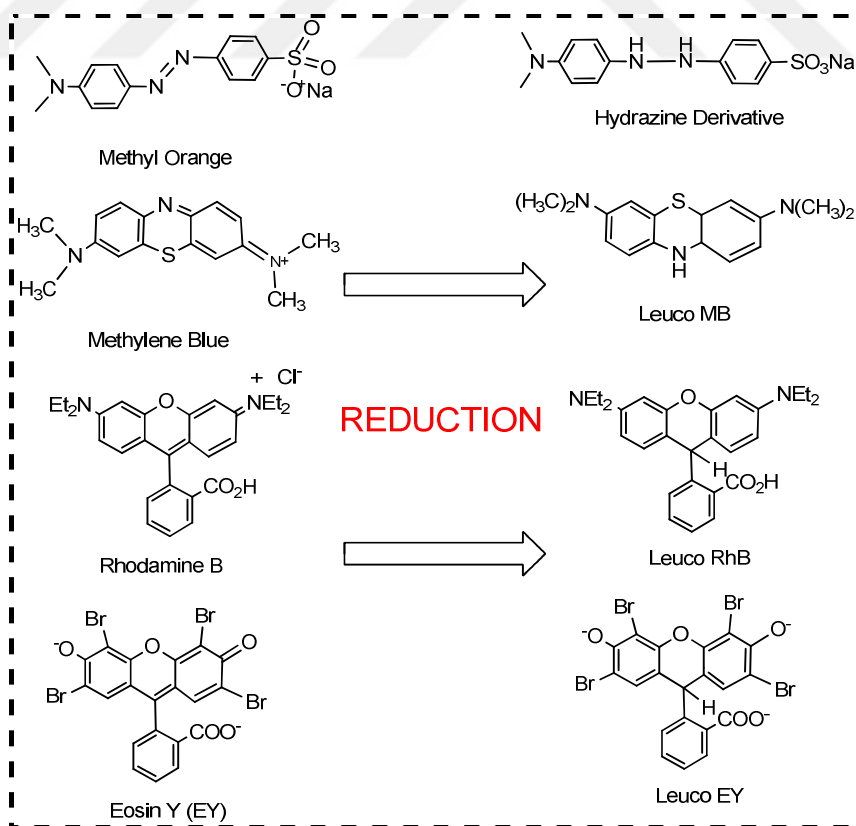
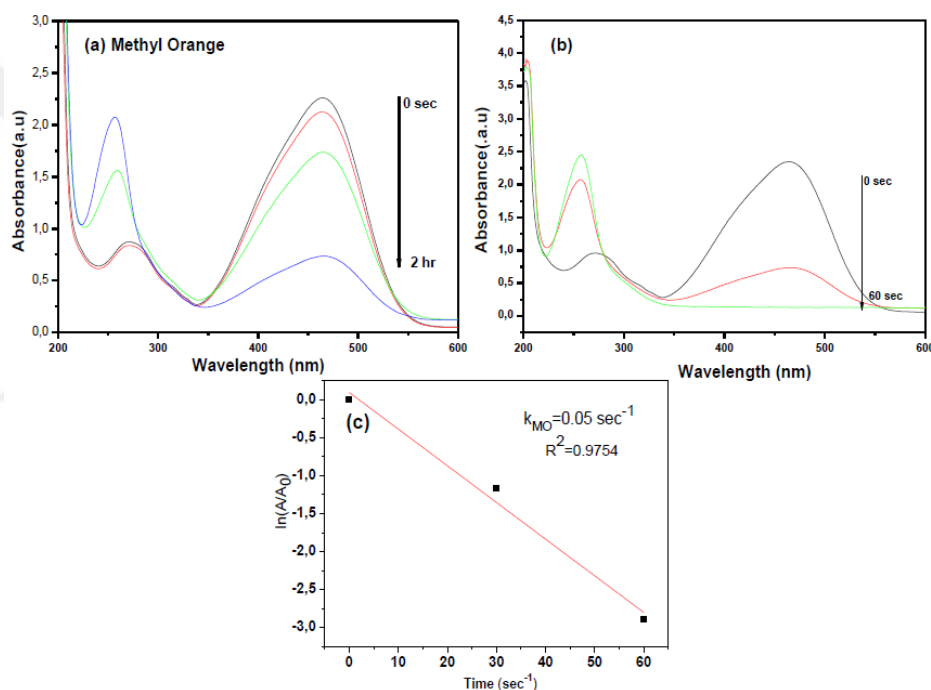


Figure 4.28: Azo dyes' leuco forms during reduction reactions (hydrazine derivative for MO).



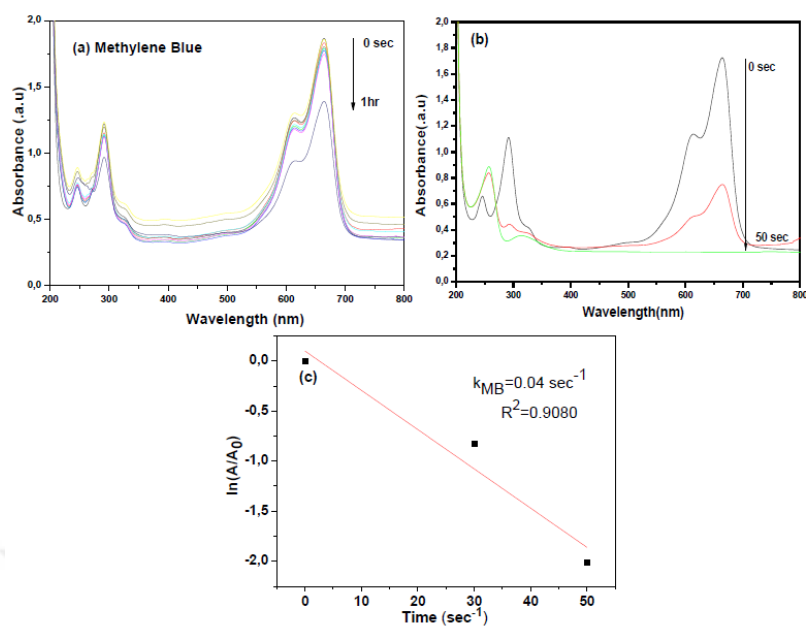
#### 4.1.5. Catalytic Tests of Fe<sub>3</sub>O<sub>4</sub>@Nico@Cu Magnetic Nanocatalysts

The catalytic performance of Fe<sub>3</sub>O<sub>4</sub>@Nico-Cu magnetic hybrid for a variety of azo dyes reduction was analyzed as seen in Figure 4.29. Firstly, partial reduction was observed in the existence of only sodiumborohydride and the peak intensity at 465 nm reduced even after 2h (Figure 4.29a). The intensity at 465 nm went to zero only 60 sec with the help of Fe<sub>3</sub>O<sub>4</sub>@Nico-Cu magnetic hybrid meanwhile a new absorption at 245 nm confirmed that complete reduction was achieved (Figure 4.29b).



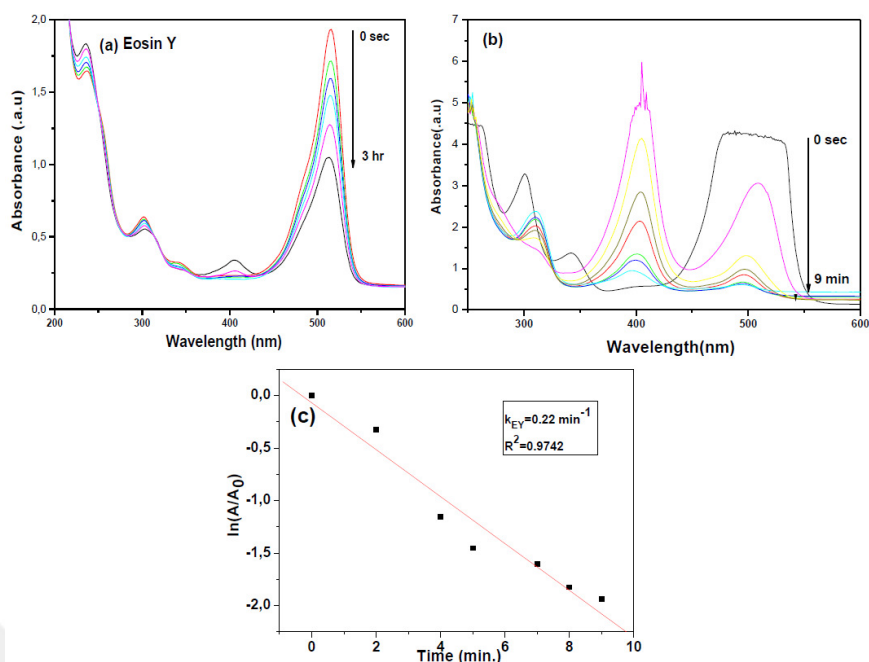
**Figure 4.29:**(a) Absorption spectra for the MO in the existence of only NaBH<sub>4</sub>, (b) upon addition of magnetic nanocatalyst and (c) The slope of straight line of ln (A<sub>t</sub>/A<sub>0</sub>) vs. reaction time for MO dye reduction.

Figure 4.30 showed that no significant changes were observed implying that MB dye reduction was not successful in the existence of only sodium borohydride (Figure 4.30a). However, the typical intensity for MB at 650 nm decreased within only 50 sec after addition of the catalyst (Figure 4.30b). This result demonstrated that the MB reduction was successful because of the catalytically active Cu NPs in the as-synthesized product.



**Figure 4.30:**(a) Absorbance for MB dye in the existence only  $\text{NaBH}_4$ , (b) upon addition of prepared magnetic nanocatalyst (c) The slope of straight line of  $\ln(A_t/A_0)$  vs. time for MB dye degradation.

Eosin Y had the peak intensity at 510 nm and the reduction was not completed even after 3h by only  $\text{NaBH}_4$  (Figure 4.31a). But the signal at 510 nm peak gradually decreased in 9 min after the addition small amount of  $\text{Fe}_3\text{O}_4@\text{Nico}@\text{Cu}$  nanocatalyst (Figure 4.31b).



**Figure 4.31:** Absorption spectra for the degradation of eosin Y dye (a) in the existence of only sodium borohydride, (b) upon addition of prepared magnetic nanocatalyst and (c) The slope of straight line of  $\ln(A_t/A_0)$  vs. reaction time for EY dye reduction.

As a final dye, RhB was tested and the main peak was unchanged when the time proceeds in the existence of only sodium borohydride (Figure 4.32a). But, its reduction happened only 2 min with the help of  $\text{Fe}_3\text{O}_4@\text{Nico}@\text{Cu}$  nanocatalyst (Figure 4.32b).

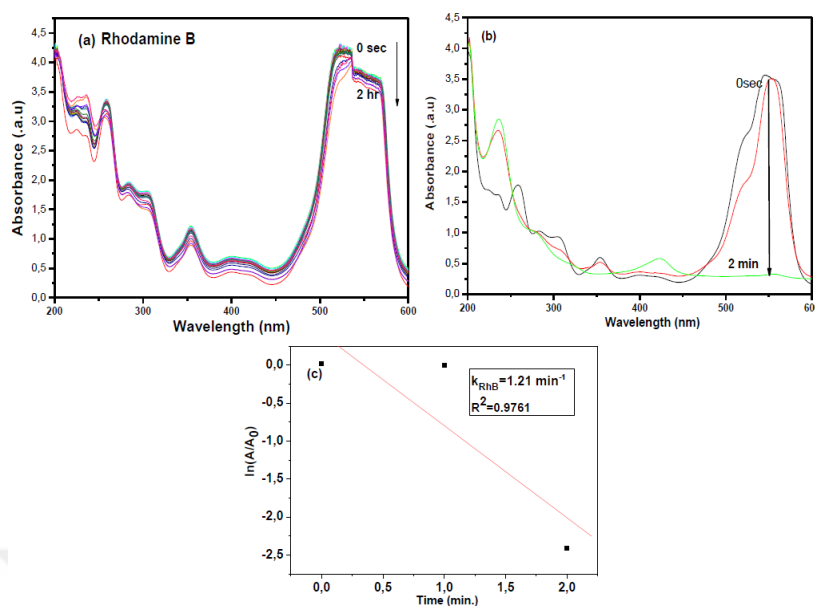


**Figure 4.32:** Absorption spectra of RhB for only (a) sodium borohydride, (b) upon addition of prepared magnetic nanocatalyst and (c) The slope of straight line of  $\ln(A_t/A_0)$  vs. time for RhB dye reduction.

The reaction kinetics were calculated to be  $0.05$  and  $0.04 \text{ s}^{-1}$  for MO and MB, respectively (Figure 4.29c and 30c). The value of apparent rate constants for EY and RhB were calculated to be  $1.21$  and  $0.22 \text{ min}^{-1}$ , respectively (Figure 4.31c and 32c). Compared with other magnetic nanocatalyst in the literature,  $\text{Fe}_3\text{O}_4@\text{Nico}@\text{Cu}$  displayed good catalytic performance [51, 70, 71, 82, 83]. The reuse and stability of  $\text{Fe}_3\text{O}_4@\text{Nico}-\text{Cu}$  nanocatalyst were studied to see the cost-effectiveness of the method and this was performed in a very simple way. After MO reduction, Cu loaded magnetic  $\text{Fe}_3\text{O}_4@\text{Nico}$  materials were collected by a magnetic filtration. Then, it was recycled and repeated for the reduction. By using the  $\text{Fe}_3\text{O}_4@\text{Nico}@\text{Cu}$  magnetic nanocatalysts for five times, the reduction of MO had almost the same catalytic performance. The color change of the each azo dye and easy separation of it were also shown in Figure 4.33. All these results confirmed that the  $\text{Fe}_3\text{O}_4@\text{Nico}@\text{Cu}$  nanocatalysts were not corroded during dye reduction.



**Figure 4.33:** Photo that illustrates color change of azo dyes after catalysis reaction and easy separation of it by a magnet.

#### 4.1.6. Catalytic Tests of $\text{MnFe}_2\text{O}_4$ @PANI-Ag Magnetic Nanocatalysts

As seen in Figure 4.34a, MO aqueous solution has a maximum UV-vis absorption ( $A_{\text{max}}$ ) at 465 nm and its partial reduction took more than 24 h in the presence of  $\text{NaBH}_4$  only but a sharp decrease in the  $A_{\text{max}}$  intensity was completed within 9 min and the solution changed to the colorless (Figure 4.34b).

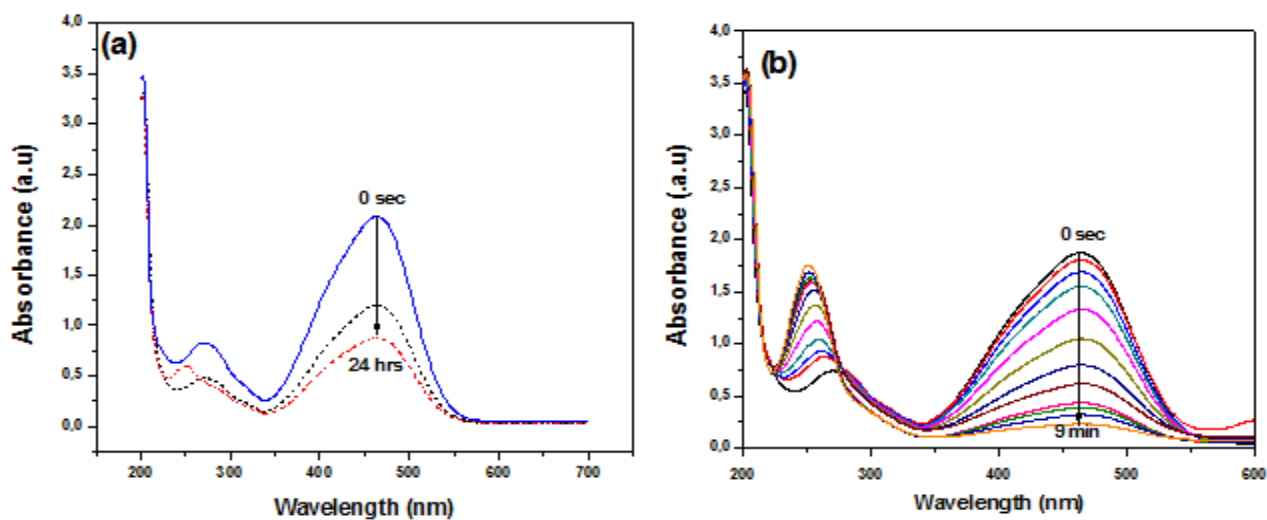


**Figure 4.34:** Absorbance of (a) MO dye by only  $\text{NaBH}_4$  and (b) upon addition of  $\text{MnFe}_2\text{O}_4@\text{PANI-Ag}$  nanocatalyst in the presence of  $\text{NaBH}_4$ .

Here, we have investigated the application of Ag loaded magnetic  $\text{MnFe}_2\text{O}_4@\text{PANI}$  nanocomposite for the degradation of methyl blue. It had a maximum absorption ( $A_{\text{max}}$ ) at 665 nm. The whole decolorization process did not occur even after 3h (Figure 4.35a). However, the absorbance at 665 nm vanished after addition of  $\text{MnFe}_2\text{O}_4@\text{PANI-Ag}$  nanocatalyst within 16 min (Figure 4.35b).

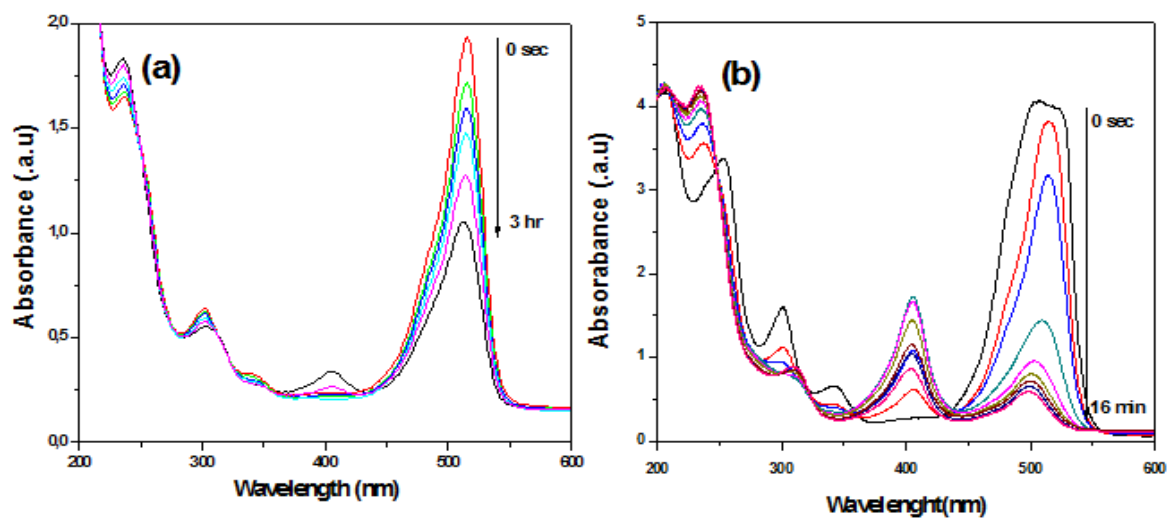


**Figure 4.35:** Absorbance of MB (a) in the presence of only NaBH<sub>4</sub> and (b) after immediate addition of MnFe<sub>2</sub>O<sub>4</sub>@PANI-Ag nanocatalyst in the existence of NaBH<sub>4</sub>.

As seen in Fig. 4.36a and 4.36b, the color of the solutions with large excess of NaBH<sub>4</sub> changed for 3h and 2h for EY and RhB, respectively, which confirmed that the rate of catalytic reaction was so slow. However, after addition of the MnFe<sub>2</sub>O<sub>4</sub>@PANI-Ag nanocatalyst, the color of EY and RhB solution disappeared within 16 and 23 min, respectively, demonstrating the catalytic reduction of EY proceeded faster than RhB (Fig. 4.36c and Fig. 4.36d).

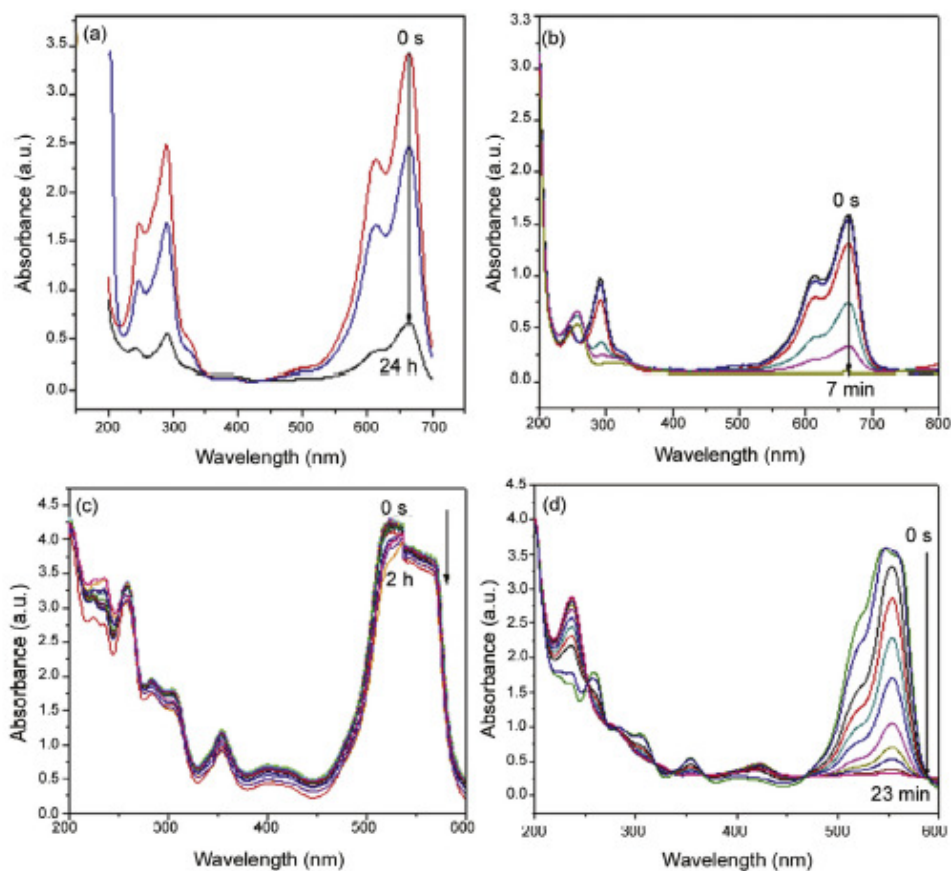


**Figure 4.36:** Absorbance of (a) EY in the presence of only  $\text{NaBH}_4$  and (b) upon addition of  $\text{MnFe}_2\text{O}_4@\text{PANI-Ag}$ , (c) RhB by only  $\text{NaBH}_4$  and (d) after immediate addition of  $\text{MnFe}_2\text{O}_4@\text{PANI-Ag}$  nanocatalyst.

The rate constants of MB, MO, EY and RhB reduction were found to be 0.61, 0.22, 0.14 and  $0.11 \text{ min}^{-1}$ , respectively (Figure 4.37). The  $\text{MnFe}_2\text{O}_4@\text{PANI-Ag}$  nanocatalyst presented the highest catalytic activity MB dye reduction while the lowest activity for RhB dye reduction. The reusability is another important factor for any recoverable magnetic nanocatalysts, was also investigated here. As seen in Figure 4.38,  $k$  value decreased after 4 runs demonstrating that catalytic activity was decreased as cycling continued.



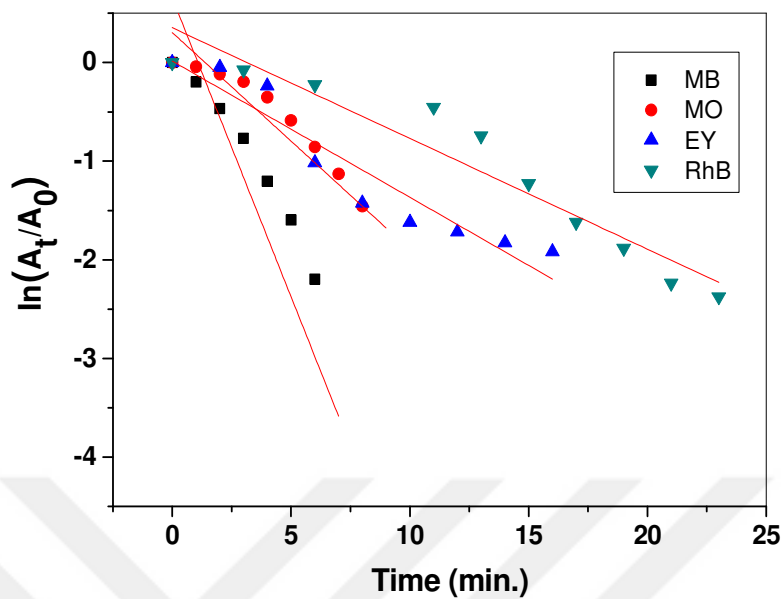


**Figure 4.37:** The slope of straight line of  $\ln(A_t/A_0)$  vs. reaction time for various azo dyes reduction.

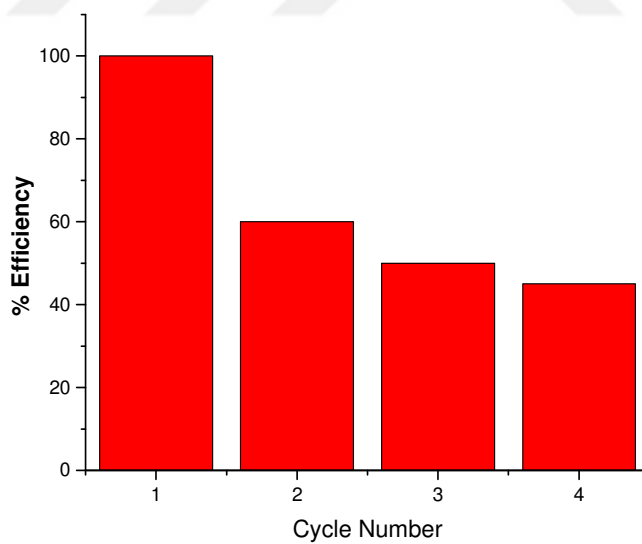


**Figure 4.38:** The catalytic performance of the  $\text{MnFe}_2\text{O}_4@PANI\text{-Ag}$  nanocatalyst in different cycling numbers.

#### 4.1.7. Catalytic Tests of MnFe<sub>2</sub>O<sub>4</sub>@SiO<sub>2</sub>-Ag Magnetic Hybrid

##### 4.1.7.1. Azo dyes reduction

As shown in Fig. 4.39, MnFe<sub>2</sub>O<sub>4</sub>@SiO<sub>2</sub>-Ag nanocatalyst caused that different reduction reactions took place at different times. The  $k$  values for degradation of methyl orange and rhodamine B were 0.04 and 0.02 sec<sup>-1</sup>, respectively. In addition, the other rate constants are for EY and MB were 0.17 and 0.15 min<sup>-1</sup>, respectively. These values were better than literature values[42,43].

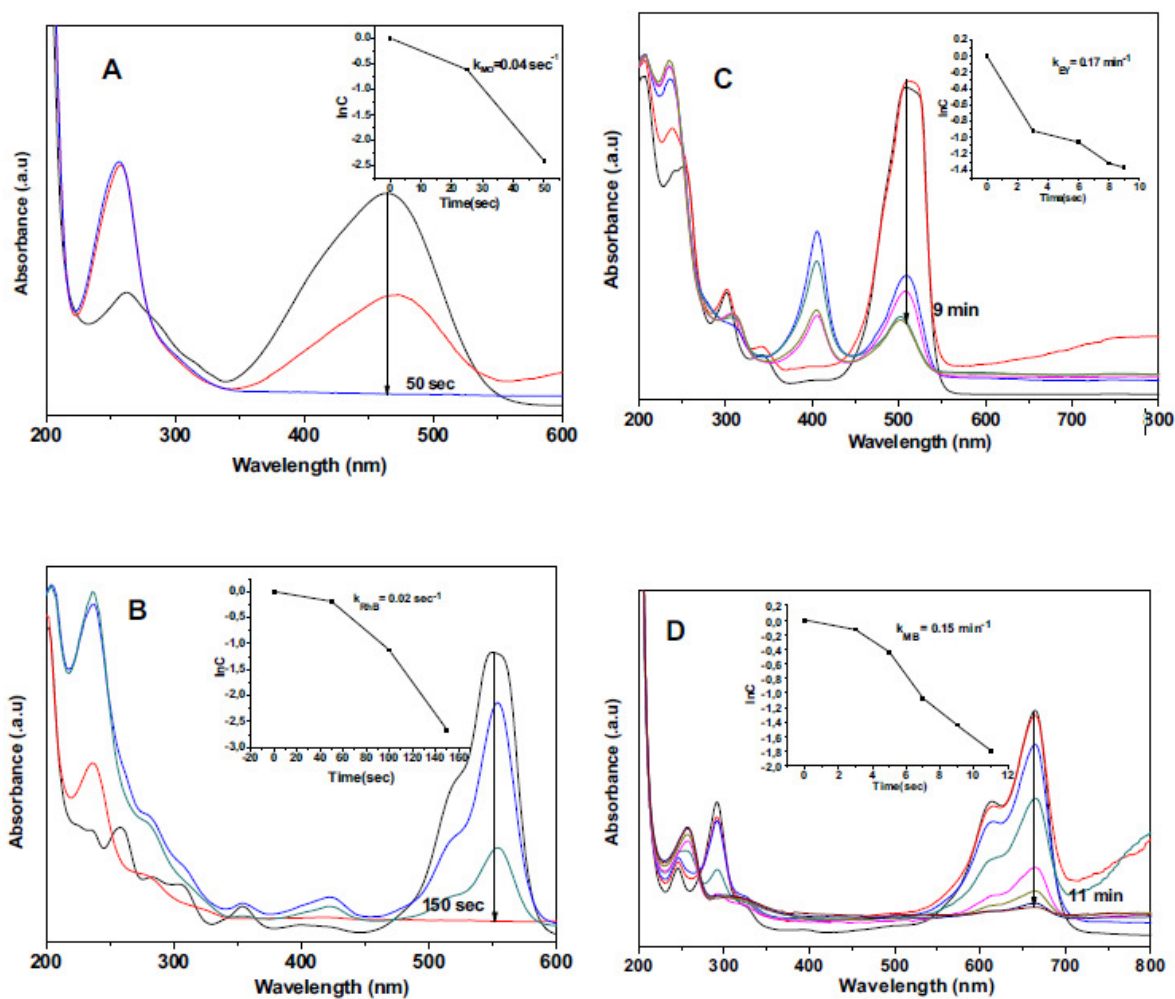
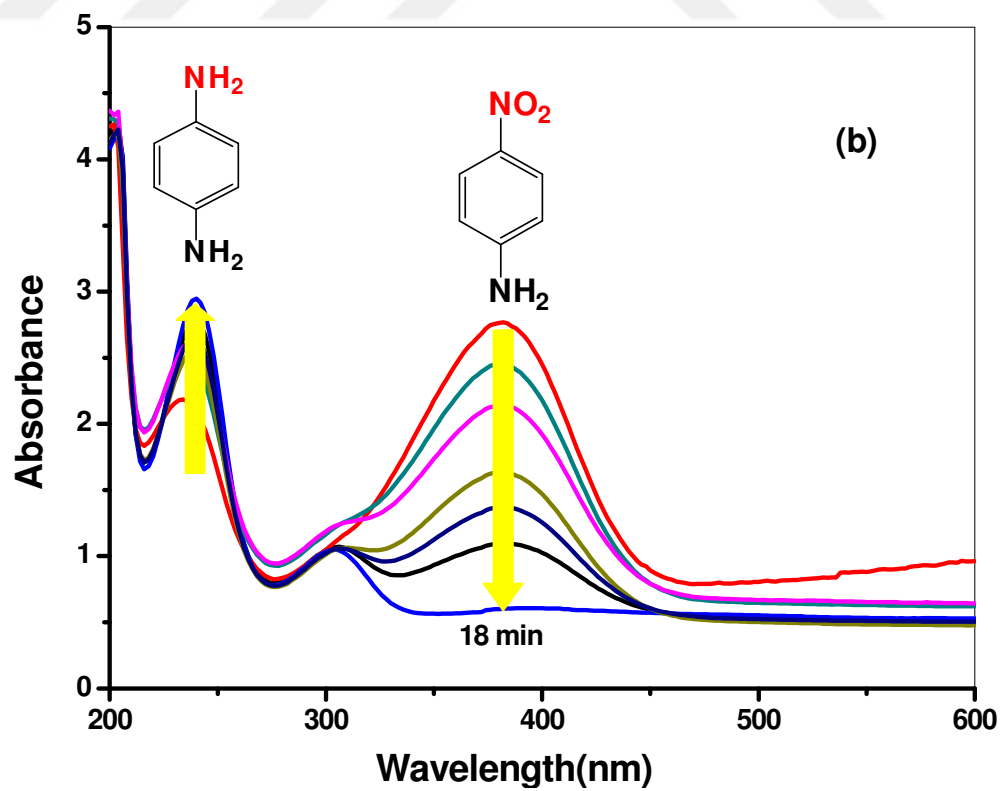
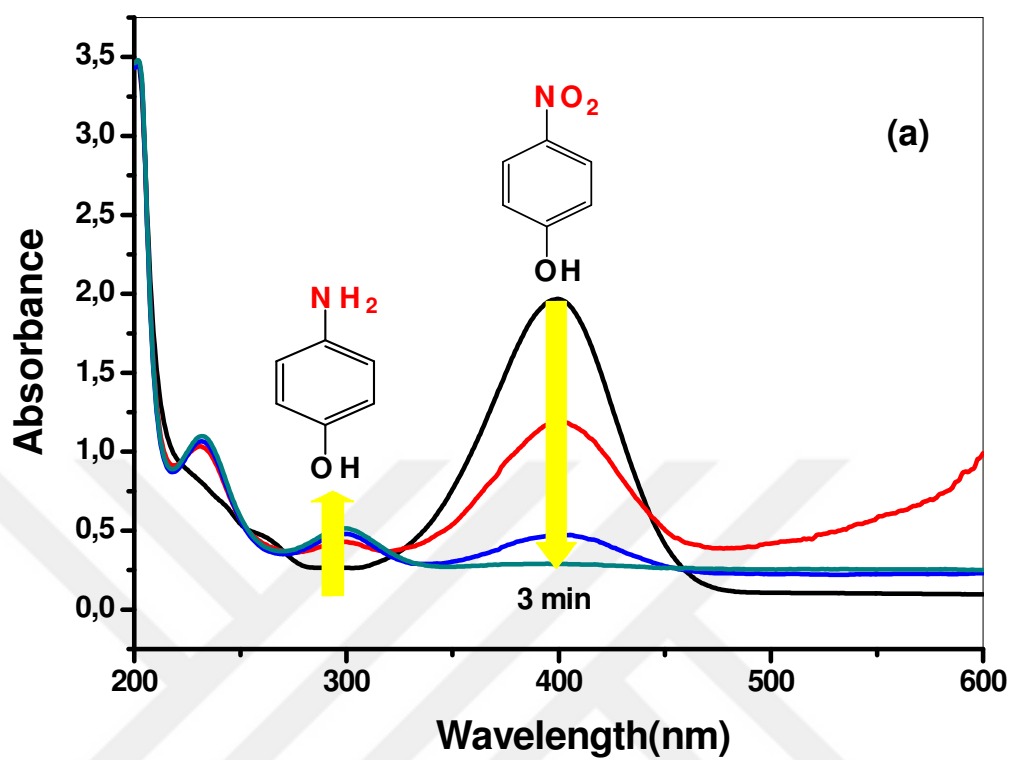


**Figure 4.39:** Absorption spectra for the reduction process of (a) MO, (b) RhB (c) EY and (d) MB solution after immediate addition of MnFe<sub>2</sub>O<sub>4</sub>@SiO<sub>2</sub>-Ag nanocatalyst in the presence of NaBH<sub>4</sub>.

When it comes to nitro compounds' reactions results, the maximum intensity at 400 nm disappeared because of the formation of phenolate ions and it turned to clear slowly (Fig. 4.40). In addition, the catalytic reduction reaction was completed within 18 min for 4-nitroaniline and 6 min for 2-nitroaniline, respectively (Fig. 4.40a and 4.40b). According to the kinetic results, the rate constants were estimated to be as 0.66, 0.09 and 0.11  $\text{min}^{-1}$  for 4-nitrophenol, 4-nitroaniline, 2-nitroaniline, respectively (Figure 4.41). They were shown in Table 3. Compared of the literature values, these results were better than other catalysts [44-49].

**Table 4.3:** Reduction time and rates of various compounds by  $\text{MnFe}_2\text{O}_4@\text{SiO}_2\text{-Ag}$  catalyzed reactions.

Azo Dye	Reaction time	Rate constant	Correlation Coefficient
MO	50 sec.	0.04 $\text{sec}^{-1}$	0.9109
RhB	150 sec.	0.02 $\text{sec}^{-1}$	0.8588
EY	9 min.	0.17 $\text{min}^{-1}$	0.8413
MB	11 min.	0.15 $\text{min}^{-1}$	0.9154
4-NP	3 min.	0.65 $\text{min}^{-1}$	0.9811
4-NA	18 min.	0.08 $\text{min}^{-1}$	0.9377
2-NA	6 min.	0.12 $\text{min}^{-1}$	0.8706



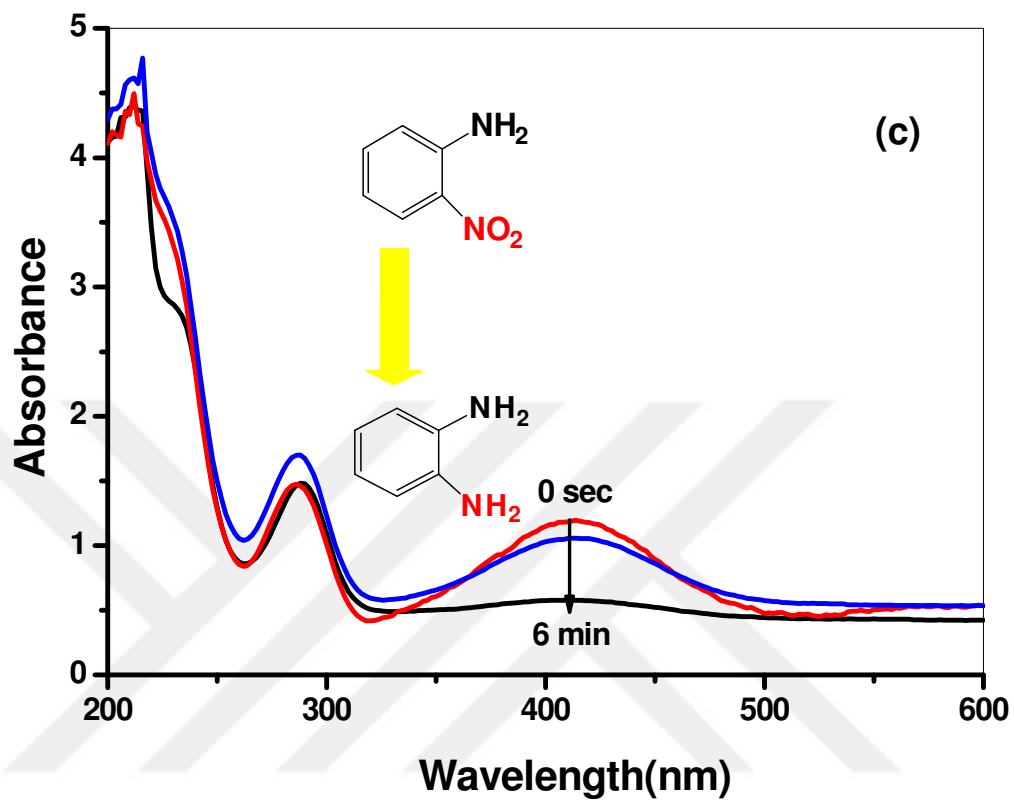


**Figure 4.40:** Absorbance of (a) 4-NP, (b) 4-NA and (c) 2-NA solution after immediate addition of  $\text{MnFe}_2\text{O}_4@\text{SiO}_2\text{-Ag}$  nanocatalyst in the presence of  $\text{NaBH}_4$ .

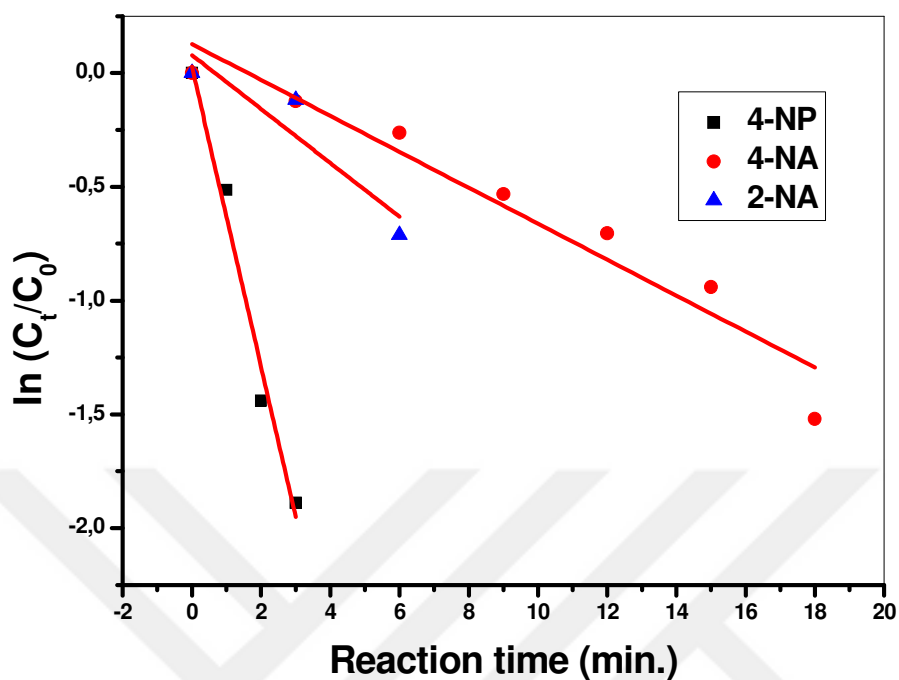


**Figure 4.41:** The first order kinetic plot of various aromatic compounds reduction using magnetic  $\text{MnFe}_2\text{O}_4@\text{SiO}_2\text{-Ag}$  as nanocatalyst.

Magnetic recyclability of  $\text{MnFe}_2\text{O}_4@\text{SiO}_2\text{-Ag}$  nanocatalyst was also carried out. Figure 4.42 showed the conversion of the prepared material for the reduction of MO and MB. As shown in Fig. 4.42, the conversion decreased little after four cycles and the catalyst showed similar catalytic performance when cycling continued.

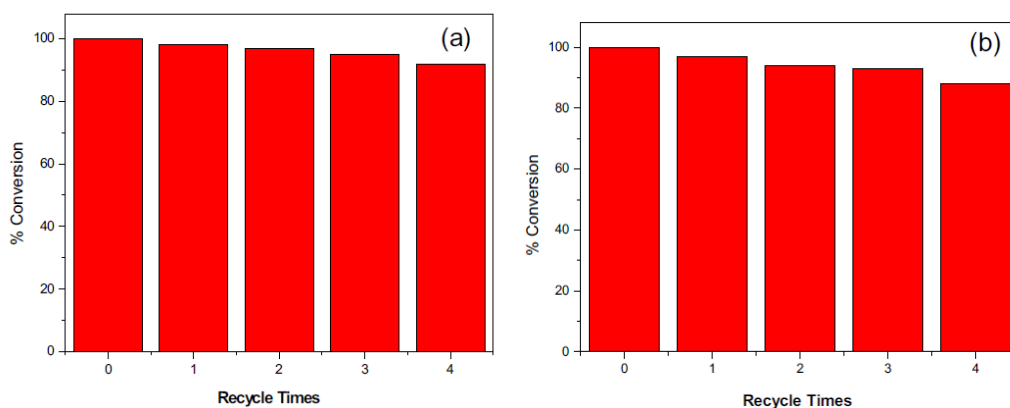


**Figure 4.42:** Recycling of  $\text{MnFe}_2\text{O}_4@\text{SiO}_2\text{-Ag}$  nanocatalyst for the reduction of (a) MO and (b) MB dye in the presence of  $\text{NaBH}_4$ .

#### 4.1.8. Catalytic Tests of $\text{Fe}_3\text{O}_4@\text{PAMAM}(\text{G}1)\text{-Ag}$ Magnetic Hybrid

The catalytic performance of the  $\text{Fe}_3\text{O}_4@\text{PAMAM}(\text{G}1)\text{-Ag}$  was examined by using the catalytic reduction of 4-nitrophenol to 4-aminophenol. This process was monitored by observing the intensity of the absorption peak at 400 nm incorporated with 4-NP (Figure 4.43). Upon addition of the  $\text{Fe}_3\text{O}_4@\text{PAMAM}(\text{G}1)\text{-Ag}$  magnetic hybrid, the maximum intensity disappeared along with the reaction time and a new absorbance peak at 300 nm appeared within 3 minutes due to the formation of 4-aminophenol as shown in Figure 4.44 [84].

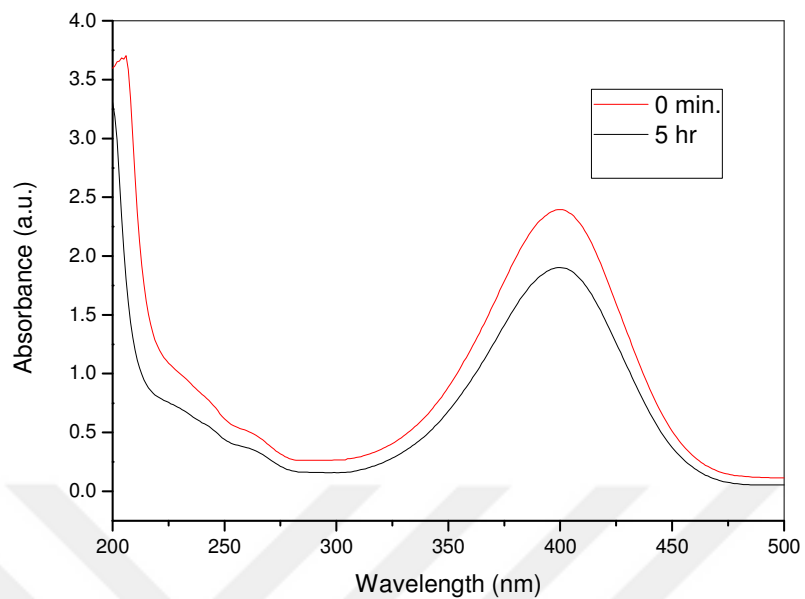


**Figure 4.43:**UV-Vis absorption spectra of the 4-NP mixture in NaBH<sub>4</sub> solution only.

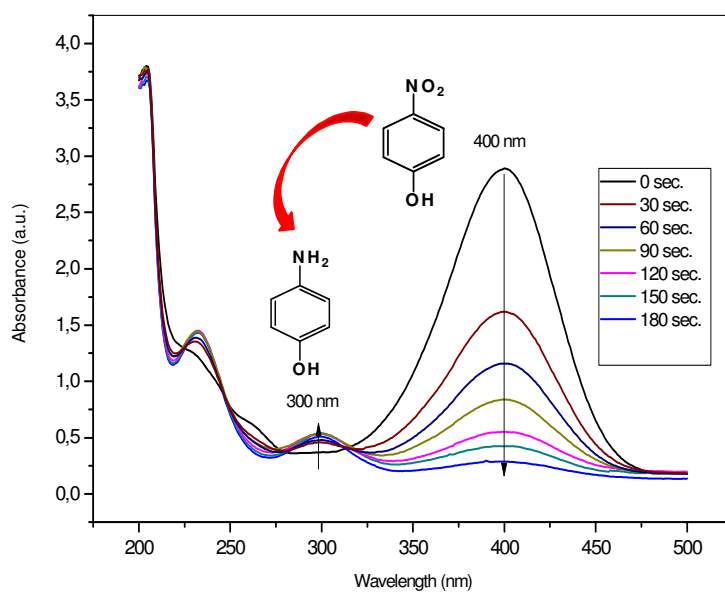


**Figure 4.44:**UV-Vis absorption spectra for the reduction of 4-NP in the presence of Fe<sub>3</sub>O<sub>4</sub>@PAMAM(G1)-Ag magnetic nanocatalyst.



From the linear relationship of  $\ln(C_t/C_0)$  and  $t$ , the rate constant ( $k$ ) of 4-nitrophenol was estimated which was better than similar studies [84, 85]. In addition, the rate constant  $k$  of the prepared material was much higher than reported values in literature [86, 87]. The color change of 4-nitrophenol with the help of  $\text{Fe}_3\text{O}_4@\text{PAMAM}(\text{G}1)\text{-Ag}$  magnetic nanocatalyst after reduction reaction was given in Figure 4.45b.

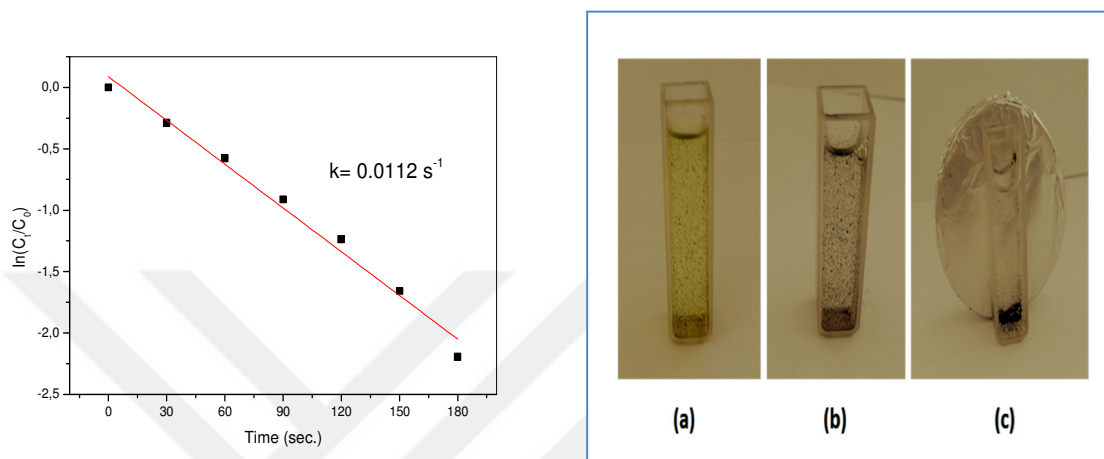


**Figure 4.45:** (a) First order kinetic plot and (b) the color changes of 4-NP and the recyclability of the catalyst after complete reaction.

## 5. CONCLUSION AND RECOMMENDATIONS

In this thesis, we have presented new magnetically recyclable nanocomposites of different core like  $\text{Fe}_3\text{O}_4$  and  $\text{MnFe}_2\text{O}_4$  and coating layers such as histidine, nicotinic acid, polyaniline, Tween20 or silica. They have been fabricated by various techniques and were investigated for their characteristics. The catalytic performance of all the prepared magnetic hybrids was tested on a series of dyes and nitroaromatic compounds.

$\text{Fe}_3\text{O}_4$ @Tween20-Ag nanocatalyst has been successfully produced by thermal decomposition route, where Tween20 was used as a linker between magnetic core and Ag NPs and then it was applied as magnetic nanocatalyst in order to reduce for different azo dyes which are harmful to environment. Obtained results have shown that  $\text{Fe}_3\text{O}_4$ @Tween20-Ag nanocatalyst showed high catalytic performance up to five cycles with a little loss of activity.

Highly effective Ag incorporated newly  $\text{MnFe}_2\text{O}_4$ @ $\text{SiO}_2$  and  $\text{MnFe}_2\text{O}_4$ @PANI magnetic hybrids were successfully synthesized with a combination of thermal reduction technique. This method prevented the aggregation of Ag NPs on the surface of magnetic nanocomposite.  $\text{MnFe}_2\text{O}_4$  was used as magnetic core and polyaniline (PANI) was the stabilizer. The structural result showed that the products were in small size with a good dispersion. They were used as magnetic nanocatalyst to reduce a wide variety of azo dyes and aromatic nitro compounds including 4-nitrophenol, 4-nitroaniline and 2-nitroaniline in the existence of  $\text{NaBH}_4$ . The high activity of  $\text{MnFe}_2\text{O}_4$ @ $\text{SiO}_2$ @Ag magnetic hybrid obtained for methyl orange reduction among the azo dyes group and for 4-NP in the aromatic nitro compounds.

Incorporating the individual advantages of Ag or Cu and  $\text{Fe}_3\text{O}_4$ ,  $\text{Fe}_3\text{O}_4$ @His@Cu and  $\text{Fe}_3\text{O}_4$ @His@Ag were also generated for decolorization of dye pollutants. The as-prepared magnetic hybrids showed many advantages like monodispersity and simplicity and used as a high performance catalyst for the reduction of a series of azo dyes. Furthermore, they could be recycled with magnetic filtration.

In order to fabricate a uniform and stable around magnetic core,  $\text{Fe}_3\text{O}_4$ , polyamidoamine dendrimer was also used on the surface of magnetic nanoparticles. Then, highly dispersed Ag NPs was doped to the layers of dendrimers and as magnetically recyclable nanocatalyst,  $\text{Fe}_3\text{O}_4$ @PAMAM (G1)-Ag was obtained with a low crystallite size. Additionally, it was tested

for the catalytic behaviour against 4-NP and the catalytic efficiency did not change after 5 cycles.

In summary, we have demonstrated an easy and effective route to prepare a series of magnetically recyclable nanocatalysts. All the fabricated magnetic hybrids had the crystalline structure with a narrow size distribution and showed very high catalytic activity for the reduction of various dyes and nitro compounds due to their strong electrostatic attraction. The kinetics studies also proved that the reduction process obeyed the pseudo-first-order kinetics model. In addition, the prepared magnetic hybrids can be easily removed from the medium by a magnet and thus they are the potential adsorbents for environmental applications.



## REFERENCES

1. Shabani I, Haddadi-Asl V, Seyedjafari E, Babaeijandaghi F, Soleimani M 2009. Improved infiltration of stem cells on electrospun nanofibers. *Biochemical and biophysical research communications* 382(1):129-133.
2. Shabani I, Haddadi-Asl V, Soleimani M, Seyedjafari E, Babaeijandaghi F, Ahmadbeigi N 2011. Enhanced infiltration and biomineralization of stem cells on collagen-grafted three-dimensional nanofibers. *Tissue Engineering Part A* 17(9-10):1209-1218.
3. Saba N, Jawaid M, Asim M. 2016. Recent advances in nanoclay/natural fibers hybrid composites. *Nanoclay reinforced polymer composites*, ed.: Springer. p 1-28.
4. Babaei I, Madanipour M, Farsi M, Farajpoor A 2014. Physical and mechanical properties of foamed HDPE/wheat straw flour/nanoclay hybrid composite. *Composites Part B: Engineering* 56:163-170.
5. J O'Loughlin E, A Gorski C, M Scherer M 2015. Effects of phosphate on secondary mineral formation during the bioreduction of akaganeite ( $\beta$ -FeOOH): Green rust versus framboidal magnetite. *Current Inorganic Chemistry* 5(3):214-224.
6. Eremin A, Gurentsov E, Mikheyeva EY, Musikhin S. *Journal of Physics: Conference Series*, 2016, pp 012127.
7. Cabrera L, Gutierrez S, Menendez N, Morales M, Herrasti P 2008. Magnetite nanoparticles: electrochemical synthesis and characterization. *Electrochimica Acta* 53(8):3436-3441.
8. Umut E. 2013. Surface modification of nanoparticles used in biomedical applications. *Modern Surface Engineering Treatments*, ed.: InTech.
9. Teja AS, Koh P-Y 2009. Synthesis, properties, and applications of magnetic iron oxide nanoparticles. *Progress in crystal growth and characterization of materials* 55(1-2):22-45.
10. Laurent S, Forge D, Port M, Roch A, Robic C, Vander Elst L, Muller RN 2008. Magnetic iron oxide nanoparticles: synthesis, stabilization, vectorization, physicochemical characterizations, and biological applications. *Chemical reviews* 108(6):2064-2110.
11. Sui R, Charpentier P 2012. Synthesis of metal oxide nanostructures by direct sol-gel chemistry in supercritical fluids. *Chemical reviews* 112(6):3057-3082.
12. Yang S, Chen L, Mu L, Ma P-C 2014. Magnetic graphene foam for efficient adsorption of oil and organic solvents. *Journal of colloid and interface science* 430:337-344.
13. Flores JA, Pavía-Sanders A, Chen Y, Pochan DJ, Wooley KL 2015. Recyclable hybrid inorganic/organic magnetically active networks for the sequestration of crude oil from aqueous environments. *Chemistry of Materials* 27(10):3775-3782.
14. Zhou L, Gao C, Xu W 2010. Magnetic dendritic materials for highly efficient adsorption of dyes and drugs. *ACS applied materials & interfaces* 2(5):1483-1491.
15. Cheng Z, Liao J, He B, Zhang F, Zhang F, Huang X, Zhou L 2015. One-step fabrication of graphene oxide enhanced magnetic composite gel for highly efficient dye adsorption and catalysis. *ACS Sustainable Chemistry & Engineering* 3(7):1677-1685.
16. Asmatulu R, Zalich MA, Claus RO, Riffle JS 2005. Synthesis, characterization and targeting of biodegradable magnetic nanocomposite particles by external magnetic fields. *Journal of Magnetism and Magnetic Materials* 292:108-119.

17. Ke F, Yuan Y-P, Qiu L-G, Shen Y-H, Xie A-J, Zhu J-F, Tian X-Y, Zhang L-D 2011. Facile fabrication of magnetic metal–organic framework nanocomposites for potential targeted drug delivery. *Journal of Materials Chemistry* 21(11):3843-3848.
18. Izydorzak-Wozniak M, Leonowicz M 2014. Carbon Matrix Based Magnetic Nanocomposites for Potential Biomedical Applications. *Journal of nanoscience and nanotechnology* 14(3):2258-2267.
19. Yi DK, Lee SS, Papaefthymiou GC, Ying JY 2006. Nanoparticle architectures templated by SiO<sub>2</sub>/Fe<sub>2</sub>O<sub>3</sub> nanocomposites. *Chemistry of Materials* 18(3):614-619.
20. Lin Y, Qiao Y, Wang Y, Yan Y, Huang J 2012. Self-assembled laminated nanoribbon-directed synthesis of noble metallic nanoparticle-decorated silica nanotubes and their catalytic applications. *Journal of Materials Chemistry* 22(35):18314-18320.
21. Stöber W, Fink A, Bohn E 1968. Controlled growth of monodisperse silica spheres in the micron size range. *Journal of colloid and interface science* 26(1):62-69.
22. Philipse AP, Van Bruggen MP, Pathmamanoharan C 1994. Magnetic silica dispersions: preparation and stability of surface-modified silica particles with a magnetic core. *Langmuir* 10(1):92-99.
23. Karimi AR, Dalirnasab Z, Karimi M, Bagherian F 2013. Sulfuric acid functionalized silica-coated magnetic nanoparticles: Preparation and application in synthesis of mono-, di- and tri [bis (6-aminopyrimidinyl) methanes]. *Synthesis* 45(23):3300-3304.
24. Chang Y-C, Chen D-H 2005. Preparation and adsorption properties of monodisperse chitosan-bound Fe<sub>3</sub>O<sub>4</sub> magnetic nanoparticles for removal of Cu (II) ions. *Journal of Colloid and Interface Science* 283(2):446-451.
25. Zhi J, Wang Y, Lu Y, Ma J, Luo G 2006. In situ preparation of magnetic chitosan/Fe<sub>3</sub>O<sub>4</sub> composite nanoparticles in tiny pools of water-in-oil microemulsion. *Reactive and Functional Polymers* 66(12):1552-1558.
26. Crabtree RH. 2009. *Green Catalysis*. ed.: Wiley-VCH.
27. Niemantsverdriet J. 2006. *Concepts of modern catalysis and kinetics*. ed.: John Wiley & Sons.
28. Zhang Y, Liu S, Lu W, Wang L, Tian J and Sun X 2011 In situ green synthesis of Au nanostructures on graphene oxide and their application for catalytic reduction of 4-nitrophenol *Catal. Sci. Technol.* 1 1142–4
29. Daniel M C and Astruc D 2004 Gold nanoparticles: assembly, supramolecular chemistry, quantum-size-related properties, and applications toward biology, catalysis, and nanotechnology *Chem. Rev.* 104 293–346
30. Zhou L, Gao C, Xu W 2010. Robust Fe<sub>3</sub>O<sub>4</sub>/SiO<sub>2</sub>-Pt/Au/Pd magnetic nanocatalysts with multifunctional hyperbranched polyglycerol amplifiers. *Langmuir* 26(13):11217-11225.
31. Ge J, Huynh T, Hu Y, Yin Y 2008. Hierarchical magnetite/silica nanoassemblies as magnetically recoverable catalyst–supports. *Nano letters* 8(3):931-934.
32. Lijuan S, Jiang H, Songsong A, ZHANG J, ZHENG J, Dong R 2013. Recyclable Fe<sub>3</sub>O<sub>4</sub>@SiO<sub>2</sub>-Ag magnetic nanospheres for the rapid decolorizing of dye pollutants. *Chinese Journal of Catalysis* 34(7):1378-1385.
33. Carvalho M, Pereira C, Goncalves I, Pinheiro H, Santos A, Lopes A, Ferra M 2008. Assessment of the biodegradability of a monosulfonated azo dye and aromatic amines. *International Biodeterioration & Biodegradation* 62(2):96-103.
34. Uddin MT, Islam MA, Mahmud S, Rukanuzzaman M 2009. Adsorptive removal of methylene blue by tea waste. *Journal of Hazardous Materials* 164(1):53-60.

35. Zhao L, Chen X, Wang X, Zhang Y, Wei W, Sun Y, Antonietti M, Titirici MM 2010. One-step solvothermal synthesis of a carbon@TiO<sub>2</sub> dye structure effectively promoting visible-light photocatalysis. *Advanced Materials* 22(30):3317-3321.
36. Zhang, C.; Wu, L.; Cai, D.; Zhang, C.; Wang, N.; Zhang, J.; Wu, Z. Adsorption of polycyclic aromatic hydrocarbons (fluoranthene and anthracene-methanol) by functional graphene oxide and removal by pH and temperature-sensitive coagulation. *ACS Appl. Mater. Interfaces* 2013, 5, 4783–4790
37. Shi B, Li G, Wang D, Feng C, Tang H 2007. Removal of direct dyes by coagulation: The performance of preformed polymeric aluminum species. *Journal of Hazardous Materials* 143(1-2):567-574.
38. Lee J-W, Choi S-P, Thiruvenkatachari R, Shim W-G, Moon H 2006. Submerged microfiltration membrane coupled with alum coagulation/powdered activated carbon adsorption for complete decolorization of reactive dyes. *Water research* 40(3):435-444.
39. Pan B-f, Gao F, Gu H-c 2005. Dendrimer modified magnetite nanoparticles for protein immobilization. *Journal of colloid and interface science* 284(1):1-6.
40. Liu H, Guo J, Jin L, Yang W, Wang C 2008. Fabrication and functionalization of dendritic poly (amidoamine)-immobilized magnetic polymer composite microspheres. *The Journal of Physical Chemistry B* 112(11):3315-3321.
41. Demir A, Baykal A, Sözeri H, Topkaya R 2014. Low temperature magnetic investigation of Fe<sub>3</sub>O<sub>4</sub> nanoparticles filled into multiwalled carbon nanotubes. *Synthetic Metals* 187:75-80.
42. Kurtan U, Baykal A 2015. Fe<sub>3</sub>O<sub>4</sub>@Tween20@Ag Magnetically Recyclable Nanocatalyst for Various Hydrogenation Reactions. *Journal of Inorganic and Organometallic Polymers and Materials* 25(4):657-663.
43. Geng, Z.; Lin, Y.; Yu, X.; Shen, Q.; Ma, L.; Li, Z.; Pan, N.; Wang, X. Highly efficient dye adsorption and removal: A functional hybrid of reduced graphene oxide-Fe<sub>3</sub>O<sub>4</sub> nanoparticles as an easily regenerative adsorbent. *J. Mater. Chem.* 2012, 22, 3527–3535.
44. Ozkaya T, Toprak MS, Baykal A, Kavas H, Köseoğlu Y, Aktaş B 2009. Synthesis of Fe<sub>3</sub>O<sub>4</sub> nanoparticles at 100°C and its magnetic characterization. *Journal of Alloys and Compounds* 472(1):18-23.
45. Manikandan A, Vijaya JJ, Mary JA, Kennedy LJ, Dinesh A 2014. Structural, optical and magnetic properties of Fe<sub>3</sub>O<sub>4</sub> nanoparticles prepared by a facile microwave combustion method. *Journal of Industrial and Engineering Chemistry* 20(4):2077-2085.
46. Wang Y, Cao X, Liu G, Hong R, Chen Y, Chen X, Li H, Xu B, Wei D 2011. Synthesis of Fe<sub>3</sub>O<sub>4</sub> magnetic fluid used for magnetic resonance imaging and hyperthermia. *Journal of Magnetism and Magnetic Materials* 323(23):2953-2959.
47. Jadhav NV, Prasad AI, Kumar A, Mishra R, Dhara S, Babu K, Prajapat C, Misra N, Ningthoujam R, Pandey B 2013. Synthesis of oleic acid functionalized Fe<sub>3</sub>O<sub>4</sub> magnetic nanoparticles and studying their interaction with tumor cells for potential hyperthermia applications. *Colloids and Surfaces B: Biointerfaces* 108:158-168.
48. Yuan H, Wang Y, Zhou S-M, Lou S 2011. Fabrication of superparamagnetic Fe<sub>3</sub>O<sub>4</sub> hollow microspheres with a high saturation magnetization. *Chemical engineering journal* 175:555-560.
49. Karaoğlu E, Baykal A, Deligöz H, Şenel M, Sözeri H, Toprak MS 2011. Synthesis and characteristics of poly (3-pyrrol-1-ylpropanoic acid)(PPyAA)-Fe<sub>3</sub>O<sub>4</sub> nanocomposite. *Journal of Alloys and Compounds* 509(33):8460-8468.

50. Temizel E, Ayan E, Şenel M, Erdemi H, Yavuz MS, Kavas H, Baykal A, Öztürk R 2011. Synthesis, conductivity and magnetic properties of poly (N-pyrrole phosphonic acid)–Fe<sub>3</sub>O<sub>4</sub> nanocomposite. *Materials Chemistry and Physics* 131(1):284-291.
51. Tang M, Zhang S, Li X, Pang X, Qiu H 2014. Fabrication of magnetically recyclable Fe<sub>3</sub>O<sub>4</sub>@Cu nanocomposites with high catalytic performance for the reduction of organic dyes and 4-nitrophenol. *Materials Chemistry and Physics* 148(3):639-647.
52. Kurtan U, Amir M, Baykal A, Sözeri H, Toprak MS 2016. Magnetically Recyclable Fe<sub>3</sub>O<sub>4</sub>@His@Cu Nanocatalyst for Degradation of Azo Dyes. *Journal of nanoscience and nanotechnology* 16(3):2548-2556.
53. Han D, Wang J, Luo H 1994. Crystallite size effect on saturation magnetization of fine ferrimagnetic particles. *Journal of Magnetism and Magnetic Materials* 136(1):176-182.
54. Kodama RH, Berkowitz AE, McNiff Jr E, Foner S 1996. Surface spin disorder in NiFe<sub>2</sub>O<sub>4</sub> nanoparticles. *Physical Review Letters* 77(2):394.
55. Batlle X, Labarta A 2002. Finite-size effects in fine particles: magnetic and transport properties. *Journal of Physics D: Applied Physics* 35(6):R15.
56. Durmus Z, Kavas H, Baykal A, Sozeri H, Alpsoy L, Çelik S, Toprak M 2011. Synthesis and characterization of l-carnosine coated iron oxide nanoparticles. *Journal of Alloys and Compounds* 509(5):2555-2561.
57. Sharma, P.; Das, M. R. 2012, Removal of a cationic dye from aqueous solution using graphene oxide nanosheets: Investigation of adsorption parameters. *J. Chem. Eng. Data*, 58, 151–158.
58. Murugan E, Jebaranjitham JN 2012. Synthesis and characterization of silver nanoparticles supported on surface-modified poly (N-vinylimidazole) as catalysts for the reduction of 4-nitrophenol. *Journal of Molecular Catalysis A: Chemical* 365:128-135.
59. Yang Y, Zhang Y, Shu G, Dong Q, Zou L, Zhu Y 2015. Electrochemiluminescence properties of Tb (III) nicotinic acid complex and its analytical application. *Journal of Luminescence* 159:73-78.
60. Amir M, Kurtan U, Baykal A, Sözeri H 2016. MnFe<sub>2</sub>O<sub>4</sub>@ PANI@ Ag heterogeneous nanocatalyst for degradation of industrial aqueous organic pollutants. *Journal of Materials Science & Technology* 32(2):134-141.
61. Kurtan U, Amir M, Yıldız A, Baykal A 2016. Synthesis of magnetically recyclable MnFe<sub>2</sub>O<sub>4</sub>@SiO<sub>2</sub>@Ag nanocatalyst: Its high catalytic performances for azo dyes and nitro compounds reduction. *Applied Surface Science* 376:16-25.
62. Zhao D-L, Zeng X-W, Xia Q-S, Tang J-T 2009. Preparation and coercivity and saturation magnetization dependence of inductive heating property of Fe<sub>3</sub>O<sub>4</sub> nanoparticles in an alternating current magnetic field for localized hyperthermia. *Journal of Alloys and Compounds* 469(1):215-218.
63. Zhang X, Jiang W, Gong X, Zhang Z 2010. Sonochemical synthesis and characterization of magnetic separable Fe<sub>3</sub>O<sub>4</sub>/Ag composites and its catalytic properties. *Journal of Alloys and Compounds* 508(2):400-405.
64. Jana NR, Pal T 1999. Redox catalytic property of still-growing and final palladium particles: a comparative study. *Langmuir* 15(10):3458-3463.
65. Dong Z, Le X, Li X, Zhang W, Dong C, Ma J 2014. Silver nanoparticles immobilized on fibrous nano-silica as highly efficient and recyclable heterogeneous catalyst for reduction of 4-nitrophenol and 2-nitroaniline. *Applied Catalysis B: Environmental* 158:129-135.
66. Vadakkekara R, Chakraborty M, Parikh PA 2012. Reduction of aromatic nitro compounds on colloidal hollow silver nanospheres. *Colloids and Surfaces A: Physicochemical and Engineering Aspects* 399:11-17.

67. Butun S, Sahiner N 2011. A versatile hydrogel template for metal nano particle preparation and their use in catalysis. *Polymer* 52(21):4834-4840.
68. Abdulrahman O 2012. Submicrometre-scale polyaniline colloidal spheres: photopolymerization preparation using fluorescent carbon nitride dots as a photocatalyst. *Catalysis Science & Technology* 2(4):711-714.
69. Ghosh BK, Hazra S, Naik B, Ghosh NN 2015. Preparation of Cu nanoparticle loaded SBA-15 and their excellent catalytic activity in reduction of variety of dyes. *Powder Technology* 269:371-378.
70. Gupta N, Singh HP, Sharma RK 2011. Metal nanoparticles with high catalytic activity in degradation of methyl orange: an electron relay effect. *Journal of Molecular Catalysis A: Chemical* 335(1):248-252.
71. Vidhu V, Philip D 2014. Catalytic degradation of organic dyes using biosynthesized silver nanoparticles. *Micron* 56:54-62.
72. Mallick K, Witcomb M, Scurrall M 2006. Silver nanoparticle catalysed redox reaction: an electron relay effect. *Materials Chemistry and Physics* 97(2):283-287.
73. Le X, Dong Z, Zhang W, Li X, Ma J 2014. Fibrous nano-silica containing immobilized Ni@Au core-shell nanoparticles: A highly active and reusable catalyst for the reduction of 4-nitrophenol and 2-nitroaniline. *Journal of Molecular Catalysis A: Chemical* 395:58-65.
74. Qin, J.; Li, R.; Lu, C.; Jiang, Y.; Tang, H.; Yang, X. 2014, Ag/ZnO/graphene oxide heterostructure for the removal of rhodamine B by the synergistic adsorption-degradation effects. *Ceram. Int.* 41,4231-4237
75. Demirelli M, Karaoğlu E, Baykal A, Sözeri H, Uysal E 2014. Synthesis, characterization and catalytic activity of CoFe<sub>2</sub>O<sub>4</sub>-APTES-Pd magnetic recyclable catalyst. *Journal of Alloys and Compounds* 582:201-207.
76. Karaoglu E, Summak M, Baykal A, Sözeri H, Toprak MS 2013. Synthesis and Characterization of Catalytically Activity Fe<sub>3</sub>O<sub>4</sub>-3-Aminopropyl-triethoxysilane/Pd Nanocomposite. *Journal of Inorganic and Organometallic Polymers and Materials* 23(2):409-417.
77. Rauf MA, Meetani MA, Khaleel A, Ahmed A 2010. Photocatalytic degradation of methylene blue using a mixed catalyst and product analysis by LC/MS. *Chemical Engineering Journal* 157(2):373-378.
78. Shahwan T, Sirriah SA, Nairat M, Boyacı E, Eroğlu AE, Scott TB, Hallam KR 2011. Green synthesis of iron nanoparticles and their application as a Fenton-like catalyst for the degradation of aqueous cationic and anionic dyes. *Chemical Engineering Journal* 172(1):258-266.
79. Khan MM, Lee J, Cho MH 2014. Au@TiO<sub>2</sub> nanocomposites for the catalytic degradation of methyl orange and methylene blue: an electron relay effect. *Journal of Industrial and Engineering Chemistry* 20(4):1584-1590.
80. Naik B, Prasad VS, Ghosh NN 2012. Preparation of Ag nanoparticle loaded mesoporous  $\gamma$ -alumina catalyst and its catalytic activity for reduction of 4-nitrophenol. *Powder technology* 232:1-6.
81. Lu Y, Mei Y, Ballauff M, Drechsler M 2006. Thermosensitive core-shell particles as carrier systems for metallic nanoparticles. *The Journal of Physical Chemistry B* 110(9):3930-3937.
82. Amir M, Kurtan U, Baykal A 2015. Rapid color degradation of organic dyes by Fe<sub>3</sub>O<sub>4</sub>@His@Ag recyclable magnetic nanocatalyst. *Journal of Industrial and Engineering Chemistry* 27:347-353.



83. Patra AK, Dutta A, Bhaumik A 2010. Cu nanorods and nanospheres and their excellent catalytic activity in chemoselective reduction of nitrobenzenes. *Catalysis Communications* 11(7):651-655.
84. Chi Y, Yuan Q, Li Y, Tu J, Zhao L, Li N, Li X 2012. Synthesis of Fe<sub>3</sub>O<sub>4</sub>@SiO<sub>2</sub>-Ag magnetic nanocomposite based on small-sized and highly dispersed silver nanoparticles for catalytic reduction of 4-nitrophenol. *Journal of colloid and interface science* 383(1):96-102.
85. Ai L, Yue H, Jiang J 2012. Environmentally friendly light-driven synthesis of Ag nanoparticles in situ grown on magnetically separable biohydrogels as highly active and recyclable catalysts for 4-nitrophenol reduction. *Journal of Materials Chemistry* 22(44):23447-23453.
86. Li, Y.; Du, Q.; Liu, T.; Sun, J.; Wang, Y.; Wu, S.; Wang, Z.; Xia, Y.; Xia, L. 2013 Methylene blue adsorption on graphene oxide/calcium alginate composites. *Carbohydr. Polym.* 95, 501–507.
- Liu P, Zhao M 2009. Silver nanoparticle supported on halloysite nanotubes catalyzed reduction of 4-nitrophenol (4-NP). *Applied Surface Science* 255(7):3989-3993.
87. Tang S, Vongehr S, Meng X 2009. Carbon spheres with controllable silver nanoparticle doping. *The Journal of Physical Chemistry C* 114(2):977-982.

## CURRICULUM VITAE

Personal Information	
Name Surname	Ümran KURTAN
Place of Birth	Fatih/İstanbul
Date of Birth	23.09 1987
Nationality	<input checked="" type="checkbox"/> T.C. <input type="checkbox"/> Other:
Phone Number	505-674-47-35
Email	umrankurtan@gmail.com
Web Page	

Educational Information	
B. Sc.	
University	Fatih University
Faculty	Science and Art Faculty
Department	Department of Chemistry
Graduation Year	15.06.2011

M. Sc.	
University	Fatih University
Institute	Institute of Science
Department	Department of Chemistry
Programme	Chemistry Programme

Ph. D.	
University	Istanbul University-Cerrahpasa
Institute	Institute of Graduate Studies
Department	Department of Bio and Nanotechnology Engineering
Programme	Bio and Nanotechnology Engineering Programme

Publications
<p><b>U. Kurtan</b>, A. Baykal, H.Sözeri, "Recyclable <math>Fe_3O_4@Twee20@Ag</math> Nanocatalyst for Catalytic Degradation of Azo Dyes", Journal of Inorganic and Organometalic Polymers, 25 (2015) 921-929</p> <p><b>U. Kurtan</b>, A.Baykal, "<math>Fe_3O_4@Twee20@Ag</math> Magnetically Recyclable Nanocatalyst for Various Hydrogenation Reactions", Journal of Inorganic and Organometalic</p>

Polymers, 25 (2015) 657-663

M Amir, **U Kurtan**, A Baykal, H Sözeri, “*MnFe<sub>2</sub>O<sub>4</sub>@PANI@Ag Heterogeneous Nanocatalyst for Degradation of Industrial Aqueous Organic Pollutants*”, Journal of Materials Science & Technology, 32, (2016) 134-141.

**U. Kurtan**, M. Amir, A. Yıldız, A. Baykal, “*Synthesis of magnetically recyclable MnFe<sub>2</sub>O<sub>4</sub>@SiO<sub>2</sub>@ Ag nanocatalyst: Its high catalytic performances for azo dyes and nitro compounds reduction*”, Applied Surface Science, 376 (2016) 16-25.

**U.Kurtan**, A.Baykal, “*Fabrication and characterization of Fe<sub>3</sub>O<sub>4</sub>@APTES@PAMAM-Ag highly active and recyclable magnetic nanocatalyst: Catalytic reduction of 4- nitrophenol*”, Materials Research Bulletin, 60 (2014) 79-87.

**U.Kurtan**, M.Amir, A.Baykal, “*A Fe<sub>3</sub>O<sub>4</sub>@Nico@Ag nanocatalyst for the hydrogenation of nitroaromatics*”, Chinese Journal of Catalysis 36 (2015) 705-711.

**U.Kurtan**, M.Amir, A.Baykal, “*Fe<sub>3</sub>O<sub>4</sub>@Nico-Ag magnetically recyclable nanocatalyst for azo dyes reduction*”, Applied Surface Science 363 (2016) 66-73.

M. Amir, **U. Kurtan**, A. Baykal, “*Synthesis and application of magnetically recyclable nanocatalyst Fe<sub>3</sub>O<sub>4</sub>@ Nico@Cu in the reduction of azo dyes*”, Chinese Journal of Catalysis 36 (2015) 1280-1286. M. Amir,

**U. Kurtan**, A. Baykal, “*Rapid color degradation of organic dyes by Fe<sub>3</sub>O<sub>4</sub>@His@Ag recyclable magnetic nanocatalyst*”, Journal of Industrial and Engineering Chemistry 27 (2015) 347-353.

**U. Kurtan**, Md. Amir, A. Baykal, H. Sözeri, M.S. Toprak, “*Magnetically Recyclable Fe<sub>3</sub>O<sub>4</sub>@His@Cu Nanocatalyst for Degradation of Azo Dyes*”, Journal of Nanoscience and Nanotechnology, 16, (2016) 2548-2556.

### Conference Presentations

- Ümran Kurtan, Abdülhadi Baykal, Mehmet Şenel, Esra Alverođlu, Hüseyin Sözeri, “Polyacrylamide-CoFe<sub>2</sub>O<sub>4</sub> Magnetic Hydrogel”, I. International Chemistry and Chemical Engineering Conference, Bakü, Azerbeycan, (2013).
- Ümran Kurtan, Abdülhadi Baykal, “Synthesis of Fe<sub>3</sub>O<sub>4</sub>@APTES@PAMAM-Ag magnetic nanocatalyst as highly active and recyclable for catalytic reduction of 4-nitrophenol”, 10th Nanoscience and Nanotechnology Conference, Yeditepe Üniversitesi İstanbul-Türkiye, (2014).